Helsinki University of Technology
Faculty of Electronics, Communications and Automation
Department of Electrical Engineering

Modeling and control of flexural rotor vibration of a two-pole cage induction motor

Anssi Sinervo

Master's thesis submitted in partial fulfilment of the requirements for the degree of Master of Science in Technology

Espoo, 24th November 2008

Supervisor: Prof. Antero Arkkio
Instructor: Kai Zenger, D.Sc.(Tech.)

HELSINKI UNIVERSITY OF TECHNOLOGY Faculty of Electronics, Communications and Automation	ABSTRACT OF MASTER'S THESIS

Author	Anssi Sinervo	Date	24th November 2008
		Pages	11 + 95
Title of thesis	Modeling and control of flexural rotor vibration of a two-pole cage induction motor		
Professorship	Electromechanics	Code	S-17
Supervisor	Prof. Antero Arkkio		
Instructor	Kai Zenger, D.Sc.(Tech.)		

The modeling and control of flexural rotor vibrations of large cage induction motors were tested with a 30 kW test machine. The 2-pole test machine was customized to behave like bigger machines. The vibrations were controlled with a 4-pole extra stator winding. A physical, time-periodic model was derived for the machine and written to state-space form for the controllers. The deformation of rotor axis and the disturbance forces were also modeled.

The models for the test machine were identified with various methods. Time periodic identification was attempted with indecisive results. Controllers were designed for the identified models and they were tested with described test measurement set-up. The controllers were tested at various operation points including the critical speed.

Despite modeling difficulties caused by the curvature shape of the rotor, the rotor vibrations were controlled successfully. The extra winding could be used to create controlled force that is sufficient for controlling the vibrations. The vibrations were damped at all rotation speeds as long as the main flux of the machine was sufficient. With the vibration control, the machine could also be continuously driven at the critical speed.

Keywords

Active control, Flexural vibrations, Convergent Control, Critical speed, Linear Quadratic controller, Time-periodic modeling

TEKNILLINEN KORKEAKOULU Elektroniikan, tietoliikenteen ja automaation tiedekunta	DIPLOMITYÖN TIIVISTELMÄ

Tekijä	Anssi Sinervo	Päiväys	24. marraskuuta 2008
		Sivumäärä	11 + 95
Työn nimi	Kaksinapaisen oikosulkumoottorin poikittaisvärähtelyjen mallinnus ja säätö		
Professuuri	Sähkömekaniikka	Koodi	S-17
Työn valvoja	Prof. Antero Arkkio		
Työn ohjaaja	TkT Kai Zenger		

Suurten oikosulkumoottoreiden taivutusvärähtelyn mallinnusta ja säätöä tutkittiin 30 kW koelaitteen avulla. Kaksinapaista testimoottoria oli muokattu ominaisuuksiltaan muistuttamaan suurempia koneita. Värähtelyjä säädettiin staattoriin asennetulla nelinapaisella lisäkäämillä. Koneelle johdettiin fysikaalinen aikaperiodinen malli, joka kirjoitettiin tilaesitykseksi säätimiä varten. Mallinnuksessa otettiin huomioon roottorin vääntynyt akseli ja muut häiriövoimat.

Koneen mallit identifioitiin useilla eri tavoilla. Myös aikaperiodista mallinnusta yritettiin. Säätimet suunniteltiin identifioitujen mallien perusteella ja niiden suorituskykyä tutkittiin työssä kuvaillulla mittalaitteistolla. Säätimiä kokeiltiin useissa koneen toimintapisteissä, myös kriittisellä nopeudella.

Roottorin käyryyden aiheuttamista mallinnusvaikeuksista huolimatta roottorivärähtelyt saatiin vaimennettua. Lisäkäämillä pystyttiin luomaan hallittua voimaa, joka riitti värähtelyjen vaimentamiseen. Värähtelyt pystyttiin vaimentamaan kaikilla pyörimistaajuuksilla kunhan koneen päävuo oli riittävä. Värähtelysäädön ansiosta konetta voitiin ajaa jatkuvasti myös kriittisellä pyörimisnopeudella.

Avainsanat

Aikaperiodinen mallinnus, Aktiivivaimennus, Kriittinen nopeus, LQ-säätö, Poikittaisvärähtely

Preface

This thesis is a part of 3-year research project "ACRVEM" (Active Control of Rotor Vibrations in Electrical Machines) funded by the Academy of Finland. I joined the project in the middle of the second year. I'm grateful to my instructor Kai Zenger for hiring me to the Laboratory of Control Engineering at TKK for the project in the first place. I'm also thankful that he had faith in my abilities even though, for the most times, he had no clue what I was doing. Sometimes even I didn't know what I was doing.

I wrote my thesis, and did most of the research work reported in it, in the Laboratory of Electromechanics, TKK. I want to thank my supervisor Antero Arkkio for letting me transfer to his lab (after control lab run out of money) and letting me work on my thesis almost 6 months longer than planed. I feel like I learned a lot from his comments about the thesis.

This thesis was delayed because of technical difficulties with the test machine. I would like to thank my colleagues Antti Laiho from VTT and Juha Orivuori from control engineering for the countless and countless hours spent in the machine hall trying to understand the test machine. Laiho introduced me to the equations and modeling of the machine, and it was the LQ controller optimized by Orivuori that really saved our project.

I must thank my friends for their support throughout my studies and especially for the language and LaTeX-support when writing my thesis. And last but not least, I should thank my family for listening me explain about my work and studies even when my explanations made no sense to them.

Espoo, 24th November 2008

Anssi Sinervo

Contents

Nomenclature

Abbreviations

CC	Convergent Control
DC	Direct Current (constant component)
FRF	Frequency Response Function
LTI	Linear Time Invariant
LTP	Linear Time Periodic
LQ	Linear Quadratic (controller)

Symbols

$\underline{x}$	complex variable x
$\underline{x}^*$	complex conjugate of x
x^T	transpose of matrix or vector x
$\underline{\hat{x}}$	space vector of variable x
$\hat{x}$	magnitude of space vector of variable x
$\dot{x}$, $\ddot{x}$	first and second derivative of x with respect to time

x^{k}, x^{r}, x^{s}	x in k-, rotor and stator coordinates (frame of reference)
x_{h}, x_{r}, x_{s}	air gap, rotor, stator related variable
$x_{\mathrm{s},0}$	LTI component of stator related variable x
$x_{\mathrm{s},2}$	LTP component of stator related variable x
$\mathfrak{F}\{x\}$	discrete Fourier transformation of x
α	parameter of CC, [-]
γ	parameter of CC, [-]
δ_0	effective air gap length when rotor is centered, [m]
$\mathbf{\Xi}$	damping matrix of the mechanical model, [-]
$\underline{\eta}$	modal coordinate vector of rotor displacement, [-]
μ	permeability, [H/m]
σ	Maxwell stress tensor, [Pa]
ϕ	magnetic flux, [Wb]
φ	polar coordinate [rad]
φ_{s}	phase angle of supply at $t = 0$, [rad]
$\mathbf{\Phi}$, $\mathbf{\Phi}^T$	modal matrix of the mechanical model, [m],[1/N]
ψ	flux linkage, [Wb]
ω	angular frequency, [rad/s]

ω_k	mechanical angular frequency of coordination system k, [rad/s]
ω_s	supply frequency, [rad/s]
$\mathbf{\Omega}$	Eigenfrequency matrix of the mechanical model, [rad/s]
Ω_M	rotational speed of rotor, [rad/s]
A	effective area of winding or coil, [m^2]
$\mathbf{A}$, $\tilde{\mathbf{A}}$, $\mathbf{A}_\mathrm{d}$	system matrix for model, observer, disturbance
$\mathbf{B}$, $\mathbf{B}_\mathrm{d}$	system matrix for model, observer, disturbance
$\mathbf{B}(\mathbf{x}, t)$	magnetic flux density, [T]
$\underline{\hat{B}}_0$, $\underline{\hat{B}}_1$, $\underline{\hat{B}}_2$	space vectors of unipolar, 2-pole and 4-pole flux density, [T]
$\mathbf{C}$, $\tilde{\mathbf{C}}$, $\mathbf{C}_\mathrm{d}$	system matrix for model, observer, disturbance
C_F	force coefficient, [m^2/H]
d_r	diameter of rotor core, [m]
$\underline{D}$	disturbance
F	total force on rotor, [N]
$\underline{F}_\mathrm{c}$	control force, [N]
$\underline{F}_\mathrm{e}$	magnetic force, [N]
$\underline{f}_\mathrm{ex}$	external forces on rotor, [N]
g	complex system gain for one frequency

g_δ	model error multiplier
G	transfer function of the system
G_δ	transfer function of model error
$\mathbf{H}$	magnetic field strength, [A/m]
i	current, [A]
j	imaginary unit, [-]
J_c	quadratic cost function for control, [-]
J_o	quadratic cost function for state observer, [-]
$\mathbf{K}$	Kalman gain for state observer
$K_{\mathrm{r},2}$, $K_{\mathrm{c},2}$	flux coefficients for 4-pole rotor and extra winding currents , [T/A]
l	length, [m]
l_r	length of the rotor core, [m]
L	self inductance, [H]
$\mathbf{L}$	state feedback matrix
L_m	magnetizing or mutual inductance, [H]
L_σ	leakage inductance, [H]
m, n	some indexes, non-negative integers, [-]
N	number of turns in a coil, [-]
p	number of pole pairs, [-]

P_{mech}	mechanical power, [W]
$\mathbf{Q}$	weight matrix for states in LQ designing, [-]
R	resistance, [Ω]
$\mathbf{R}$	weight matrix for control signal LQ designing, [-]
S	slip of the rotor with respect to the 2-pole field, [-]
t	time, [s]
T	length of time step, [s]
T_{e}	electromagnetic torque, [Nm]
u	voltage, [V]
$\underline{U}$	vector of complex control voltage in CC, [V]
$\underline{\mathbf{x}}$	state vector for model
$\underline{\hat{\mathbf{x}}}$, $\underline{\hat{\mathbf{x}}}_{\mathrm{d}}$	estimated state vectors of dynamic and disturbance model, respectively
$\underline{\tilde{\mathbf{x}}}$	state error
X	combined constant of physical parameters, [m]
$\underline{\mathbf{y}}$, $\underline{\tilde{\mathbf{y}}}$	model output and model output error, [-]
z, $\underline{Z}$	vector of measured system outputs, [m]
$\underline{z}_{\mathrm{e}}$	magnetic displacement of the rotor core, [m]
$\underline{z}_{\mathrm{s}}$	shape displacement of the rotor core, [m]

Chapter 1

Introduction

This thesis is related to research that aims to solve problems with lateral rotor vibration of large induction machines. Rotors of electrical machines are never perfectly balanced. When the rotor rotates, the mass unbalance causes mechanical forces that cause vibration. The forces cause the rotor to move from the center of the stator. The displacement of the rotor makes the air gap between the rotor and stator non-symmetric which will also exert magnetic forces on the rotor. These can amplify or dampen the vibration.

This thesis focuses on radial forces that cause flexural vibration. Machines can also have torsional and axial vibration but the force from the mass unbalance is mostly radial. There is a special interest in flexural vibrations of large over 5 MW induction machines, used for example for large industrial pumps. Such machines tend to have long rotors that have a low natural resonance frequency, usually within the operating range of the machine.

Natural resonance frequencies are something that all structures have. Any force excitation at such a frequency can cumulate and be amplified significantly more than at other frequencies. Structures technically have infinite number of these frequencies. The high natural frequencies can cause noise problems when machines are supplied from frequency converters. The lower frequencies cause mechanical problems.

When studying only the flexural vibrations of large induction machine rotors, the lowest bending mode dominates. This mode can be excited by the radial forces from rotation. Thus, most machines cannot be run continuously at this frequency or at a certain frequency band around it. The vibration could break the rotor bearings or even cause the rotor to hit the stator breaking the entire machine, thus it is called *critical speed*. The flexural vibrations wear off the rotor bearing even when the rotor is not at the critical speed. There are also standards that define maximum vibration levels for machines.

Controlling the flexural vibrations would protect the bearings increasing the life span or the maintenance interval of machines. Being able to keep the rotor centered would also reduce some power loses caused by rotor eccentricity further improving the overall efficiency of the machines. Still, the biggest benefit would be the ability to drive the machine freely at all frequencies.

The vibrations are to be controlled with a secondary stator winding. For 2-pole machines, a 4-pole extra winding can be used to exert radial forces to the rotor. It might even be possible to levitate the rotor with the extra winding so that the rotor requires no bearings at all. The first objective of the research is still to reduce the vibration of the rotor to protect bearings and to be able to drive the machines at all rotation speeds.

Chiba, Fukao & Rahman (2006) and the rest of their team have done extensive work in this field. This thesis, however, is related to another research project with slightly different approach. In this work, the 4-pole control winding is supplied from voltage source whereas Hiromi, Katou, Chiba, Rahman & Fukao (2007) use current driven controllers.

The models and controllers are tested with a small-scale test-machine. The test machine has been modified to resemble more closely bigger machines. This thesis does not include any of the simulation results done related to this work. Several publication have already been released about the simulations and about the methods to be used (Laiho, Tammi, Zenger & Arkkio 2008), (Zenger, Sinervo, Orivuori, Laiho & Tammi 2008), (Orivuori, Laiho & Sinervo 2008). One master's thesis has also been done about the simulations (Orivuori 2008).

1.1 Objective of the thesis

Objective of the thesis is to show that the extra stator winding can be used to control the flexural vibrations and to find a control algorithm for this purpose.

1.2 Overview of the thesis

Chapter 2 explains only the basics about electrical machines needed to understand what has been done. The chapter does include some unconventional notations that might be new to some readers who are familiar with electrical machines. Mostly the chapter is useful for readers with control engineering background.

Chapter 3 explains the physics behind the radial forces and derives the

equations used. Some of the derivations rely on work done by Holopainen (2004). Not all the physical phenomena have been included into the equations, such as slot harmonics and saturation harmonics. They have been discussed in (Arkkio & Holopainen 2008). Transient phenomena (Kovács 1984) were also neglected. Some features like shape of the rotor axis was included to the model because it was detected to be important during the measurements.

The different control algorithms used are presented in Chapter 4. The research was mostly oriented towards developing more sophisticated controllers for the machine, but because of problems with the test machine, the focus shifted more towards modeling. Unfortunately, not all the controllers could be tested and thus they are not included in this thesis.

Chapter 5 describes the measurement set-up and measurement techniques used. It also explains how the data was pre and post processed. Some of the techniques might be easier to understand if the Results chapter (6) is visited first.

Chapter 6 is the longest and it shows all the results from the measurements. The chapter is divided into three sections. Measurements of the disturbance forces that cause the vibration of the rotor, have been presented in the first section. The disturbance forces were bigger than expected and caused some practical problems. The forces affected the course of the research forcing new issues to be taken into account.

Chapter 2

Electrical machines

2.1 Basic principles

The voltage induced into a conducting coil in a changing magnetic field is given by

$$u = Ri + \frac{\mathrm{d}\psi}{\mathrm{d}t} \tag{2.1}$$

where R is the resistance of the coil, i the current of the coil and ψ the flux linkage of the coil. The flux linkage is the sum of the magnetic fluxes penetrating the individual loops of the coil. This law, known as Faraday law of induction, couples the magnetic flux and voltage.[1](Chiasson 2005)

In electrical machines, the magnetic flux is generated by permanent magnets or currents in conducting coils. According to the Ampère's circuital law, a current in a conductor generates a circular magnetic field around it. The weak form of the law says that the integral of magnetic field strength along a closed loop gives the total current flowing through the loop.

$$\oint_S \mathbf{H} \cdot \mathbf{dl} = i_S \tag{2.2}$$

If this law is applied to a coil, it can be simplified. If the integration path is chosen so that the magnetic field strength is constant on the path and the path goes through the coil, the law becomes

$$lH_\mathrm{l} = Ni \tag{2.3}$$

where l is the length of the path, H_l the magnetic field strength of the path, N the number of turns in the coil and i the current of the coil. The term Ni is called *magneto motive force*.

If we consider a situation, where there is more than one coil, part of the magnetic field can pass through several coils. For the part of the field that is common for a group of coils, the field strength depends on the magneto motive forces of the coils in the group.

The magnetic flux of a coil can be obtained from the magnetic field strength via integration. Multiplying the magnetic field strength with permeability μ of the material, where the field is, gives the magnetic flux density. The magnetic flux, ϕ, of an individual loop of the coil is obtained by integrating the flux density, $\mathbf{B}$, over the area of the loop. If the flux density is assumed to be constant, the flux linkage of the coil is a product of flux density, average area of a coil loop, and the number of turns in the coil.

$$\phi = \int_A \mathbf{B} \cdot \mathbf{dA} = \int_A \mu \mathbf{H} \cdot \mathbf{dA} \tag{2.4}$$

[1]The Faraday law of induction is usually presented without the current term Ri.

Flux linkages are often presented as a product of current and inductance, L. Inductance comprise the physical dimensions of the coil and its surroundings. Currents in other coils that share part of the magnetic field with the one considered, contribute to the total flux linkage. Thus the flux linkage of a coil is

$$\psi_\mathrm{s} = L_\mathrm{s} i_\mathrm{s} + \sum_k (L_{\mathrm{s},k} i_k) \tag{2.5}$$

where L_s is the self inductance of the coil, $L_\mathrm{s,k}$ are the mutual inductances between the coil and other coils, and i_k are the currents in the other coils.

In most control applications, the inductances are assumed to be constant. However, the inductance depends on the permeability of the material that the magnetic flux flows through. In electrical machines, the materials include iron and the permeability of iron is a non-linear function of magnetic flux density or field strength. Thus the permeability and the inductances depend on the currents that generate the magnetic field. This nonlinear dependence is ignored and the inductances are defined as constants in some operation point. (Hubert 2002)

2.2 Mathematical notations and definitions used in electric machines

In this work, electric machines are modeled only in two dimensions, which makes it convenient to use complex coordinates. Forces and displacements are represented as complex vectors, where the real part of the vector is the cartesian x-direction component and the imaginary part the y-direction, respectively. It is customary in electrical engineering to present currents and voltages as complex quantities; thus, representing the mechanical variables in the same way makes them easier to combine.

Most large electric machines have 3 phases in their windings. The phase currents and voltages can usually be assumed symmetric allowing them to be represented as *space vectors*. Symmetric means that the sum of the three phases is zero[2] which removes one degree of freedom. The space vector for voltage is defined from the phase voltages as follows.

$$\underline{\hat{u}} = \frac{2}{3}\left(u_\mathrm{a} + u_\mathrm{b} e^{\mathrm{j}\frac{2\pi}{3}} + u_\mathrm{c} e^{\mathrm{j}\frac{4\pi}{3}}\right) \tag{2.6}$$

[2]The sum of voltages does not have to be zero. The winding of machines are usually connected in such way that the so called zero component does not affect the behavior of the machine.

The space vector notation brings the electromagnetic variables to the same complex coordination system just defined for the mechanical variables. The exponent terms correspond to the physical locations of the three windings. However, if the machine has more pole pairs than one, the angles between winding are not $2\pi/3$, but are divided with the number of pole pairs, p. The winding pattern repeats itself p times and the voltage vector would point to p different directions. The space vector defines the direction for one of these.

Direction of voltage seems like a bizarre concept but it is related to the direction of the magnetic fields and flux. The windings couple the currents and voltages to the fields. The magnetic flux is usually studied only in the air gap and only in radial direction. By using polar coordinates, the flux density vector field in the air gap can be written into a sum where time and space dependencies have been separated.

$$\mathbf{B}(\mathbf{x}, t) = \sum_k \cos(k\varphi) B_k(t) \hat{\mathbf{e}}_\mathbf{r} \tag{2.7}$$

The $\hat{\mathbf{e}}_\mathbf{r}$ is the unit vector in radial direction, φ the angle coordinate, and $\mathbf{x}$ general position vector. The sum (2.7) is the spatial Fourier series for the flux. It has been assumed that the flux density is symmetric around poles and thus the sum has only cosine terms.

It is a common assumption that the voltage space vector only excites one of the terms in the sum (2.7), the one that has $k = p$. The flux density is assumed sinusoidal in space and to have p maximums. The rest of the terms in the sum are called *spatial harmonics*. Usually machines are built so that the harmonics are as small as possible.

One major advantage of representing quantities as complex variables is the transformations to rotating coordinates. For example, some equations are easier to write in coordination that rotates with the rotor of the machine. The transformation from stator coordinates (static) to arbitrary coordinates rotating with angular frequency ω_k can be done by multiplying variable with exponent function.

$$\underline{\hat{u}}^\mathrm{k} = \underline{\hat{u}}^\mathrm{s} e^{-\mathrm{j}p\omega_\mathrm{k} t} \tag{2.8}$$

Superscripts k and s indicate arbitrary and stator coordinates, respectively. It should be noted that the pole pair number p exists in the equation. The pole pair number affects the apparent frequency of the currents and voltages in the coordination transformation. This is because the physical voltage vector turns only the length between one pole pair while the space

vector makes a full circle. The same transformation can be used for the mechanical variables as well. For them p equals one.

Normal machines have only one stator winding and thus only one pole pair number, p. To be able to use the same equations for different machines that have different numbers of poles, the coordination transformation is often defined without p. The frequencies for current and voltage space vectors are thought to be in *electrical degrees*. The pole pair number is taken into account only, when calculating mechanical quantities like torque or rotation speed of the machine. This allows the same electrical equations to be used for machines with different number of poles.

The machines studied in this work have two stator windings with different number of poles. Using electrical degrees would lead into confusion because there are two different p values in the equations. The two windings are coupled by the magnetic field that does have some real direction. Thus all the angles and angular frequencies are in mechanical degrees and the coordination transformations have p included.

2.3 Cage induction machine

The structure of a cage induction machine has been explained with illustrative figures in (Hubert 2002) Chapter 4 and in (Boldea & Nasar 2002). The stator of an induction machine has a three phase winding and the rotor consists of laminated steel sheets (rotor core) and a conductive cage usually made of aluminium. The cage is made of rotor bars and end rings that connect the bars together from both ends, see Figure 2.1. The rotor bars can be parallel to the rotor shaft, like in the figure, or they can be skewed to reduce the asymmetric effect of individual bars and to make the torque smoother. The cage is usually casted into the rotor core.

The rotor bars and end rings form closed circuits in which currents can be induced when the magnetic flux through the loop changes. The 3-phase winding in the stator is used to create a rotating magnetic field. If the rotor does not rotate with the field, the magnetic flux through the rotor cage changes.

According to Lenz's law the rotation induces currents that try to counter the changes in the fluxes that penetrate the loops. For the loop that the field has just passed, the current tries to keep the flux flowing and thus strengthens the flux. For the loop the field is just moving to, the current tries to prevent the flux from entering. This causes the flux to twist, see Figure 2.2.

Magnetic forces try to align the flux in the rotor with the field of the stator thus creating electromagnetic torque. Currents are induced only if the

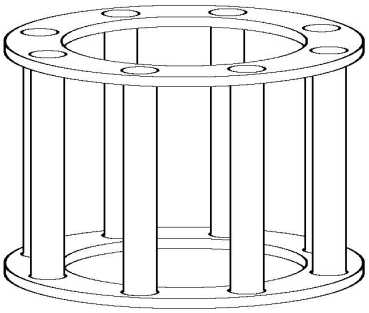

Figure 2.1: The cage of a cage induction machine is often called a squirrel cage because it looks like an exercising wheel of a hamster or squirrel.

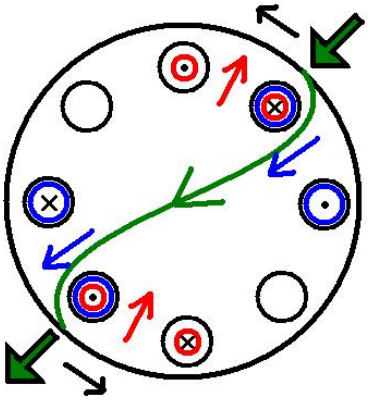

Figure 2.2: Magnetic flux in the squirrel cage rotor core when stator field is rotating with respect to the rotor. A dot denotes current coming out of the page and x current going into the page. The colored circles and small arrows denote loop currents and the flux they induce. The big arrows represent the stator field rotating counter-clockwise.

rotor rotates slower[3] than the field. The rotor is slowed down by any load torques attached to it.

It is difficult to consider all rotor bar currents separately because all the induction loops are connected together. It is possible, however, to represent the effective rotor cage current as a single space vector. Thus the equation (2.1) can be written for the stator winding and for the rotor cage. The rotor voltage is zero because the rotor cage is short circuited.

$$\hat{\underline{u}}_\mathrm{s} = R_\mathrm{s}\hat{\underline{i}}_\mathrm{s} + \frac{\mathrm{d}\hat{\underline{\psi}}_\mathrm{s}}{\mathrm{d}t} \tag{2.9}$$

$$0 = R_\mathrm{r}\hat{\underline{i}}_\mathrm{r} + \frac{\mathrm{d}\hat{\underline{\psi}}_\mathrm{r}}{\mathrm{d}t} \tag{2.10}$$

The flux linkages are assumed to be composed of some mutual flux $\hat{\underline{\psi}}_h$ and leakage fluxes $\hat{\underline{\psi}}_{\sigma,\mathrm{s}}$ and $\hat{\underline{\psi}}_{\sigma,\mathrm{r}}$. The flux linkages are also assumed to be linearly dependent on the currents; thus, they can be written with inductances like in Equation (2.5). Both the stator and rotor currents affect only their own leakage fluxes besides contributing to the mutual flux.

$$\hat{\underline{\psi}}_\mathrm{s} = \hat{\underline{\psi}}_{\sigma,\mathrm{s}} + \hat{\underline{\psi}}_h = L_{\sigma,\mathrm{s}}\hat{\underline{i}}_\mathrm{s} + L_\mathrm{m}(\hat{\underline{i}}_\mathrm{s} + \hat{\underline{i}}_\mathrm{r}) = L_\mathrm{s}\hat{\underline{i}}_\mathrm{s} + L_\mathrm{m}\hat{\underline{i}}_\mathrm{r} \tag{2.11}$$

$$\hat{\underline{\psi}}_\mathrm{r} = \hat{\underline{\psi}}_{\sigma,\mathrm{r}} + \hat{\underline{\psi}}_h = L_{\sigma,\mathrm{r}}\hat{\underline{i}}_\mathrm{r} + L_\mathrm{m}(\hat{\underline{i}}_\mathrm{s} + \hat{\underline{i}}_\mathrm{r}) = L_\mathrm{r}\hat{\underline{i}}_\mathrm{r} + L_\mathrm{m}\hat{\underline{i}}_\mathrm{s} \tag{2.12}$$

The flux linkages are substituted into the voltage equations (2.9) and (2.10). The rotation of the rotor has to be taken into account and therefore the rotor voltage equation (2.10) has to be written in rotor coordinates.

$$\hat{\underline{u}}_\mathrm{s}^\mathrm{s} = R_\mathrm{s}\hat{\underline{i}}_\mathrm{s}^\mathrm{s} + L_\mathrm{s}\frac{\mathrm{d}\hat{\underline{i}}_\mathrm{s}^\mathrm{s}}{\mathrm{d}t} + L_\mathrm{m}\frac{\mathrm{d}\hat{\underline{i}}_\mathrm{r}^\mathrm{s}}{\mathrm{d}t} \tag{2.13}$$

$$0 = R_\mathrm{r}\hat{\underline{i}}_\mathrm{r}^\mathrm{r} + L_\mathrm{m}\frac{\mathrm{d}\hat{\underline{i}}_\mathrm{s}^\mathrm{r}}{\mathrm{d}t} + L_\mathrm{r}\frac{\mathrm{d}\hat{\underline{i}}_\mathrm{r}^\mathrm{r}}{\mathrm{d}t} \tag{2.14}$$

If the machine's stator is supplied with a balanced 3-phase sinusoidal voltage with supply frequency ω_s, the space vector of stator voltage is

$$\hat{\underline{u}}_\mathrm{s}^\mathrm{s} = \hat{u}e^{\mathrm{j}\frac{\omega_s}{p}t} \tag{2.15}$$

Amplitude of the voltage is $\hat{u}$ and p is the number of pole pairs in the machine. If the amplitude and frequency of the supply are constant and machine operates in a steady state, the currents are also sinusoidal. Equations (2.13) and (2.14) become

[3]faster for generators.

$$\hat{\underline{u}}_{\mathrm{s}}^{\mathrm{s}} = R_{\mathrm{s}}\hat{\underline{i}}_{\mathrm{s}}^{\mathrm{s}} + \mathrm{j}\frac{\omega_{\mathrm{s}}}{p}L_{\mathrm{s}}\hat{\underline{i}}_{\mathrm{s}}^{\mathrm{s}} + \mathrm{j}\frac{\omega_{\mathrm{s}}}{p}L_{\mathrm{m}}\hat{\underline{i}}_{\mathrm{r}}^{\mathrm{s}} \tag{2.16}$$

$$0 = R_{\mathrm{r}}\hat{\underline{i}}_{\mathrm{r}}^{\mathrm{s}} + \mathrm{j}\left(\frac{\omega_{\mathrm{s}}}{p} - p\Omega_{\mathrm{M}}\right)L_{\mathrm{m}}\hat{\underline{i}}_{\mathrm{s}}^{\mathrm{s}} + \mathrm{j}\left(\frac{\omega_{\mathrm{s}}}{p} - p\Omega_{\mathrm{M}}\right)L_{\mathrm{r}}\hat{\underline{i}}_{\mathrm{r}}^{\mathrm{s}} \tag{2.17}$$

where Ω_{M} is the mechanical angular frequency of rotation. The rotor voltage equation has been transformed to stator coordinates. From equations (2.16) and (2.16) it can be seen why electrical degrees are usually used for voltage equations, as mentioned in Section 2.2. In electrical degrees, the space vector of stator voltage would have frequency ω_{s} and $p\Omega_{\mathrm{M}}$ would be defined as electrical rotation frequency.

The relative rotation speed difference between the magnetic field and the rotor is called *slip*, S. The slip is actually the same for mechanical and electrical angular speeds, defined as

$$S = \frac{\omega_{\mathrm{s}} - p\Omega_{\mathrm{M}}}{\omega_{\mathrm{s}}} \tag{2.18}$$

where electrical speeds have been used. When p is reduced from right side of (2.18), the equation contains only mechanical speeds.

From now on, it is assumed that the machine has just one pole pair, $p = 1$. There is no need to keep things complicated since the test machine used for this work was originally a 2-pole machine. The supply frequency ω_{s} is then also the mechanical frequency of the magnetic field.

Equations (2.16) and (2.17) can be used to construct an equivalent circuit shown in Figure 2.3. The slip has been substituted to the rotor voltage equation. It is a common practice to add a resistor parallel to the magnetizing inductance L_{m} to account for iron losses. The nonlinear behavior of iron causes some power to be lost in the iron parts of the machine as well and not just in the windings.

The torque produced by the machine is calculated from power. In the equivalent circuit, the "power loss" in rotor resistance corresponds the power going into the rotor. The resistances in rotor cage consume some of the power but the rest is mechanical power. The equation for the mechanical power is

$$P_{\mathrm{mech}} = \frac{3}{2}\frac{1-S}{S}R_{\mathrm{r}}|\hat{\underline{i}}_{\mathrm{r}}|^2 \tag{2.19}$$

The torque is thus

$$T_{\mathrm{e}} = \frac{P_{\mathrm{mech}}}{\Omega_{\mathrm{M}}} = \frac{3}{2}\frac{1-S}{S}\frac{R_{\mathrm{r}}|\hat{\underline{i}}_{\mathrm{r}}(S)|^2}{\Omega_{\mathrm{M}}} = \frac{3}{2}\frac{R_{\mathrm{r}}|\hat{\underline{i}}_{\mathrm{r}}(S)|^2}{S\omega_{\mathrm{s}}} \tag{2.20}$$

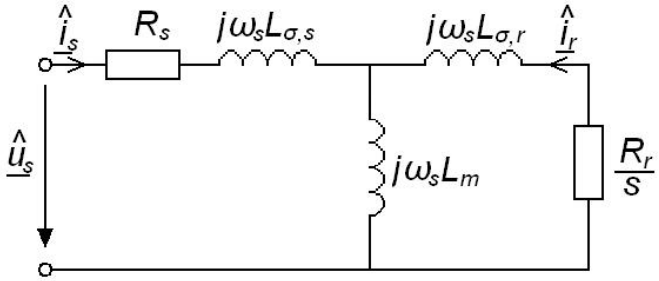

Figure 2.3: Equivalent circuit for induction machine in steady state when supplied from sinusoidal voltage source.

The rotor current can be solved as a function of supply voltage, but the result is very complicated. It can be seen from (2.20) that as the slip gets smaller, the torque increases. However, if the slip is zero, the rotor resistance in the equivalent circuit, in Figure 2.3, goes to infinity and there is no rotor current and thus no torque. This means in practice that the rotor of an induction machine always rotates slower than the magnetic field when the machine is used as a motor, because there is always some load torque from friction.

A real induction machine is never ideal. Thus, it is actually possible that the machine runs without slip when not loaded. The iron core of the rotor can sustain some remanence flux after the machine is started due to hysteresis of iron. This remanence flux behaves like a permanent magnet in the rotor and is pulled towards the rotating magnetic field created by the stator. The remanence flux is weak but can keep the machine rotating with the field as long as the load torque from friction is small. Friction increases with the rotation speed and once the load torque gets bigger than the hysteresis torque, the machine starts to slow down.

When the rotor is rotating with the magnetic field, the field helps to sustain the remanence flux. The field is not parallel to the remanence, or there would be no torque, but stays within 90 degrees. When the rotor slows down, the field starts rotating relative to the rotor. By the time the field is opposite to the remanence flux, it will have demagnetized the rotor core. The hysteresis effect does create a temporary remanence flux with the slowly rotating field as well. The remanence trails the actual field. The torque from this effect is very small, thus the hysteresis torque is rarely an issue with an induction machine.[4]

[4]Hysteresis torque is explained here because it was detected during the measurements.

Chapter 3

Models

3.1 Force production

In Section 2.2, it was mentioned that the spatial harmonics of the magnetic flux density are unwanted in electric machines. However, when studying the radial forces exerted on the rotor, the spatial harmonics of the flux are in fact extremely important. It can be shown that interactions of different flux harmonics cause the radial forces.

The radial force can be calculated from Maxwell stress tensor in polar coordinates

$$\sigma = \begin{bmatrix} \frac{1}{\mu_0} B_\mathrm{r}^2 - \frac{1}{2\mu_0} B^2 & \frac{1}{\mu_0} B_\mathrm{r} B_\tau \\ \frac{1}{\mu_0} B_\mathrm{r} B_\tau & \frac{1}{\mu_0} B_\tau^2 - \frac{1}{2\mu_0} B^2 \end{bmatrix} \tag{3.1}$$

where B_r is the radial part and B_τ the tangential part of the magnetic flux density, B. The force is obtained by integrating the tensor over the rotor surface.

If the flux density in the air gap is assumed to be purely radial, the magnetic force is

$$\underline{F}_\mathrm{e}(t) = \frac{d_\mathrm{r} l_\mathrm{r}}{4\mu_0} \int_0^{2\pi} |\underline{B}(\varphi, t)|^2 e^{\mathrm{j}\varphi} d\varphi \tag{3.2}$$

where d_r is the diameter of the rotor, l_r length of the rotor and $\underline{B}(\varphi, t)$ is the flux density in the air gap. The analogy between 2D-coordination and complex plane has been used to denote directions of the vectors.

The air gap flux can be broken into spatial harmonics. The n:th harmonic would be

$$\underline{B_n}(\varphi, t) = \hat{B}_n(t) \cos\left(n\varphi - \varphi_n(t)\right) e^{\mathrm{j}\varphi} \tag{3.3}$$

where $\hat{B}_n(t)$ is the amplitude and $\varphi_n(t)$ the phase angle of the flux density component. The exponent term $e^{j\varphi}$ tells the direction of the flux vector and it is the only term that is complex. The absolute value of the flux is defined by the other terms. The cosine term can be negative, so direction of the flux is not solely defined by the exponent term.

If the flux density consists of only one harmonic component, like usually assumed, the absolute value of flux is symmetric around the rotor. Thus, the radial force is zero. But, if the air gap flux is composed of two spatial harmonic components n and m, the radial force becomes

$$\begin{aligned}\underline{F}_{\mathrm{e}}(t) &= \frac{d_{\mathrm{r}} l_{\mathrm{r}}}{4\mu_0} \int_0^{2\pi} \Big| \hat{B}_n(t) \cos\left(n\varphi - \varphi_n(t)\right) e^{\mathrm{j}\varphi} \\ &\quad + \hat{B}_m(t) \cos\left(m\varphi - \varphi_m(t)\right) e^{\mathrm{j}\varphi} \Big|^2 e^{\mathrm{j}\varphi} d\varphi \\ &= \frac{d_{\mathrm{r}} l_{\mathrm{r}}}{4\mu_0} \int_0^{2\pi} \Big(\hat{B}_n^2(t) \cos^2(n\varphi - \varphi_n(t)) \\ &\quad + 2\hat{B}_n(t)\hat{B}_m(t) \cos(n\varphi - \varphi_n(t)) \cos(m\varphi - \varphi_m(t)) \\ &\quad + \hat{B}_m^2(t) \cos^2(m\varphi - \varphi_m(t)) \Big) e^{\mathrm{j}\varphi} d\varphi \end{aligned} \tag{3.4}$$

The square terms $\hat{B}_n^2(t)\cos^2(n\varphi - \varphi_n(t))$ and $\hat{B}_m^2(t)\cos^2(m\varphi - \varphi_m(t))$ produce no total force, so they can be left out. This is easy to see if the integration limits are changed to $[-\pi, \pi]$. The cosine is even and $e^{\mathrm{j}\varphi}$ is odd.

$$\begin{aligned}\underline{F}_{\mathrm{e}}(t) &= \frac{d_{\mathrm{r}} l_{\mathrm{r}}}{4\mu_0} \int_0^{2\pi} 2\hat{B}_n(t)\hat{B}_m(t) \cos(n\varphi - \varphi_n(t)) \\ &\quad * \cos(m\varphi - \varphi_m(t)) e^{\mathrm{j}\varphi} d\varphi \end{aligned} \tag{3.5}$$

The cosine functions can be written as complex exponent functions.

$$\begin{aligned}\underline{F}_{\mathrm{e}}(t) &= \frac{d_{\mathrm{r}} l_{\mathrm{r}}}{4\mu_0} \int_0^{2\pi} 2\hat{B}_n(t)\hat{B}_m(t) \frac{e^{\mathrm{j}(n\varphi - \varphi_n(t))} + e^{-\mathrm{j}(n\varphi - \varphi_n(t))}}{2} \\ &\quad * \frac{e^{\mathrm{j}(m\varphi - \varphi_m(t))} + e^{-\mathrm{j}(m\varphi - \varphi_m(t))}}{2} e^{\mathrm{j}\varphi} d\varphi \\ &= \frac{d_{\mathrm{r}} l_{\mathrm{r}}}{8\mu_0} \int_0^{2\pi} \hat{B}_n(t)\hat{B}_m(t) \Big(e^{-\mathrm{j}(\varphi_n(t) + \varphi_m(t))} e^{\mathrm{j}(n+m+1)\varphi} \\ &\quad + e^{-\mathrm{j}(\varphi_n(t) - \varphi_m(t))} e^{\mathrm{j}(n-m+1)\varphi} + e^{-\mathrm{j}(\varphi_m(t) - \varphi_n(t))} e^{\mathrm{j}(m-n+1)\varphi} \\ &\quad + e^{\mathrm{j}(\varphi_n(t) + \varphi_m(t))} e^{\mathrm{j}(1-n-m)\varphi} \Big) d\varphi \end{aligned} \tag{3.6}$$

For the integral to be non zero, one of the arguments of the exponent functions containing φ must be zero. The component numbers n and m are positive or zero and they cannot be equal. Thus, the first of the four terms never produces force. The last term produces force only if $m = 1$ and $n = 0$, or wise versa. The other two terms produce force only if $m - n = \pm 1$. The same result was obtained in (Holopainen 2004).

Defining $m = n + 1$ allows the force equation to be simplified further.

$$\underline{F}_{\mathrm{e}}(t) = \frac{d_{\mathrm{r}} l_{\mathrm{r}}}{8\mu_0} \int_0^{2\pi} \hat{B}_n(t)\hat{B}_m(t)\Big(e^{\mathrm{j}(\varphi_m(t)-\varphi_n(t))} + \delta_{n0} e^{\mathrm{j}(\varphi_n(t)+\varphi_m(t))}\Big) d\varphi \tag{3.7}$$

δ_{n0} is the Kronecker's delta indicating that the second term is included only if $n = 0$. All φ dependencies have disappeared and the integral can be calculated.

If a space vector for the flux density components is defined as

$$\underline{\hat{B}}_n(t) = \hat{B}_n(t) e^{\mathrm{j}\varphi_n(t)} \tag{3.8}$$

the force can be written as

$$\underline{F}_{\mathrm{e}} = \frac{\pi d_{\mathrm{r}} l_{\mathrm{r}}}{4\mu_0} \left(\underline{\hat{B}}_n^* \underline{\hat{B}}_{n+1} + \delta_{n0} \underline{\hat{B}}_0 \underline{\hat{B}}_1\right) \tag{3.9}$$

Having more than two flux components leads to the same conditions for the force. Thus, the total radial force exerted on the rotor, when all flux components are included, is

$$\underline{F}_{\mathrm{e}} = \frac{\pi d_{\mathrm{r}} l_{\mathrm{r}}}{4\mu_0} \left(\underline{\hat{B}}_0 \underline{\hat{B}}_1 + \sum_{n=0}^{\infty} \underline{\hat{B}}_n^* \underline{\hat{B}}_{n+1}\right) \tag{3.10}$$

Not all the components need to be included when calculating the force. Like already mentioned, in normal electrical machines, the $\underline{\hat{B}}_p$ component dominates. Thus, it is justified to assume that the magnetic radial forces come from $\underline{\hat{B}}_p$ component interacting with $\underline{\hat{B}}_{p-1}$ and $\underline{\hat{B}}_{p+1}$ components[1]. In normal machines, in which the rotor rotates in the middle of the stator, these other components are small and there is little force. However, multiple studies have concluded that rotor eccentricity causes $\underline{\hat{B}}_{p-1}$ and $\underline{\hat{B}}_{p+1}$ components to appear in the air gap and these components can cause significant force (Belmans, Vandenput & Geysen 1984) (Taegen 1964).

The spatial harmonic flux components are induced in the air gap due to the air gap length not being constant. This causes *unbalanced magnetic pull* and thus exerts radial force to the rotor. What is interesting is that this force can be detected from the harmonic flux components. The spatial harmonic flux components can also be used to produce controlled radial force on the

[1]Slot harmonics are ignored.

rotor. If the machine's stator is equipped with an extra $p+1$ or $p-1$ pole pair winding, it can be used as a *force actuator*. The test machine used in the project was a 2-pole machine ($p=1$) and it was fitted with 4-pole extra winding.

Machines with 2 poles are a special case, since $p-1=0$ which means that $\underline{\hat{B}}_{p-1}$ is a unipolar flux. It means also that the $n=0$ term in (3.9) comes to play. With the assumptions above the force for the 2-pole machine is

$$\underline{F}_{\mathrm{c}} = \frac{\pi d_{\mathrm{r}} l_{\mathrm{r}}}{4\mu_0}\left(\underline{\hat{B}}_1^*\underline{\hat{B}}_2 + \underline{\hat{B}}_0\underline{\hat{B}}_1 + \underline{\hat{B}}_0^*\underline{\hat{B}}_1\right) \tag{3.11}$$

The indexes 0, 1 and 2 denote the unipolar, 2-pole and 4-pole fields, respectively. Of the three terms, the middle one, will prove to be the most challenging when tempting to build a *linear time invariant* model for the machine.

3.2 Parametric model for the actuator

We are studying a cage induction machine with a 2-pole main winding and a 4-pole control winding. The force exerted on the rotor is caused by the interactions of three flux density components. The main field, the 2-pole flux, is significantly higher than the other two, 4-pole and unipolar. It can be assumed that the machine is supplied from a rigid source and thus the 2-pole flux is unaffected by the other two.

The 4-pole flux has its own winding in the machine through which it can be excited and thus controlled. The unipolar flux is only excited by the rotor's radial displacement. All the flux components induce currents into the rotor cage. The 2-pole flux is defined by the machines supply voltage, but equations for the other two are needed.

When the 2-pole flux is assumed to be known, the other two flux components become functions of currents and rotor displacement. According to Holopainen (2004), the flux densities can be expressed as

$$\underline{\hat{B}}_0^{\mathrm{s}} = \frac{\underline{z}_{\mathrm{e}}^{\mathrm{s}*}}{2\delta_0}\underline{\hat{B}}_1^{\mathrm{s}} \tag{3.12}$$

$$\underline{\hat{B}}_2^{\mathrm{s}} = \frac{\underline{z}_{\mathrm{e}}^{\mathrm{s}}}{2\delta_0}\underline{\hat{B}}_1^{\mathrm{s}} + K_{\mathrm{r},2}\underline{\hat{i}}_{\mathrm{r},p+1}^{\mathrm{s}} + K_{\mathrm{c},2}\underline{\hat{i}}_{\mathrm{c},p+1}^{\mathrm{s}} \tag{3.13}$$

The superscript s denotes stator frame of reference. Equations in (Holopainen 2004) are written in rotor coordinate system but they are the same in stator frame. Parameters $K_{x,2}$ are some constants that are defined more precisely later, $\underline{\hat{i}}_{\mathrm{r},p+1}$ is the 4-pole component of rotor current, $\underline{\hat{i}}_{\mathrm{c},p+1}$ the 4-pole extra

winding current, and $\underline{z}_\mathrm{e}$ is the magnetic displacement of the rotor, to be defined in Section 3.3.

The equations for the rotor and the 4-pole winding currents can be obtained from standard voltage equations of an induction machine, (2.13) and (2.14). Just the eccentricity terms must be added to them. The 4-pole extra winding is considered as just a normal stator winding. Only two voltage equations are required for the model. The 2-pole current is assumed constant and the unipolar flux causes currents only to the end rings of the rotor cage, see Figure 2.1. These currents themselves do not contribute to radial force and the unipolar flux was assumed to be defined by the 2-pole flux and rotor displacement, so the currents are ignored. Therefore voltage equations are only written for the 4-pole fields.

$$\hat{\underline{u}}_\mathrm{c}^\mathrm{s} = R_\mathrm{c}\hat{\underline{i}}_\mathrm{c}^\mathrm{s} + L_\mathrm{c}\frac{\mathrm{d}\hat{\underline{i}}_\mathrm{c}^\mathrm{s}}{\mathrm{d}t} + L_\mathrm{m}\frac{\mathrm{d}\hat{\underline{i}}_\mathrm{r}^\mathrm{s}}{\mathrm{d}t} + \frac{N_\mathrm{c}A_\mathrm{c}}{2\delta_0}\frac{\mathrm{d}\underline{z}_\mathrm{e}^\mathrm{s}\hat{\underline{B}}_1^\mathrm{s}}{\mathrm{d}t} \tag{3.14}$$

$$0 = R_\mathrm{r}\hat{\underline{i}}_\mathrm{r}^\mathrm{r} + L_\mathrm{r}\frac{\mathrm{d}\hat{\underline{i}}_\mathrm{r}^\mathrm{r}}{\mathrm{d}t} + L_\mathrm{m}\frac{\mathrm{d}\hat{\underline{i}}_\mathrm{c}^\mathrm{r}}{\mathrm{d}t} + \frac{N_\mathrm{r}A_\mathrm{r}}{2\delta_0}\frac{\mathrm{d}\underline{z}_\mathrm{e}^\mathrm{r}\hat{\underline{B}}_1^\mathrm{r}}{\mathrm{d}t} \tag{3.15}$$

The parameters A_x, N_x and δ_0 are the effective area and effective number of turns in winding x and the effective air gap length, respectively. They all are assumed to be constant parameters.

The voltages in the rotor are zero since the rotor cage is short circuited. The external voltage in the actuator circuit is the control voltage. The actuator can be driven with either a current or voltage source. For the project, a voltage source was chosen because it is easier. Voltage has no continuity issues to be considered when supplied to the coils, unlike current. Also, using the voltage source allows the 4-pole winding to act as a passive vibration controller when the control signal is zero, see (6.1). A current source does not.

Designing a control for the machine will be easier if the model is made linear. By making assumptions about the main field and expressing the equations in different coordination system, this can be achieved. Since the 2-pole flux was assumed to be defined by only the supply voltage, it can be assumed sinusoidal in time.

$$\hat{\underline{B}}_1^\mathrm{s} = \hat{B}_1 e^{\mathrm{j}(\omega_\mathrm{s}t+\varphi_\mathrm{s})} \tag{3.16}$$

The transient phenomena are not studied here so the amplitude $\hat{B}_1$, supply angular frequency ω_s and phase φ_s are constants and known. The amplitude $\hat{B}_1$ can be left into the model as just one new parameter, but the exponent term does not belong to a time invariant model.

It turns out that the exponent term $e^{\mathrm{j}(\omega_\mathrm{s}t+\varphi_\mathrm{s})}$ vanishes, if the 4-pole currents and the control voltage in the voltage equations (3.14) and (3.15) are expressed in a coordination system that rotates at the electrical angular frequency ω_s, and is locked to the phase of the field. For the 4-pole quantities, this means that the new coordination system rotates with a mechanical angular frequency of half the frequency of the main field, see equation (2.8). The magnetic displacement of the rotor is presented in the stator frame.

Coordination system k is defined so that

$$\hat{\underline{i}}_2^\mathrm{s} = \hat{\underline{i}}_2^\mathrm{k} e^{\mathrm{j}(\omega_\mathrm{s}t+\varphi_\mathrm{s})} \tag{3.17}$$

After substituting (3.17) into the voltage equations (3.14) and (3.15), the exponent terms are eliminated from both the sides.

$$\begin{aligned}\hat{\underline{u}}_\mathrm{c}^\mathrm{k} = {} & R_\mathrm{c}\hat{\underline{i}}_\mathrm{c}^\mathrm{k} + L_\mathrm{c}\frac{\mathrm{d}\hat{\underline{i}}_\mathrm{c}^\mathrm{k}}{\mathrm{d}t} + \mathrm{j}\omega_\mathrm{s}L_\mathrm{c}\hat{\underline{i}}_\mathrm{c}^\mathrm{k} + L_\mathrm{m}\frac{\mathrm{d}\hat{\underline{i}}_\mathrm{r}^\mathrm{k}}{\mathrm{d}t} + \mathrm{j}\omega_\mathrm{s}L_\mathrm{m}\hat{\underline{i}}_\mathrm{r}^\mathrm{k} \\ & + X_\mathrm{c}\hat{B}_1\left(\frac{\mathrm{d}\underline{z}_\mathrm{e}^\mathrm{s}}{\mathrm{d}t} + \mathrm{j}\omega_\mathrm{s}\underline{z}_\mathrm{e}^\mathrm{s}\right)\end{aligned} \tag{3.18}$$

$$\begin{aligned}0 = {} & R_\mathrm{r}\hat{\underline{i}}_\mathrm{r}^\mathrm{k} + L_\mathrm{r}\frac{\mathrm{d}\hat{\underline{i}}_\mathrm{r}^\mathrm{k}}{\mathrm{d}t} + \mathrm{j}\left(\omega_\mathrm{s} - 2\Omega_\mathrm{M}\right)L_\mathrm{r}\hat{\underline{i}}_\mathrm{r}^\mathrm{k} + L_\mathrm{m}\frac{\mathrm{d}\hat{\underline{i}}_\mathrm{c}^\mathrm{k}}{\mathrm{d}t} \\ & + \mathrm{j}\left(\omega_\mathrm{s} - 2\Omega_\mathrm{M}\right)L_\mathrm{m}\hat{\underline{i}}_\mathrm{c}^\mathrm{k} + X_\mathrm{r}\hat{B}_1\left(\frac{\mathrm{d}\underline{z}_\mathrm{e}^\mathrm{s}}{\mathrm{d}t} + \mathrm{j}\left(\omega_\mathrm{s} - 2\Omega_\mathrm{M}\right)\underline{z}_\mathrm{e}^\mathrm{s}\right)\end{aligned} \tag{3.19}$$

Ω_M is the mechanical angular frequency of the rotor. Note that the factor 2 in front of Ω_M comes from the equations being written for the 4-pole field. To avoid confusion, only the mechanical angular frequencies are used in all the equations. The parameters X_c and X_r have been introduced for convenience. They are defined as

$$X_\mathrm{x} = \frac{N_\mathrm{x}A_\mathrm{x}}{2\delta_0} \tag{3.20}$$

By substituting (3.12) and (3.13) into (3.11) the radial electromagnetic force on the rotor becomes

$$\underline{F}_\mathrm{c}^\mathrm{s} = \frac{\pi d_\mathrm{r} l_\mathrm{r}}{4\mu_0}\left(\frac{L_\mathrm{m}}{2\delta_0}\hat{\underline{B}}_1^{\mathrm{s}*}\left(\frac{\hat{\underline{i}}_\mathrm{c}^\mathrm{s}}{X_\mathrm{c}} + \frac{\hat{\underline{i}}_\mathrm{r}^\mathrm{s}}{X_\mathrm{r}}\right) + 2\frac{\underline{z}_\mathrm{e}^\mathrm{s}}{2\delta_0}|\hat{\underline{B}}_1^\mathrm{s}|^2 + \frac{\underline{z}_\mathrm{e}^{\mathrm{s}*}}{2\delta_0}\left(\hat{\underline{B}}_1^\mathrm{s}\right)^2\right) \tag{3.21}$$

By using the k coordinate system for currents and (3.16), the force simplifies to

$$\underline{F}_\mathrm{c}^\mathrm{s} = C_\mathrm{F}\hat{B}_1 L_\mathrm{m}\left(\frac{\hat{\underline{i}}_\mathrm{c}^\mathrm{k}}{X_\mathrm{c}} + \frac{\hat{\underline{i}}_\mathrm{r}^\mathrm{k}}{X_\mathrm{r}}\right) + 2C_\mathrm{F}\hat{B}_1^2\underline{z}_\mathrm{e}^\mathrm{s} + C_\mathrm{F}\hat{B}_1^2\underline{z}_\mathrm{e}^{\mathrm{s}*}e^{\mathrm{j}2(\omega_\mathrm{s}t+\varphi_\mathrm{s})} \tag{3.22}$$

where

$$C_{\mathrm{F}} = \frac{\pi d_{\mathrm{r}} l_{\mathrm{r}}}{8\delta_0 \mu_0} \tag{3.23}$$

The equations (3.18), (3.19) and (3.22) form the parametric model for the actuator. The actuator force depends on the control voltage and the magnetic displacement of the rotor. The model is linear and almost time invariant. Only the last term in the force equation (3.22) depends explicitly on time.

Comparing the force equation (3.21) with the force equation (3.11) allows the $K_{x,2}$ parameters in Equation(3.13) be defined as

$$K_{x,2} = \frac{L_{\mathrm{m}}}{N_{\mathrm{x}} A_{\mathrm{x}}} = \frac{L_{\mathrm{m}}}{2\delta_0 X_{\mathrm{x}}} \tag{3.24}$$

3.3 Rotor dynamics

In the previous Section 3.2, the magnetic displacement of the rotor was used as a input to the actuator model. The magnetic displacement is the displacement of rotor core from the point, where the magnetic force exerted on the rotor is zero . This "point" can also be a very complicated track inside the stator, but we now assume that it is the geometric center point of the stator. What is not assumed, is that the rotor shaft is straight or that the axis between rotor bearings would pass through the center point of the stator.

When a curved or bowed rotor rotates, the rotor core will run on a circular path around the axis between its bearings. This will cause a rotating component to the magnetic displacement. The magnetic displacement will also have a static component, because the center point of the rotation has some offset to the center point of the stator. In addition to these two components, the rotor shaft can also bend when a force is exerted on it. This displacement caused by bending is called mechanical displacement from now on.

To calculate the mechanical displacement from the forces that affect the rotor, a mechanical model for the rotor dynamics is needed. To obtain this, the rotor is modeled as a symmetric disk on a weightless and flexible shaft that connects to the center point of the disk. The rotor's center of mass is assumed not to be in the middle of the rotor core - the disk -, thus there is a mass unbalance - even if the rotor were straight. This is modeled as a point formed mass on the outer circle of the disk. This model is known as the *Jeffcott rotor* (Jeffcott 1919). The curvature shape of the rotor shaft is ignored for now. It is assumed to have no effect on the dynamics.

The mechanical model can be derived using Lagrange dynamics for small oscillations, (Fetter & Walecka 2003). The model can be written for mechanical displacement in modal form as done by Genta (1999).

$$\ddot{\underline{\eta}} + 2\mathbf{\Xi\Omega}\dot{\underline{\eta}} + \mathbf{\Omega}^2\underline{\eta} = \mathbf{\Phi}^T F \tag{3.25}$$

The time derivatives have been marked as dots on variables and F includes all the forces exerted on the rotor. The mechanical displacement is obtained from the modal coordinate vector as

$$\underline{z}_{\mathrm{m}} = \mathbf{\Phi}\underline{\eta} \tag{3.26}$$

When the rotor shaft's shape is taken into account, the magnetic displacement becomes

$$\underline{z}_{\mathrm{e}} = \mathbf{\Phi}\underline{\eta} + \underline{z}_{\mathrm{s}} \tag{3.27}$$

The variable $\underline{z}_{\mathrm{s}}$ is defined as shape displacement. It is the displacement caused by the bowed rotor shaft and the offset of the axis between rotor bearings.

The modal coordinate vector has been presented as complex vector containing only the first bending mode that also defines the critical speed, (Rao 2000). The other mechanical frequencies are assumed to be so high that they can be left out of the model. In the modal coordinate vector, the real component represents a displacement in x-direction and imaginary in y-direction. The mechanical model is presented as xy-symmetric, which might not be the case in reality. The model can be made real by breaking the modal vector into x- and y-component but that would make it more complicated to combine the model with the electromagnetical model. Thus the mechanics is assumed symmetric.

3.4 Combined mechanical and electromagnetic model

To build a complete model of rotor vibration, the actuator model from Section 3.2 needs to be combined with the mechanical model from Section 3.3. All the necessary equations have already been presented but, to make the control design easier, the model should be made linear and time invariant. The shape of the rotor and the explicit time dependence in the actuator force equation (3.22) make achieving this goal challenging, but it can be done.

The combining equation for the two models is obtained by substituting the actuator force (3.22) in to the mechanical equation (3.25).

$$\begin{aligned}\underline{\ddot{\eta}}^{\mathrm{s}} + 2\boldsymbol{\Xi}\boldsymbol{\Omega}\underline{\dot{\eta}}^{\mathrm{s}} + \boldsymbol{\Omega}^2\underline{\eta}^{\mathrm{s}} = \boldsymbol{\Phi}^T\Big(C_{\mathrm{F}}\hat{B}_1 L_{\mathrm{m}}\left(\frac{\hat{\imath}_{\mathrm{c}}^{\mathrm{k}}}{X_{\mathrm{c}}} + \frac{\hat{\imath}_{\mathrm{r}}^{\mathrm{k}}}{X_{\mathrm{r}}}\right) \\ + 2C_{\mathrm{F}}\hat{B}_1^2\underline{z}_{\mathrm{e}}^{\mathrm{s}} + C_{\mathrm{F}}\hat{B}_1^2\underline{z}_{\mathrm{e}}^{\mathrm{s}*}e^{\mathrm{j}2(\omega_{\mathrm{s}}t+\varphi_{\mathrm{s}})} + \underline{f}_{\mathrm{ex}}\Big)\end{aligned} \tag{3.28}$$

The last force term $\underline{f}_{\mathrm{ex}}$ includes mechanical excitations and other disturbance forces. The next step is to express the magnetic displacement with $\underline{\eta}$ by substituting Equation (3.27) into the mechanical equation and actuator equations.

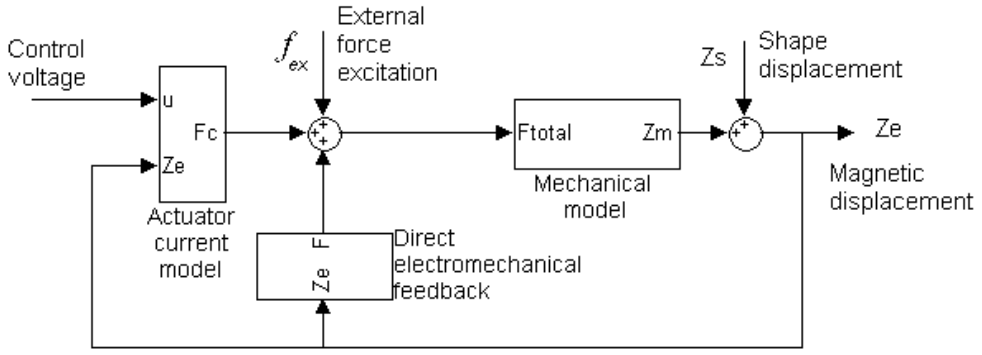

Figure 3.1: The model structure. The actuator current model is defined by equations (3.18) and (3.19). The mechanical model is defined by (3.25) and the direct electromechanical feedback represents the terms of the force equation (3.22) that do not depend on the currents.

When studying the structure of the model, illustrated in Figure 3.1, it can be seen that it is possible to consider the shape displacement being caused by some external force. Thus, the shape displacement can be combined with the other external forces $\underline{f}_{\mathrm{ex}}$ to form one disturbance force. A model for this disturbance force can be build separately and, for some controllers, it is not even required. When the shape displacement is modeled as a part of the disturbance force, it is possible to first build the model without any disturbances. The shape displacement is therefore removed from equations for now. It will be dealt with in Section (3.5).

The equations for the model without disturbance are

$$\underline{\hat{u}}_{\mathrm{c}}^{\mathrm{k}} = R_{\mathrm{c}}\underline{\hat{i}}_{\mathrm{c}}^{\mathrm{k}} + L_{\mathrm{c}}\dot{\underline{\hat{i}}}_{\mathrm{c}}^{\mathrm{k}} + \mathrm{j}\omega_{\mathrm{s}}L_{\mathrm{c}}\underline{\hat{i}}_{\mathrm{c}}^{\mathrm{k}} + L_{\mathrm{m}}\dot{\underline{\hat{i}}}_{\mathrm{r}}^{\mathrm{k}} + \mathrm{j}\omega_{\mathrm{s}}L_{\mathrm{m}}\underline{\hat{i}}_{\mathrm{r}}^{\mathrm{k}} + X_{\mathrm{c}}\hat{B}_1\left(\mathbf{\Phi}\dot{\underline{\eta}} + \mathrm{j}\omega_{\mathrm{s}}\mathbf{\Phi}\underline{\eta}\right) \tag{3.29}$$

$$0 = R_{\mathrm{r}}\underline{\hat{i}}_{\mathrm{r}}^{\mathrm{k}} + L_{\mathrm{r}}\dot{\underline{\hat{i}}}_{\mathrm{r}}^{\mathrm{k}} + \mathrm{j}\left(\omega_{\mathrm{s}} - 2\Omega_{\mathrm{M}}\right)L_{\mathrm{r}}\underline{\hat{i}}_{\mathrm{r}}^{\mathrm{k}} + L_{\mathrm{m}}\dot{\underline{\hat{i}}}_{\mathrm{c}}^{\mathrm{k}} + \mathrm{j}\left(\omega_{\mathrm{s}} - 2\Omega_{\mathrm{M}}\right)L_{\mathrm{m}}\underline{\hat{i}}_{\mathrm{c}}^{\mathrm{k}} + X_{\mathrm{r}}\hat{B}_1\left(\mathbf{\Phi}\dot{\underline{\eta}} + \mathrm{j}\left(\omega_{\mathrm{s}} - 2\Omega_{\mathrm{M}}\right)\mathbf{\Phi}\underline{\eta}\right) \tag{3.30}$$

$$\ddot{\underline{\eta}} + 2\mathbf{\Xi}\mathbf{\Omega}\dot{\underline{\eta}} + \mathbf{\Omega}^2\underline{\eta} = C_{\mathrm{F}}\hat{B}_1\mathbf{\Phi}^T\left(L_{\mathrm{m}}\left(\frac{\underline{\hat{i}}_{\mathrm{c}}^{\mathrm{k}}}{X_{\mathrm{c}}} + \frac{\underline{\hat{i}}_{\mathrm{r}}^{\mathrm{k}}}{X_{\mathrm{r}}}\right) + 2\hat{B}_1\underline{\eta} + \hat{B}_1\underline{\eta}^* e^{\mathrm{j}2(\omega_{\mathrm{s}}t+\varphi_{\mathrm{s}})}\right) \tag{3.31}$$

The time-derivatives are denoted as dots on variables and superscripts denoting stator frame are left out. The equations for currents are linear and time invariant but the mechanical equation is *time periodic*. When compared to Figure 3.1, it can be seen that the time periodic part is in the direct electromechanical feedback. The rest of the model is time invariant.

When the time periodic force component is studied closer, we see that it contains a complex conjugate of the modal vector $\underline{\eta}$. This is the key to remove the time periodic term from the model. If the mechanical displacement, and thus the modal vector, is considered to be a rotating space vector at some angular frequency ω, the force from the time periodic component is

$$F_{tp} \sim |\underline{\eta}|e^{-\mathrm{j}\omega t}e^{\mathrm{j}2(\omega_{\mathrm{s}}t+\varphi_{\mathrm{s}})} = |\underline{\eta}|e^{\mathrm{j}((2\omega_{\mathrm{s}}-\omega)t+2\varphi_{\mathrm{s}})} \tag{3.32}$$

Because the rest of the model is linear and time invariant, the force component will excite a displacement that rotates at an angular frequency of $2\omega_{\mathrm{s}} - \omega$. When this frequency is substituted into the time periodic force component, the angular frequency of the force will be again ω; even the phase will be the same.

$$F'_{tp} \sim |\underline{\eta}|e^{-\mathrm{j}((2\omega_{\mathrm{s}}-\omega)t+2\varphi_{\mathrm{s}})}e^{\mathrm{j}2(\omega_{\mathrm{s}}t+\varphi_{\mathrm{s}})} = |\underline{\eta}|e^{\mathrm{j}\omega t} \tag{3.33}$$

This means that the time periodic component "pairs up" frequencies.

The conclusions above are not entirely true. If the mechanical model is not symmetric in horizontal and vertical directions, a circular rotating force will induce elliptic rotor displacement. An elliptic rotation means that there is a rotational component at negative frequency[2], thus the mechanical model is not linear for rotating space vectors. These negative frequencies are paired

[2]For negative frequencies, the elliptic components are positive.

up with rotation frequencies higher than $2\omega_\mathrm{s}$, thus invoking more frequencies. However, it is later shown in Chapter 6 that only the two frequencies and their elliptic negatives are significant. For some frequencies even the elliptic components could be ignored.

Knowing that the frequencies are excited in pairs, it is possible to make the model LTI system, by adding a new dimension to it. The two frequency components are considered to be in different dimensions. The model equation are written for both the dimensions, thus doubling the number of equations. All the inputs are connected in the first dimension but the output is a sum of the outputs of the two. The time periodic terms couple the dimensions.

To put the previous explanation into equations, we define

$$\underline{\eta} = \underline{\eta}_0 + \underline{\eta}_2^* e^{\mathrm{j}2(\omega_\mathrm{s}t+\varphi_\mathrm{s})} \tag{3.34}$$

and the same for the currents

$$\hat{\underline{i}}_\mathrm{x}^\mathrm{k} = \hat{\underline{i}}_{\mathrm{x},0}^\mathrm{k} + \hat{\underline{i}}_{\mathrm{x},2}^{k*} e^{\mathrm{j}2(\omega_\mathrm{s}t+\varphi_\mathrm{s})} \tag{3.35}$$

Substituting these into equations (3.29), (3.30), and (3.31), gives

$$\begin{aligned}
\hat{\underline{u}}_\mathrm{c}^\mathrm{k} = {} & R_\mathrm{c}\hat{\underline{i}}_{\mathrm{c},0}^\mathrm{k} + R_\mathrm{c}\hat{\underline{i}}_{\mathrm{c},2}^{k*} e^{\mathrm{j}2(\omega_\mathrm{s}t+\varphi_\mathrm{s})} + L_\mathrm{c}\dot{\hat{\underline{i}}}_{\mathrm{c},0}^\mathrm{k} + \mathrm{j}\omega_\mathrm{s}L_\mathrm{c}\hat{\underline{i}}_{\mathrm{c},0}^\mathrm{k} \\
& + L_\mathrm{c}d\hat{\underline{i}}_{\mathrm{c},2}^{k*} e^{\mathrm{j}2(\omega_\mathrm{s}t+\varphi_\mathrm{s})} + \mathrm{j}3\omega_\mathrm{s}L_\mathrm{c}\hat{\underline{i}}_{\mathrm{c},2}^{k*} e^{\mathrm{j}2(\omega_\mathrm{s}t+\varphi_\mathrm{s})} + L_\mathrm{m}\dot{\hat{\underline{i}}}_{\mathrm{r},0}^\mathrm{k} \\
& + \mathrm{j}\omega_\mathrm{s}L_\mathrm{m}\hat{\underline{i}}_{\mathrm{r},0}^\mathrm{k} + L_\mathrm{m}\dot{\hat{\underline{i}}}_{\mathrm{r},2}^{k*} e^{\mathrm{j}2(\omega_\mathrm{s}t+\varphi_\mathrm{s})} + j3\omega_\mathrm{s}L_\mathrm{m}\hat{\underline{i}}_{\mathrm{r},2}^{k*} e^{j2(\omega_\mathrm{s}t+\varphi_\mathrm{s})} \\
& + X_\mathrm{c}\hat{B}_1\left(\boldsymbol{\Phi}\dot{\underline{\eta}}_0 + \mathrm{j}\omega_\mathrm{s}\boldsymbol{\Phi}\underline{\eta}_0 + \boldsymbol{\Phi}\dot{\underline{\eta}}_2{}^* e^{j2(\omega_\mathrm{s}t+\varphi_\mathrm{s})} + j3\omega_\mathrm{s}\boldsymbol{\Phi}\underline{\eta}_2^* e^{j2(\omega_\mathrm{s}t+\varphi_\mathrm{s})}\right)
\end{aligned} \tag{3.36}$$

$$\begin{aligned}
0 = {} & R_\mathrm{r}\hat{\underline{i}}_{\mathrm{r},0}^\mathrm{k} + R_\mathrm{r}\hat{\underline{i}}_{\mathrm{r},2}^{k2} e^{\mathrm{j}2(\omega_\mathrm{s}t+\varphi_\mathrm{s})} + L_\mathrm{r}\dot{\hat{\underline{i}}}_{\mathrm{r},0}^\mathrm{k} + \mathrm{j}\left(\omega_\mathrm{s} - 2\Omega_\mathrm{M}\right)L_\mathrm{r}\hat{\underline{i}}_{\mathrm{r},0}^\mathrm{k} \\
& + L_\mathrm{r}\dot{\hat{\underline{i}}}_{\mathrm{r},2}^{k2} e^{\mathrm{j}2(\omega_\mathrm{s}t+\varphi_\mathrm{s})} + \mathrm{j}\left(3\omega_\mathrm{s} - 2\Omega_\mathrm{M}\right)L_\mathrm{r}\hat{\underline{i}}_{\mathrm{r},2}^{k*} e^{\mathrm{j}2(\omega_\mathrm{s}t+\varphi_\mathrm{s})} + L_\mathrm{m}\dot{\hat{\underline{i}}}_{\mathrm{c},0}^\mathrm{k} \\
& + \mathrm{j}\left(\omega_\mathrm{s} - 2\Omega_\mathrm{M}\right)L_\mathrm{m}\hat{\underline{i}}_{\mathrm{c},0}^\mathrm{k} + L_\mathrm{m}\dot{\hat{\underline{i}}}_{\mathrm{c},2}^{k*} e^{\mathrm{j}2(\omega_\mathrm{s}t+\varphi_\mathrm{s})} \\
& + \mathrm{j}\left(3\omega_\mathrm{s} - 2\Omega_\mathrm{M}\right)L_\mathrm{m}\hat{\underline{i}}_{\mathrm{c},2}^{k*} e^{\mathrm{j}2(\omega_\mathrm{s}t+\varphi_\mathrm{s})} + X_\mathrm{r}\hat{B}_1\Big(\boldsymbol{\Phi}\dot{\underline{\eta}}_0 + \mathrm{j}\left(\omega_\mathrm{s} - 2\Omega_\mathrm{M}\right)\boldsymbol{\Phi}\underline{\eta}_0 \\
& + \boldsymbol{\Phi}\dot{\underline{\eta}}_2{}^* e^{\mathrm{j}2(\omega_\mathrm{s}t+\varphi_\mathrm{s})} + \mathrm{j}\left(3\omega_\mathrm{s} - 2\Omega_\mathrm{M}\right)\boldsymbol{\Phi}\underline{\eta}_2^* e^{\mathrm{j}2(\omega_\mathrm{s}t+\varphi_\mathrm{s})}\Big)
\end{aligned} \tag{3.37}$$

$$\begin{aligned}
& \ddot{\underline{\eta}}_0 + 2\boldsymbol{\Xi}\boldsymbol{\Omega}\dot{\underline{\eta}}_0 + \boldsymbol{\Omega}^2\underline{\eta}_0 + \ddot{\underline{\eta}}_2^* e^{\mathrm{j}2(\omega_\mathrm{s}t+\varphi_\mathrm{s})} + 2\left(\boldsymbol{\Xi}\boldsymbol{\Omega} + \mathrm{j}2\omega_\mathrm{s}\right)\dot{\underline{\eta}}_2^* e^{\mathrm{j}2(\omega_\mathrm{s}t+\varphi_\mathrm{s})} \\
& + \left(\boldsymbol{\Omega}^2 + \mathrm{j}4\omega_\mathrm{s} - 4\omega_\mathrm{s}^2\right)\underline{\eta}_2^* e^{\mathrm{j}2(\omega_\mathrm{s}t+\varphi_\mathrm{s})} = C_\mathrm{F}\hat{B}_1\boldsymbol{\Phi}^T\Bigg(L_\mathrm{m}\left(\frac{\hat{\underline{i}}_{\mathrm{c},0}^\mathrm{k}}{X_\mathrm{c}} + \frac{\hat{\underline{i}}_{\mathrm{r},0}^\mathrm{k}}{X_\mathrm{r}}\right) \\
& + 2\hat{B}_1\underline{\eta}_0 + \hat{B}_1\underline{\eta}_0^* e^{\mathrm{j}2(\omega_\mathrm{s}t+\varphi_\mathrm{s})} + L_\mathrm{m}\left(\frac{\hat{\underline{i}}_{\mathrm{c},2}^{k*}}{X_\mathrm{c}} + \frac{\hat{\underline{i}}_{\mathrm{r},2}^{k*}}{X_\mathrm{r}}\right)e^{\mathrm{j}2(\omega_\mathrm{s}t+\varphi_\mathrm{s})} \\
& + 2\hat{B}_1\underline{\eta}_2^* e^{\mathrm{j}2(\omega_\mathrm{s}t+\varphi_\mathrm{s})} + \hat{B}_1\underline{\eta}_2\Bigg)
\end{aligned} \tag{3.38}$$

from which

$$\begin{aligned}\hat{\underline{u}}_{\mathrm{c}}^{\mathrm{k}} &= R_{\mathrm{c}}\hat{\underline{i}}_{\mathrm{c},0}^{\mathrm{k}} + L_{\mathrm{c}}\dot{\hat{\underline{i}}}_{\mathrm{c},0}^{\mathrm{k}} + \mathrm{j}\omega_{\mathrm{s}}L_{\mathrm{c}}\hat{\underline{i}}_{\mathrm{c},0}^{\mathrm{k}} + L_{\mathrm{m}}\dot{\hat{\underline{i}}}_{\mathrm{r},0}^{\mathrm{k}} + \mathrm{j}\omega_{\mathrm{s}}L_{\mathrm{m}}\hat{\underline{i}}_{\mathrm{r},0}^{\mathrm{k}} \\ &\quad + X_{\mathrm{c}}\hat{B}_1\left(\boldsymbol{\Phi}\dot{\underline{\eta}}_0 + \mathrm{j}\omega_{\mathrm{s}}\boldsymbol{\Phi}\underline{\eta}_0\right)\end{aligned} \tag{3.39}$$

$$\begin{aligned}0 &= R_{\mathrm{c}}\hat{\underline{i}}_{\mathrm{c},2}^{\mathrm{k}} + L_{\mathrm{c}}\dot{\hat{\underline{i}}}_{\mathrm{c},2}^{\mathrm{k}} + \mathrm{j}3\omega_{\mathrm{s}}L_{\mathrm{c}}\hat{\underline{i}}_{\mathrm{c},2}^{\mathrm{k}} + L_{\mathrm{m}}\dot{\hat{\underline{i}}}_{\mathrm{r},2}^{\mathrm{k}} + \mathrm{j}3\omega_{\mathrm{s}}L_{\mathrm{m}}\dot{\hat{\underline{i}}}_{\mathrm{r},2}^{\mathrm{k}} \\ &\quad + X_{\mathrm{c}}\hat{B}_1\left(\boldsymbol{\Phi}\dot{\underline{\eta}}_2 + \mathrm{j}3\omega_{\mathrm{s}}\boldsymbol{\Phi}\underline{\eta}_2\right)\end{aligned} \tag{3.40}$$

$$\begin{aligned}0 &= R_{\mathrm{r}}\hat{\underline{i}}_{\mathrm{r},0}^{\mathrm{k}} + L_{\mathrm{r}}\dot{\hat{\underline{i}}}_{\mathrm{r},0}^{\mathrm{k}} + \mathrm{j}\left(\omega_{\mathrm{s}} - 2\Omega_{\mathrm{M}}\right)L_{\mathrm{r}}\hat{\underline{i}}_{\mathrm{r},0}^{\mathrm{k}} + L_{\mathrm{m}}\dot{\hat{\underline{i}}}_{\mathrm{c},0}^{\mathrm{k}} \\ &\quad + \mathrm{j}\left(\omega_{\mathrm{s}} - 2\Omega_{\mathrm{M}}\right)L_{\mathrm{m}}\hat{\underline{i}}_{\mathrm{c},0}^{\mathrm{k}} + X_{\mathrm{r}}\hat{B}_1\left(\boldsymbol{\Phi}\dot{\underline{\eta}}_0 + \mathrm{j}\left(\omega_{\mathrm{s}} - 2\Omega_{\mathrm{M}}\right)\boldsymbol{\Phi}\underline{\eta}_0\right)\end{aligned} \tag{3.41}$$

$$\begin{aligned}0 &= R_{\mathrm{r}}\hat{\underline{i}}_{\mathrm{r},2}^{\mathrm{k}} + L_{\mathrm{r}}\dot{\hat{\underline{i}}}_{\mathrm{r},2}^{\mathrm{k}} + \mathrm{j}\left(3\omega_{\mathrm{s}} - 2\Omega_{\mathrm{M}}\right)L_{\mathrm{r}}\hat{\underline{i}}_{\mathrm{r},2}^{\mathrm{k}} + L_{\mathrm{m}}\dot{\hat{\underline{i}}}_{\mathrm{c},2}^{\mathrm{k}} \\ &\quad + \mathrm{j}\left(3\omega_{\mathrm{s}} - 2\Omega_{\mathrm{M}}\right)L_{\mathrm{m}}\hat{\underline{i}}_{\mathrm{c},2}^{\mathrm{k}} + X_{\mathrm{r}}\hat{B}_1\left(\boldsymbol{\Phi}\dot{\underline{\eta}}_2 + \mathrm{j}\left(3\omega_{\mathrm{s}} - 2\Omega_{\mathrm{M}}\right)\boldsymbol{\Phi}\underline{\eta}_2\right)\end{aligned} \tag{3.42}$$

$$\begin{aligned}\ddot{\underline{\eta}}_0 + 2\boldsymbol{\Xi}\boldsymbol{\Omega}\dot{\underline{\eta}}_0 + \left(\boldsymbol{\Omega}^2 - 2C_{\mathrm{F}}\hat{B}_1^2\boldsymbol{\Phi}^T\right)\underline{\eta}_0 = \\ C_{\mathrm{F}}\hat{B}_1\boldsymbol{\Phi}^T\left(L_{\mathrm{m}}\left(\frac{\hat{\underline{i}}_{\mathrm{c},0}^{\mathrm{k}}}{X_{\mathrm{c}}} + \frac{\hat{\underline{i}}_{\mathrm{r},0}^{\mathrm{k}}}{X_{\mathrm{r}}}\right) + \hat{B}_1\underline{\eta}_2\right)\end{aligned} \tag{3.43}$$

$$\begin{aligned}\ddot{\underline{\eta}}_2 + 2\left(\boldsymbol{\Xi}\boldsymbol{\Omega} - \mathrm{j}2\omega_{\mathrm{s}}\right)\dot{\underline{\eta}}_2 + \left(\boldsymbol{\Omega}^2 + \mathrm{j}4\omega_{\mathrm{s}} - 4\omega_{\mathrm{s}}^2 - 2C_{\mathrm{F}}\hat{B}_1^2\boldsymbol{\Phi}^T\right)\underline{\eta}_2 = \\ C_{\mathrm{F}}\hat{B}_1\boldsymbol{\Phi}^T\left(\hat{B}_1\underline{\eta}_0 + L_{\mathrm{m}}\left(\frac{\hat{\underline{i}}_{\mathrm{c},2}^{\mathrm{k}}}{X_{\mathrm{c}}} + \frac{\hat{\underline{i}}_{\mathrm{r},2}^{\mathrm{k}}}{X_{\mathrm{r}}}\right)\right)\end{aligned} \tag{3.44}$$

Now the model itself is LTI, but it only gives the components of the modal coordinate vector. The mechanical displacement is given by

$$\underline{z}_{\mathrm{m}} = \boldsymbol{\Phi}\left(\underline{\eta}_0 + \underline{\eta}_2^* e^{\mathrm{j}2(\omega_{\mathrm{s}}t+\varphi_{\mathrm{s}})}\right) \tag{3.45}$$

3.5 State-space model

Equations (3.39)-(3.44) can be formulated into a state-space representation.

$$\begin{aligned}\dot{\underline{\mathbf{x}}} &= \mathbf{A}\underline{\mathbf{x}} + \mathbf{B}\hat{\underline{u}}_{\mathrm{c}}^{\mathrm{k}} \\ \underline{z}_{\mathrm{m}} &= \mathbf{C}_0\underline{\mathbf{x}} + e^{\mathrm{j}2(\omega_{\mathrm{s}}t+\varphi_{\mathrm{s}})}\mathbf{C}_2\underline{\mathbf{x}}^*\end{aligned} \tag{3.46}$$

where $\mathbf{A}$, $\mathbf{B}$, $\mathbf{C}_0$ and $\mathbf{C}_2$ are constant[3] complex matrices and

$$\underline{\mathbf{x}} = \begin{bmatrix} \hat{\underline{i}}_{\mathrm{c},0}^{\mathrm{k}} & \hat{\underline{i}}_{\mathrm{r},0}^{\mathrm{k}} & \dot{\underline{\eta}}_0 & \underline{\eta}_0 & \hat{\underline{i}}_{\mathrm{c},2}^{\mathrm{k}} & \hat{\underline{i}}_{\mathrm{r},2}^{\mathrm{k}} & \dot{\underline{\eta}}_2 & \underline{\eta}_2 \end{bmatrix}^T \tag{3.47}$$

[3] as long as the operation point of the machine stays constant.

If the currents, the control voltage and the displacements are presented in a coordination that rotates with the 2-pole flux, the explicit time dependence can be removed from the state-space model. If the complex model is then made real by breaking the complex variables into real and imaginary part, also the complex conjugate disappears and the model is in standard LTI form. The number of states just doubles.

Using the field coordination means that the mechanical model must be written for the field coordinates. If the mechanical model is symmetric, like assumed, the coordination change causes no problems. However, if the mechanical stiffness is not the same for the horizontal and vertical vibrations, the mechanics becomes time periodic in the field coordinates and thus the whole model. If the state-space model (3.46) is broken into real and imaginary components, it is possible to use a non-symmetric mechanical model without changing the model structure.

The state-space representation (3.46) is only a dynamic model that describes how the control voltage affects the currents and displacements. That still leaves the problem with the shape, $\underline{z}_\mathrm{s}$ in Equation (3.27), and the other disturbance forces. The shape itself could be just added to the output of the model, the forces caused by the shape are more problematic.

When building a model for the disturbance forces, one has to consider what can be measured. Calculating the force caused by the shape with the equation presented is pointless if it is not possible to separate the deformation of rotor from systematic measuring errors. The magnetic forces depend on the displacement of the rotor core and that can not be measured directly because sensors cannot be put inside the machine.

The disturbance forces can be modeled as an input force that affects the third state of $\underline{\mathbf{x}}$ in (3.46). The displacement from deformation would also affect the currents but the total effect is reduced to the mechanical equation. Most of the disturbance forces are caused by rotation and thus it is reasonable to assume that the forces are mostly on rotation frequency. The disturbance can be represented as sum of sinusoidal forces. The frequency content of the disturbance consists of harmonics of the rotor's rotation frequency, the 2-pole supply frequency and their combinations. When the machine is not loaded, the supply frequency and rotation frequency are almost the same.

The simplest state-space model for the disturbance force would be

$$\dot{\underline{\mathbf{x}}}_d = \begin{bmatrix} 0 & 1 & 0 & 0 \\ -\Omega_\mathrm{M}^2 & 0 & 0 & 0 \\ 0 & 0 & 0 & 1 \\ 0 & 0 & -\Omega_\mathrm{M}^2 & 0 \end{bmatrix} \underline{\mathbf{x}}_d \tag{3.48}$$

$$\underline{F}_d = \begin{bmatrix} 0 & 1 & 0 & 0 \\ 0 & 0 & 0 & 1 \end{bmatrix} \underline{\mathbf{x}}_d$$

The disturbance model has no input so the output depends on the initial state. For control purposes, this model is still adequate.

Chapter 4

Control algorithms

4.1 LQ-control

All controllers to be used to control the radial vibrations of the rotor in this thesis are model-based. The state space models discussed in Section 3.5 were the starting point for controller design. In the next chapter, Section 5.2.3, it is described how numerical values were obtained for the models.

$$\begin{aligned} \dot{\underline{\mathbf{x}}} &= \mathbf{A}\underline{\mathbf{x}} + \mathbf{B}\underline{\mathbf{u}} \\ \underline{\mathbf{y}} &= \mathbf{C}\underline{\mathbf{x}} \end{aligned} \tag{4.1}$$

Probably the simplest model-based controller is a linear state feedback, built on a time independent model. The time periodic part of the model is simply ignored. The model is used to estimate the state vector $\underline{\mathbf{x}}$ for the machine and the control voltage is then defined by

$$\underline{\mathbf{u}} = -\mathbf{L}\hat{\underline{\mathbf{x}}} \tag{4.2}$$

where $\mathbf{L}$ is some constant feedback gain matrix and $\hat{\underline{\mathbf{x}}}$ the estimate for the state vector.

The feedback gain matrix can be chosen so that it minimizes a quadratic cost function J_c; thus the name Linear Quadratic (LQ) control. The cost function can be defined as

$$J_c = \int_0^\infty \left(\underline{\mathbf{x}}^T\mathbf{Q}\underline{\mathbf{x}} + \underline{\mathbf{u}}^T\mathbf{R}\underline{\mathbf{u}}\right) \mathrm{d}t \tag{4.3}$$

where $\mathbf{Q}$ and $\mathbf{R}$ are weight matrices. For the minimization to have a solution, $\mathbf{Q}$ must be positive semi-definite and $\mathbf{R}$ positive definite. Both should also be chosen to be symmetric.

Choosing appropriate weight matrices is another problem. To keep things simple, $\mathbf{Q}$ and $\mathbf{R}$ can be chosen to be diagonal matrices. Then, the diagonal values of $\mathbf{Q}$ are the weights for individual state variables and the diagonal values of $\mathbf{R}$ are the weights for the control voltage. The $\mathbf{R}$ matrix can actually be chosen as an identity matrix because the cost function (4.3) can be scaled with any constant factor without changing the "location" of the minimum. In this case, there is no need to weight some control input more then others. Thus, only the weights for the state have to be chosen.

The weights can be placed only to those states that directly affect the rotor displacement. Those states are known from the physical model, see Equation (3.47), or, in case that the equations (3.39)-(3.44) cannot be separated during identification, they can be determined from the $\mathbf{C}$ matrix of

the model.[1] Increasing the weights on state variables will bring them closer to zero on the optimal solution but it will also cause the relative weight of the control input to decrease, leading to a higher control voltage.

The defined cost function (4.3) is minimized for the model. The technique is explained thoroughly in (Lewis & Syrmos 1995). The feedback gain matrix $\mathbf{L}$ that optimizes (4.3) is given by

$$\mathbf{L} = \mathbf{R}^{-1}\mathbf{B}^T\mathbf{S} \tag{4.4}$$

where $\mathbf{S}$ is the solution of the Riccati equation

$$\mathbf{A}^T\mathbf{S} + \mathbf{S}\mathbf{A} - \mathbf{S}\mathbf{B}\mathbf{R}^{-1}\mathbf{B}^T\mathbf{S} + \mathbf{Q} = 0 \tag{4.5}$$

The matrix $\mathbf{S}$ is positive definite and symmetric.

The estimate for the state vector $\underline{\mathbf{x}}$ is obtained from a state-observer, which is basically a Kalman filter (Harvey 1991) with constant gain. The model output is compared to the measured output of the system and the error is used to update the estimated model state $\underline{\hat{\mathbf{x}}}$.

$$\dot{\underline{\hat{\mathbf{x}}}} = \mathbf{A}\underline{\hat{\mathbf{x}}} + \mathbf{B}\underline{\mathbf{u}} + \mathbf{K}\left(\underline{\mathbf{y}} - \mathbf{C}\underline{\hat{\mathbf{x}}}\right) \tag{4.6}$$

The matrix $\mathbf{K}$ is the Kalman gain[2].

To make the model output comparable with the measured output of the system, the disturbance model has to be included in the observer. There are at least two ways to do it. If possible, the disturbance should be modeled as a force and the combined model for the system would be

$$\begin{aligned} \begin{bmatrix} \dot{\underline{\hat{\mathbf{x}}}} \\ \dot{\underline{\hat{\mathbf{x}}}}_\mathrm{d} \end{bmatrix} &= \begin{bmatrix} \mathbf{A} & \mathbf{B}_\mathrm{m}\mathbf{C}_\mathrm{d} \\ 0 & \mathbf{A}_\mathrm{d} \end{bmatrix} \begin{bmatrix} \underline{\hat{\mathbf{x}}} \\ \underline{\hat{\mathbf{x}}}_\mathrm{d} \end{bmatrix} + \begin{bmatrix} \mathbf{B} \\ 0 \end{bmatrix} \underline{\mathbf{u}} \\ \underline{\hat{\mathbf{y}}} &= \begin{bmatrix} \mathbf{C} & 0 \end{bmatrix} \begin{bmatrix} \underline{\hat{\mathbf{x}}} \\ \underline{\hat{\mathbf{x}}}_\mathrm{d} \end{bmatrix} \end{aligned} \tag{4.7}$$

The problem with this combined model is the matrix $\mathbf{B}_\mathrm{m}$ which defines the location of the mechanical equations in the $\mathbf{A}$ matrix. The matrix $\mathbf{B}_\mathrm{m}$ can be derived from Equations (3.39)-(3.44), but it requires that the identification of the model manages to separate the equations from each other. Because the forces cannot be measured, the separation is quite a challenge. Therefore another approach is needed.

[1] The identified model can have different state variables which are linear combinations of the physical ones. The $\mathbf{C}$ matrix reveals the linear combination for the mechanical modal vectors.

[2] Also $\mathbf{L}$ can be called the Kalman gain in some context.

Because the model is linear, the disturbance force can be reduced to a completely independent displacement. The model for the disturbance is so simple that it can be used for both the force and displacement. When the disturbance is added as a displacement, the combined model does not require any new matrices.

$$\begin{bmatrix} \dot{\hat{\underline{\mathbf{x}}}} \\ \dot{\hat{\underline{\mathbf{x}}}}_d \end{bmatrix} = \begin{bmatrix} \mathbf{A} & 0 \\ 0 & \mathbf{A}_d \end{bmatrix} \begin{bmatrix} \hat{\underline{\mathbf{x}}} \\ \hat{\underline{\mathbf{x}}}_d \end{bmatrix} + \begin{bmatrix} \mathbf{B} \\ 0 \end{bmatrix} \underline{\mathbf{u}} \tag{4.8}$$
$$\hat{\underline{\mathbf{y}}} = \begin{bmatrix} \mathbf{C} & \mathbf{C}_d \end{bmatrix} \begin{bmatrix} \hat{\underline{\mathbf{x}}} \\ \hat{\underline{\mathbf{x}}}_d \end{bmatrix}$$

The observer equation (4.6) must be written for the extended model. The Kalman gain matrix $\mathbf{K}$ can be optimized in a similar fashion as the feedback gain matrix $\mathbf{L}$. The system to be optimized would be

$$\dot{\tilde{\underline{\mathbf{x}}}} = \tilde{\mathbf{A}}\tilde{\underline{\mathbf{x}}} + \mathbf{K}\tilde{\mathbf{C}}\tilde{\underline{\mathbf{y}}} \tag{4.9}$$

where $\tilde{\mathbf{A}}$ and $\tilde{\mathbf{C}}$ are matrices of the extended model, $\tilde{\underline{\mathbf{y}}}$ is the output error and $\tilde{\underline{\mathbf{x}}}$ the state error defined as

$$\tilde{\underline{\mathbf{x}}} = \underline{\mathbf{x}} - \hat{\underline{\mathbf{x}}} \tag{4.10}$$

Now, the $\mathbf{K}$ and $\tilde{\mathbf{C}}$ matrices are in wrong order for the same quadratic cost function optimization to be used directly. However, the $\mathbf{K}$ matrix can be optimized for the transposed system

$$\dot{\tilde{\underline{\mathbf{x}}}}_T = \tilde{\mathbf{A}}^T\tilde{\underline{\mathbf{x}}}_T + \tilde{\mathbf{C}}^T\mathbf{K}^T\tilde{\underline{\mathbf{y}}} \tag{4.11}$$

The cost function for the transposed observer can be defined as

$$J_o = \int_0^\infty \left(\tilde{\underline{\mathbf{x}}}_T^T\mathbf{Q}\tilde{\underline{\mathbf{x}}}_T + \tilde{\underline{\mathbf{y}}}^T\mathbf{R}\tilde{\underline{\mathbf{y}}}\right) \mathrm{d}t \tag{4.12}$$

Vector $\tilde{\underline{\mathbf{x}}}_T$ is the state error of the transposed system.

Although (4.9) and (4.11) are not the same system, they have the same eigenvalues and therefore the same dynamic properties. Therefore this method gives a good enough value for $\mathbf{K}$ without much effort, since very powerful tools exist for solving Equation (4.5). This method has been presented in (Orivuori 2008), where also simulation results have been presented.

The state observer can be used with other controllers as well. It is also possible to estimate only some of the states. If the disturbance were modeled

as a force, it is possible to estimate the total force on the rotor and try to control the forces directly, not just the rotor displacement.

For implementation, the LQ-controller was discretized with *zero order hold* (Franklin, Powell & Workman 1998). The sampling time for the test system was 5 kHz. A more sophisticated tuning of LQ-controller for the same system has been presented in (Orivuori 2008).

4.2 Convergent Control

4.2.1 Space vector control

If the disturbance force appears on one frequency only, as assumed here, the control voltage also needs to have only one frequency. Of course, it must also be assumed that the system is LTI. If a sinusoidal control voltage is fed with a right phase and amplitude, it should cancel the disturbance force completely. It is possible to design a control algorithm that aims to find the correct phase and amplitude for the control voltage.

The induction machine here is a special case. The disturbance is not just sinusoidal but can be represented as rotating complex vector. The control voltage is also a complex vector. Rotation of the disturbance vector is tied to the rotation of the rotor, which means that the complex disturbance force vector is constant in a coordinate system that rotates with the rotor. Thus in rotor coordinates, the perfect control voltage is just one constant complex number.

The LTI model, Equation (4.1), can be used to calculate the force or displacement caused by the control voltage. In rotor coordinates, the system only amplifies and changes the direction of the control vector. It can be reduced into one complex multiplier, g. Thus the system can be inverted in one frequency, and it is possible to directly calculate the perfect control, if the disturbance vector is known.

The disturbance does not have to be known; the measurements can be used directly. Since the system can be inverted for one frequency, it is possible to directly calculate the control signal that would cancel the measured displacement. The problem is that, when the control algorithm makes the displacement disappear, the control signal goes to zero. The effect of control voltage must be taken into account when calculating the displacement to be canceled, since the control effect is shown in the measurements.

There is always some delay or transient dynamics so the control voltage being calculated is not the same as the one that shows in the measured displacement. Otherwise the controller would break causality. Since the

controller is going to be discretized, it is possible to simply use the control signal from the previous time step to calculate it in the next one. Therefore, the perfect control would be

$$\underline{u}_{k+1} = -g^{-1}\left(\underline{Z} - g\underline{u}_k\right) \tag{4.13}$$

where $\underline{Z}$ is the measured output of the system in the rotor coordination.

Before studying the stability of (4.13), it has to be noticed that the model has some phase and magnitude error. Let us assume that the modeled complex multiplier for the system is a product of the actual multiplier, g, and model error multiplier, g_δ. With the model error included, the perfect control (4.13) becomes

$$\underline{u}_{k+1} = \gamma\underline{u}_k - \alpha g^{-1} g_\delta^{-1}\underline{Z} \tag{4.14}$$

Artificial factors γ and α have been added to the control law to help to adjust the stability. The same factors were used in (Tammi 2007).

Let us assume for now that the measured system output consists of only the effect of the control and the disturbance $\underline{D}_k$ on one frequency only.

$$\underline{Z}_k = g\underline{u}_k + \underline{D}_k \tag{4.15}$$

The subscript k denotes time stepping. Since the only excitation has only one frequency, so does the control voltage. The issue with more frequencies is treated in Section 4.2.3.

The stability of the control can be studied by combining (4.15) and (4.14).

$$\begin{aligned}
\underline{Z}_{k+1} &= g\underline{u}_{k+1} + \underline{D}_{k+1} \\
&= g\left(\gamma\underline{u}_k - \alpha g^{-1} g_\delta^{-1}\underline{Z}_k\right) + \underline{D}_{k+1} \\
&= \gamma\left(\underline{Z}_k - \underline{D}_k\right) - \alpha g_\delta^{-1}\underline{Z}_k + \underline{D}_{k+1} \\
&= \left(\gamma - \alpha g_\delta^{-1}\right)\underline{Z}_k + \left(\underline{D}_{k+1} - \gamma\underline{D}_k\right)
\end{aligned} \tag{4.16}$$

If $\gamma = 1$ and $\underline{D}_k$ constant, the disturbance is completely removed from the measured output. The stability of the control depends on the model error.

$$|\gamma - \alpha g_\delta^{-1}| < 1 \tag{4.17}$$

If $\gamma = 1$, the phase error of the model must less than 90 degrees, but it still puts some restrictions on α. The two parameters can always make the control stable. Reducing γ also allows over 90 degree phase errors but leaves more

disturbance unbalanced. Reducing α allows more phase error but makes the control converge slower. Figure 4.1 illustrates the stability condition.

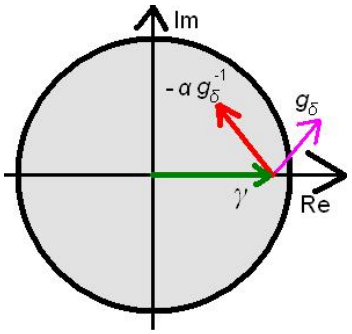

Figure 4.1: Controlled system is stable as long as the red arrow stays within the unit circle. The green arrow γ is the leakage factor and g_δ the model error factor. When the model error is zero, g_δ is a unit vector pointing towards the positive real axis.

4.2.2 CC in general case

The control algorithm presented in the previous section is known as *convergent control*, *CC*, (Burrows & Sahinkaya 1983) (Keogh, Cole & Burrows 2002). It can be generalized to cover also real systems with sinusoidal disturbances and multiple inputs and outputs. For multiple sinusoidal signals the control law would be

$$\underline{U}_{k+1} = \gamma \underline{U}_k - \alpha g^{-1} \left(z_k e^{-j\omega kT} \right) \tag{4.18}$$

where T is the length of time step, ω the frequency of known disturbance, and z_k is now a vector of measured signals. The stability condition (4.17) still holds but the question is, what is g for this general case.

Let us assume that the control is zero at $k = 0$.

$$\underline{U}_0 = 0 \tag{4.19}$$

Solving the control signal from (4.18) for time step n gives

$$\underline{U}_n = -\alpha g^{-1} \sum_{k=0}^{n} z_k e^{-j\omega kT} \tag{4.20}$$

with the assumption $\gamma = 1$. The sum term looks exactly like the definition of the Discrete Fourier Transformation for frequency ω, and it can be claimed that

$$\lim_{n\to\infty} \underline{U}_n = -\alpha g^{-1} \mathfrak{F}\{z\}(\omega) \tag{4.21}$$

Note that in (4.20), if the average of the product inside the sum does not go to zero, the amplitude of the control signal will keep rising. Thus, the convergent control can be said to be an integrating controller. If the controller is designed for zero frequency, all the coordination transformations can be left out and the controller is simply a discrete integrator. Having $\gamma < 1$ weakens the integrating effect.

The complex multiplier g is now a matrix. The definition was that it describes how the phases and amplitudes of the output, represented as complex numbers, change as a function of phase and amplitude of the control voltage. For frequency ω, this can be obtained from the system's transfer function G as

$$g = G(j\omega) = \mathbf{C}\left(j\omega I - \mathbf{A}\right)^{-1}\mathbf{B} \tag{4.22}$$

$\mathbf{A}$, $\mathbf{B}$, and $\mathbf{C}$ are the matrices of the LTI state-space model (4.1). Although the analysis was done for the special case in previous Section 4.2.1, it holds for the general case as well.

The convergent control algorithm (4.18) calculates the control signal in frequency domain. The signal still has to be converted into a real voltage. With a complex displacement and control voltage (in Section 4.2.1) the only conversion needed is to transform the space vector of control voltage back to the original frame of reference. In a general case, a vector of complex variables needs to be transformed into real sinusoidal signals.

The complex variables in $\underline{U}$ describe the amplitudes and phases of the control voltage inputs. In electrical engineering, such variables are often used and are called *phasors*. The phasors usually represent cosine waves of voltages and currents. The angular frequency of the cosine waves is ω. The phasors can be converted into time domain by

$$u(t) = |\underline{U}|\cos(\omega t + \angle\underline{U}) = \mathrm{Re}\{\underline{U}e^{j\omega t}\} \tag{4.23}$$

Thus, the real control voltage is given by

$$u_k = \mathrm{Re}\{\underline{U}_k e^{j\omega kT}\} \tag{4.24}$$

In some papers, there is a factor 2 in front of the realization (4.24), e.g. (Lantto 1999) (Tammi 2007). It might be some historic relic since the factor is not needed. It can be included into the parameter α of Equation (4.18)

anyway. Although, some further analysis looks prettier if the 2 is kept there for convenience.

Using the general convergent control instead of the space vector control, gives more degrees of freedom. Each output is controlled separately. In practice, it means that the general CC also controls a space vector rotating to the other direction and can attenuate elliptic disturbances.

In practice, the term ωkT in Equations (4.18) and (4.24) should be replaced with an angle. Best results are achieved when the measured rotor angle is used. If ω is set to be a constant and the real disturbance frequency is not, the controller could end up operating at a wrong frequency. If only the disturbance frequency can be measured, the angle should be integrated from it. Having the index parameter k explicitly in the equations should be avoided.

4.2.3 Multiple frequencies

Section 4.2.1 derived the stability condition for CC when the system output has only one frequency. The stability in a general case is much more difficult to show and it has not been done yet. It is possible to derive a discrete equivalent feedback system for CC, so the stability can be studied for any given system. The equivalent feedback has been presented (Tammi 2007).

If we consider a case in which the disturbance is not at the frequency for which the controller was designed, the model error becomes

$$G_\delta(j\omega) = G_{\delta 0} G(j\omega_d) G^{-1}(j\omega) \tag{4.25}$$

where $G_{\delta 0}$ is the error at the designed frequency ω_d. The effective model error depends on the frequency of the disturbance.

According to the stability condition (4.17), if $\gamma = 1$, the phase error of the model has to be less than 90 degrees. If the system has at least 3 poles more than zeros and none of the poles are at zero, the phase shifts in total 270 degrees as a function of frequency. Thus, there is always a frequency at which the phase error is more than 90 degrees. The control should then be unstable with any α but empiric studies have shown that it is not the case.

If the time step is small enough, the control frequency will be the same as the disturbance frequency. From (4.20) it can be seen that if the system output z_k is not at the frequency the controller was designed for, ω, the control signal approaches to zero. That is, if the system stays stable during the beginning transient, when the controller is switched on or the disturbance appears. With small α, the control signal builds up slowly, giving time for the transient to pass.

It has not been theoretically proven, but if α is chosen small enough, at least smaller than the time step used, the controller will be stable as long as the system itself is stable[3]. The controller works only at very narrow frequency band around its designed frequency and does practically nothing to other frequencies. Thus, if the system has poles in the right side of complex plane, the controller cannot stabilize the closed loop system.

Because the CC practically controls only one frequency and ignores the rest, several of them can be used in parallel to control multiple disturbance frequencies. The controllers do not interfere with each other. Another good feature of the CC is that it only requires a system model for the disturbance frequencies. A complete dynamic model is not needed.

In Chapter 3, plenty of pages were used to derive a time periodic model for the system and in this chapter the models used have been LTI. The CC works well also with LTP systems. The harmonic frequencies caused by the sinusoidal control signal of one controller can be removed with another controller. The CC assumes nothing about what is causing the disturbance. The only danger is that two controllers can start oscillating if they both act as a disturbance source for each other. This problem can be dealt with by making one of the controllers faster than the other by using different values for the parameter α.

4.3 Combined control

The two controllers presented can be combined. The LQ can be used for wide-band control of the rotor vibration and the CC to attack the known disturbances. The CC should be designed for the rotation speed and maybe for the first few harmonics.

The CC can be designed for the field coordination[4] but the LQ cannot. In the field coordination, the disturbance on rotation speed appears at the slip frequency. The elliptic part of the disturbance is at the sum of rotation frequency and field frequency. If the machine is not loaded, the slip is so small that the main disturbance component is almost at 0 Hz. The disturbance model used by the LQ cannot be designed for 0 Hz and works poorly at very low frequencies. Thus, k-coordination should be used for the combined controller.

The CC and LQ can be designed independently and placed parallel to each other. Meaning that the CC can be designed for the uncontrolled process and

[3]The stability for the actuator model has been shown with simulations and measurements.

[4]Frame of reference that rotates with the 2-pole magnetic field.

yet the control signal from CC does not have to be connected to the observer used by the LQ. The reason why this works is that the disturbance model in the observer of the LQ is adaptive. The observer has no prior knowledge of the magnitude and phase of the disturbance. Since the CC operates on only this frequency, the disturbance model can adapt to the effect the CC has on the measurements.

If the $\mathbf{B}_\mathrm{m}$ matrix in Equation (4.9) can be identified, it is possible to use the observer to estimate the forces exerted on the rotor and use the CC to control them directly. A slightly modified version of such a controller has been presented in (Zenger et al. 2008). However, the background of that controller has been explained a bit differently.

Both the CC and LQ are based on a model that was derived assuming that the amplitude of the 2-pole flux density and the rotation speed of the machine stay constant. Still, there is a need for a controller that could operate at different operation points. If a physical model can be identified for the machine, the model can be obtained as a function of the flux density and rotation speed. The only problem remaining is how to solve the Riccati equation (4.5) for the LQ. If the physical model cannot be obtained, there is plenty more problems to be solved.

The operating frequency of CC can be taken from the measurements directly but, if the operating frequency moves away from the designed frequency, the model error increases as seen from Equation (4.25). The model used by the CC has only four complex valued parameters. If there was a way to separate the disturbance from the effect of the control online, the model could be identified online and an adaptive controller could be designed.

Making the LQ adaptive is a much more challenging task. It is possible, though, to set the poles of the observer and LQ so that the closed-loop system stays stable even when the operation point changes. In that case, the poles cannot be optimized for any particular frequency and the control result might not be very good.

Chapter 5

Verification

5.1 Measurement set-up

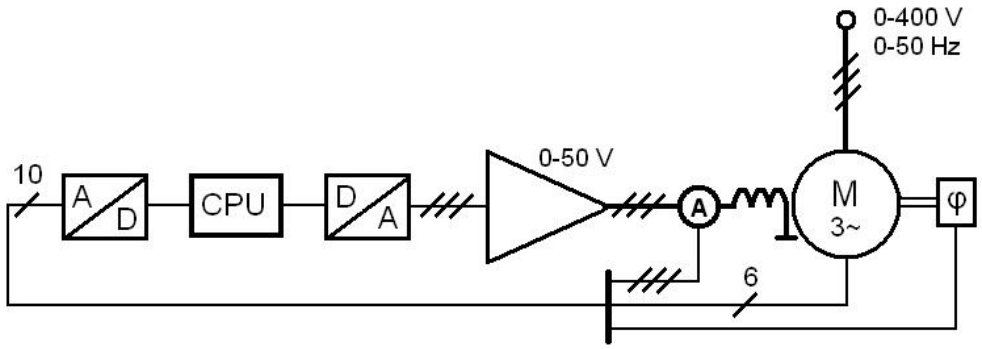

Figure 5.1: Measurement lay-out. The 6 measurement signals from the machine are; the rotor displacements (x- and y-direction), 2-pole flux (2 phases), and 4-pole flux (2 phases). Control signals computed by CPU are amplified and fed to the extra windings. The extra winding currents are measured as well as the rotor angle.

Figure 5.1 shows the lay-out of the measurement set-up. The induction machine is powered from a 750 kVA adjustable generator. The rotor displacements are measured from the rotor shaft and the 2- and 4-pole fluxes from inside the machine. The measurements are converted to digital signals for the processor that runs the control algorithms. The processor calculates the control voltages for all three phases of the 4-pole control winding. The voltages are converted to analog signals and amplified before fed into the machine. The control winding currents are also measured as well as the rotor angle.

5.1.1 Test machine

The active vibration control methods studied in this research are meant to be used for large electrical machines. Since bigger machines are more expensive and potentially a lot more dangerous[1], the measurements and testing are done with a smaller machine. The test machine, shown in Figure 5.2, was built from a standard 30 kW 3-phase cage induction machine made by ABB. Both the stator and rotor of the machine were taken out and replaced with customized versions. Thus, the rated values for the actual test machine were undefined.

[1]If for example the controller develops a malfunction at critical speed.

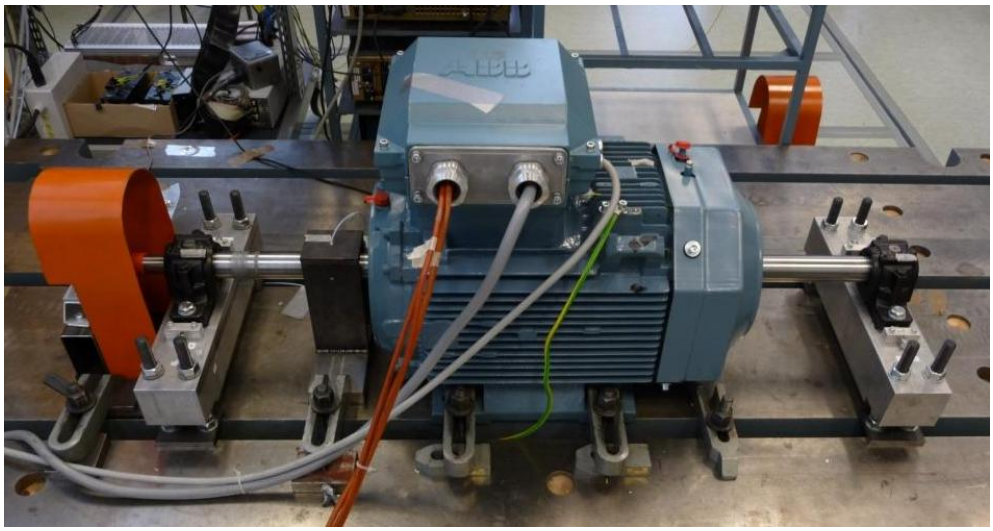

Figure 5.2: The test machine. The rotor is supported by external bearings. The displacement measurement rack can be seen on the left side of the machine. The three orange wires at going into the machine's terminal box at left are the main supply lines. The thick line next to them brings out all measurements from inside the machine. The third line going to the terminal box is the extra winding supply line. The one in the most right grounds the machine frame.

The stator for the test machine was completely rebuilt. The original machine had two parallel 2-pole windings. In the new stator, the 2-pole windings were installed in series. Approximately 10% less copper was used for the new winding. Thus, the rated power had to be dropped or the machine would overheat.

Less copper was used for the main winding to make room for the extra winding that would be used to create controlled radial forces to the rotor. The extra winding had 4-poles and it was wound in the same stator slots as the main winding. The extra winding was significantly thinner than the main winding and had more turns. Besides the main and extra winding, two measurement windings were also placed in the stator slots. The other was a 2-phase 2-pole winding to measure the 2-pole magnetic flux and the other one 2-phase 4-pole winding to measure the 4-pole magnetic flux inside the machine.

Like in the old stator, the main winding was connected to delta. Each of the three phases of the extra winding were supplied separately. The low voltage ends of the extra windings were connected to ground by the voltage

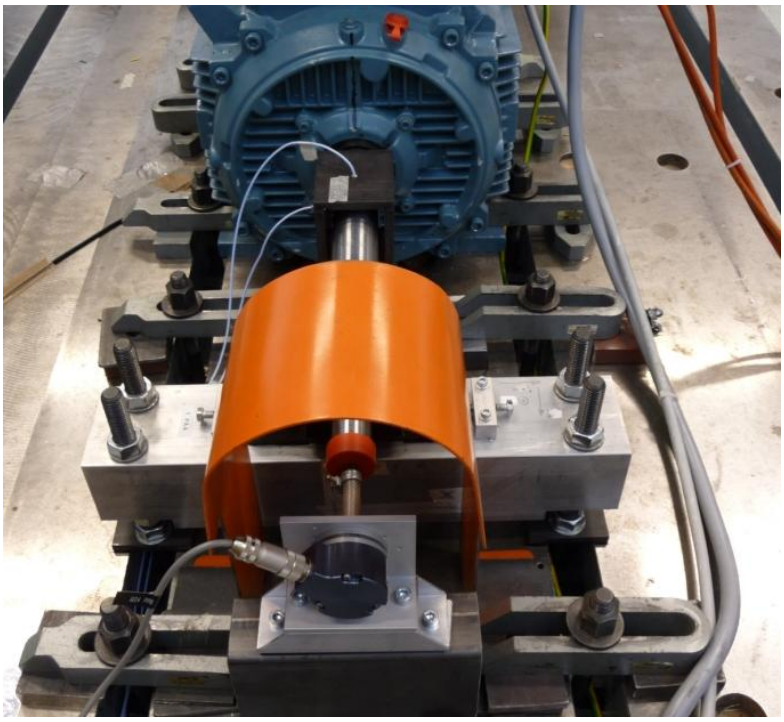

Figure 5.3: Test machine from the drive end. The displacement measurement rack is shown in front of the machine. The tacho meter is shown at the bottom of the picture.

supplies but the connection set no limits for the currents.

The new rotor had an identical core to the old rotor, but in the new one the rotor shaft was longer and thinner[2]. The rotor shaft came about 400 mm out of the machine from both sides. In the original machine, the shaft only came out from the drive end. On the other side there was a fan covered with grating. For the test machine, the grating was broken and the rotor shaft pushed through it.

The rotor was placed on external bearings that were designed to allow the rotor to bend. The bearings had two set of ball bearings that allowed extra degree of freedom. The bearings span was 1220 mm. It would have been too risky to have the rotor only on external bearings; therefore, safety bearings were placed to the machines end shields where the actual bearings normally are. The gap between the rotor shaft and the safety bearings was about 0.5 mm.

The purpose of the longer and weaker rotor was to reduce the critical

[2]Diameter of the rotor shaft was less then 50 mm, the total length was 1500 mm.

frequency[3] and to enhance the effect of radial rotor forces. Somewhere during the manufacturing, the rotor sustained some damage and became more eccentric than normal. Given the purpose of the research, this was not necessarily a disaster but it caused some practical problems. The rotor shaft was so flexible that when the machine was running at slow speed, the magnetic field pulled the rotor to the safety bearings from the direction, where the air gap was shortest. The magnetic flux of the machine needed to be weakened in order to run the machine without vibration control.

5.1.2 Sensors

The rotor displacement was measured using eddy-current sensors (Holmgren, Hasling & Denny 1979) (Brauer 2006), seen as light blue wires in Figure 5.3. Two sensors were positioned on the rotor shaft 90 mm from the end shield on the side of the load. The sensors where placed in custom-made frame that put the sensors in 90 degree angle to each other. One of them was placed vertically to measure in y-direction, the other horizontally to measure in x-direction. The coordinate system was defined so that the rotor rotated in the direction of increasing angle. The directions are shown in Figure 5.4.

The eddy current sensors had their own converters and amplifiers that gave the distance between the rotor shaft and the sensor as a voltage signal. The voltage was between 0 V and 24 V and was linearly dependent on the distance. The measurement information was passed to the control program through an AD-converter port. The maximum voltage for the converter port was 10 V so the signals where first routed through a voltage reducer box. The operating voltage for the measurement amplifiers was provided with batteries to prevent ground loops.

To measure the machine's magnetic flux, measuring coils were constructed inside the machine into the stator slots. Two coils with two turns were used to measure the 2-pole flux and other two coils with 10 turns measured the 4-pole flux. The 2-pole field measurement windings were connected to the AD-converter ports through the voltage reducer and the 4-pole field measurements directly. The measuring coils were originally meant to be used to calculate the electromagnetic force exerted on the rotor, see Section 3.1, but that did not work out as planned. The 2-pole field measurement was used to get the angle of the main flux in the machine. The angle was used in coordination transformations and for modulating the control voltage.

The angle of the rotor was measured with a pulse tachometer. The

[3]The lowest mechanical bending frequency of the rotor was to be around 37 Hz. Measurements were done before the rotor was installed into the machine.

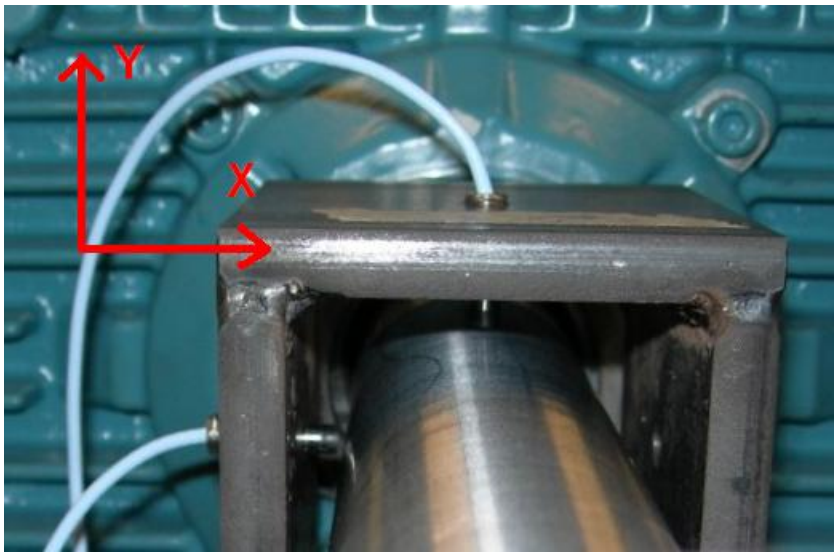

Figure 5.4: The eddy current sensors were placed less than 1 mm away from the rotor shaft. The sensors measure distance. The defined direction are plotted as arrows. The rotor rotates from x to y, i.e. counter-clockwise.

tachometer gave two sets of 1024 pulses per revolution and it was connected to a digital encoder card. The card was able to update the rotor angle information 4096 times per revolution as it used rising and falling edges of both the pulse signals. The signals had 90 degree phase shift (van Dam & Immink 1980). The used software made the angle available for the control algorithms. Because of delays and 5 kHz sampling the resolution of the angle information was not 360 / 4096 degrees.

The currents of the extra winding were measured with shunt resistors connected to each phase. The shunts were placed on the low voltage side of the control voltage supply, so that the voltage measurement over them could be connected to the same ground as the control voltage supply. The voltages were measured directly with the AD-converters. The resistances of the shunts were approximately 0.3 Ω whereas the measured phase resistances of the extra winding were over 14 Ω.

5.1.3 Actuator

The control force was produced with the 4-pole extra winding built into the machine. The winding was voltage driven and the voltage was taken from DA-converters and amplified with analog power amplifiers. The DA-

converter ports gave voltage from -10 V to +10 V and the range of the amplifier output was from -100 V to +100 V. The range was dropped to ±50 V by adding 10 kΩ front resistors between the DA-ports and the amplifiers (Sedra & Smith 2004). The amplifiers also allowed a current limit to be set to prevent accidental overheating of the windings.

Each of the three phases of the extra winding had their own DA-converter and amplifier allowing the voltages to be controlled separately without limitations. The signal grounds of input and output port of the amplifiers where internally connected together and the signal grounds of the DA-converters where internally connected to the protective ground. In this way, the other ends of the extra windings were at the same potential.

Originally the control voltage was to be provided with a small frequency converter (Rashid 2004) to better replicate the bigger machines. Because the test machine was small and the control voltages needed low, there was no way to accurately produce the control voltage with a frequency converter. One frequency converter was tested with voltage reducing transformers (and without) but the transformers quickly overheated. The problem was that the control frequencies are too low for transformers to be used (Wildi 2006). It was though shown that the machine can be controlled with pulse-like voltages. Thus, there is nothing fundamental preventing the use of frequency converters, just the voltage level was too high.

5.1.4 Power supply

The test machine was driven with 750 kVA synchronous generator. The generator was rotated with 60 kW direct current motor that was supplied with a thyristor bridge from the grid. This setup allowed the frequency and amplitude of the supply voltage to be controlled separately. Controlling the amplitude of the supply voltage, the magnitude of the magnetic flux inside the machine could be altered. The rotation speed of the direct current motor, and that of the generator connected to it, was defined by the current delay angle of the thyristor bridge. The generator had three pole pairs, so the supply frequency was three times the rotation speed of the converter machines. Magnetization of the synchronous generator defined the amplitude of the voltage.

As explained in Section 5.1.1, the test machine was customized and partly damaged. Connecting the machine directly to the grid could have been fatal. Before it was clear that the vibration control was working, the machine was only driven with low rotation speeds. The ability to control the amplitude of the voltage was also crucial since the nominal field strength pull the slack rotor to the safety bearings.

The used synchronous generator was huge compared to what was needed but it was the only accurately adjustable generator available that could be operated with low frequencies. Still, the rotation speed could not be lowered too much or the bearings of the generator could have been broken. The rotor of the generator was so heavy and the machine was not designed to rotate slowly. The minimum rotation speed used was about 2.75 Hz which gave supply frequency of 8.3 Hz.

The test machine was supposed to be driven with frequency converter but that caused some practical problems. When frequency converter supply was tested, the switching frequency of the converter was somehow induced also in the extra windings. The most likely reason for that was that since the windings were in same stator slots, they were capacitively coupled. The sharp edges of the voltage pulses given by the frequency converter caused voltage spikes to the extra windings.

The voltage spikes were so narrow that their effect on the produced force was marginal. However, the spikes peeked over 60 V which was more than enough to disturb the measurements. But the noise in the measurement signals was not the problem. The high-frequency spikes passed through the power amplifiers and could be detected at the output ports of the DA-converters. The maximum voltage the ports were designed to withstand was 15 V and the high voltage spikes were breaking the channels. The peek values of the spikes where lowered to safe levels with filters but they still disturbed the control signal.

If the control signal was also supplied from a frequency converter, the spikes would cause no problems. The analog amplifiers gave in to the spikes but frequency converter should be able to hold its voltage. How this would affect the losses of the converters was not considered. Since the control voltage supply was already changed to analog, the other frequency converter was abandoned as well. It was decided to keep the measurement setup as ideal as possible until the controllers were working.

5.1.5 Control interface

The control interface was implemented with commercial dSpace systems[4], consisting of a hardware and software. The software can be integrated into MATLAB and Simulink[5] allowing all the control codes to be designed in MATLAB. The dSpace provides Simulink blocks for the AD- and DA-converter ports. The blocks act like normal inputs and outputs in Simulink.

[4]http://www.dspace.ltd.uk/

[5]MATLAB and Simulink are trademarks of Mathworks Inc. (http://www.mathworks.com/)

That makes it possible to take the same controllers used in simulations and "paste" them into the actual control program.

The dSpace hardware part includes a processor that runs the control program, AD- and DA-converters and a frequency converter. The frequency converter was made by ABB, so it did not come with the dSpace system. The system used in the project had been used for another project before and the frequency converter had been made as a part of that system. The frequency converter was only briefly tested.

The control program was designed and built on a normal desktop computer. The Simulink program was compiled into c-code with MATLAB's realtime workshop and then loaded into the processor via Ethernet connection. The AD- and DA-converter ports were in a separate rack that was connected to the processor with a serial cable. The Ethernet connection between the processor and the desktop computer retrieved measurement data from the processor to the desktop computer, where the data could be analyzed. The connection also allowed IO-data to be sent to the processor.

The control program was managed with dSpace control desktop program. The program allowed all data in the program to be monitored in realtime and also to change some predefined parameters in the control code allowing for example the control to be switched on and off manually and some gains to be altered while the program was running. The control desktop allowed to record and save measurement data into MATLAB 'struct'-form. The data was then processed in MATLAB. The sampling time for system was set to 5 kHz but the measured data was down-sampled to 1 kHz.

5.2 Methods and techniques

5.2.1 Measurement techniques

The very first measurements with the test machine were done with DC-field. The machine was disconnected from the 3-phase power supply and DC-current was fed to one of the phases of the main 2-pole winding. The purpose of this measurement was to safely test the forces that could be produced with the actuator and to determine some of the physical angles between different windings.

When the current was increased rapidly, the 2-pole measurement showed the direction of the increasing magnetic field in its own coordination. Strong field pulled the rotor towards the stator frame at the direction of maximum flux density. Thus it was possible to determine the angle between displacement measurement and 2-pole field measurement; however, it was not pos-

sible tell had the rotor been pulled to the negative or positive side of the flux.

Next, the rotor shaft's deformation, the shape of the rotor, was measured by letting the rotor rundown freely without any field being present. The tacho meter was used to assign rotor angles to measured displacements. Displacement was then divided into full revolutions and the average was calculated angle wise. This gave a lookup table that gave the shape displacement as a function of rotor angle. The rundown data was taken from the last 30-40 full revolutions, so that the rotation speed was low and the eccentricity of the rotor did not awake mechanical forces. The measured shape was thus the track were no forces affect the rotor, except of course the gravity and supporting force from the bearings.

To be sure that the 4-pole extra winding could produce force and that the force could be controlled, the machine was first set to manual control. The control signal was a single rotating space vector of which frequency, amplitude and phase could be adjusted with the monitoring program. This test was first done at minimum rotation frequency, 8.3 Hz, but later done up to 32 Hz. The manual control was also used to control the vibrations to provide a reference to evaluate different controllers.

The manual control was also used to test the time periodic behavior of the machine. Because the single space vector, a wave shows up only as one spike in the frequency domain, there was some uncertainty about whether to spikes seen in the response were caused by the control or some other phenomenon. Thus became the idea of using several waves. Using a bunch of frequencies revealed the other phenomena as single spikes. Phases of the space vectors were randomized so that the maximum amplitude of their sum was as close to minimum as possible. This allowed bigger amplitudes to be used for individual waves, within the limits of the maximum control voltage (50 V). The amplitudes were manually controlled from the monitoring program.

The models for the machine were mostly identified from noise measurement data. Two different types of noise signals were used. The one that was used more was *band-limited white noise*, which was especially used in frequency domain identification. The used software, Simulink, provided easy way to produce this pseudo random signal. The frequency limit for identification was set to 200 Hz, but also 1 kHz and 40 Hz limits were used. It was discovered in the measurements that between 200 Hz and 220 Hz there was some mechanical dynamics that was not wanted to be included in the model. The other noise type was *uniform random number* also provided by Simulink. It was used only for time domain identification. The sampling frequency of the URN was lowered to 1 kHz with zero-order hold.

The system models were identified always for one operating point of the

machine. The controllers were first tested at the operating point they were designed. The controllers were switched on and off and the rotor was attempted to be controlled both to the shape path and to the measurement origin. The robustness of the controllers were tested by hitting the rotor shaft with a hammer and changing the operation point of the machine, i.e. adjusting the rotation speed and field strength.

As the rotation speed and field strength were increased, the rotor displacement was close to the limits of the sensors even without any kind of control input. The magnitude of the displacement depended greatly on the slip angle of the machine. This behavior was recorded for disturbance modeling and to be used to calculate the effect of the control input. Identification data was measured with various slip angles but some measurements were done only when disturbance was at its minimum phase. This allowed bigger amplitudes to be used without the measurements saturating[6] or rotor hitting the safety bearings. Before this was made into a common practice, it was made sure that the control did not depend on the slip angle.

5.2.2 Data processing

The control winding had three phases and thus the controller had three voltage outputs. The displacement was only measured in two directions and the forces were to be controlled only in 2D. Thus the 3-phase voltage was presented as a space vector inside the control program. The designed controllers only had two outputs, the two components of the space vector. The conversion to three phase voltage was made as part of the control interface on the software side. The coordination transformations were also included into the interface.

The models presented in Chapter 3 used different coordination systems. Especially the control voltage needed to be in rotating coordination to make the system less time variant. These transformations had to be calculated online and they were done by using the 2-pole field measurement. The exponent factor in the transformation 3.17 was obtained by representing the 2-pole field as a complex quantity and dividing it with its absolute value, extracting the phase information i.e. the measured field angle. The direction of the measuring coils was unknown in the coordination system defined for the displacement[7]. The field measurement signal needed to be smooth since the angle was used to modulate the controller output and also the measured displacement in those cases, when rotor coordinate system was used. The

[6]The range of the sensors used was limited. If the rotor shaft was too far, the senor gave maximum voltage signal.

[7]Some efforts were made to measure the angle, but ultimately there was no need for it.

same transformation was used for the currents and 4-pole field measurement, but these were not needed online.

The rotor displacement was measured from the rotor shaft outside the actual machine. Thus, the measured displacements were smaller than the actual displacement of the rotor core. The measurement was assumed to be directly proportional to the real displacement. The models and controllers required only the differential displacement of the rotor. Thus it was possible to remove any displacement caused by unwanted phenomena from the measurements without corrupting the models. These were the rotor shaft's deformation and the displacement caused by disturbance forces.

The mechanical displacement of the rotor was obtained by using the measured rotor angle and the lookup table for the shape to calculate the track where the rotor would have been, if no forces were exerted on it. This track was subtracted from the measured displacement. The controllers for the system were to be used to eliminate the forces from the rotor, i.e. set the mechanical displacement to zero. The lookup table was thought to be too heavy for online calculation, thus the shape displacement was presented as a sum of trigonometric functions of the rotor angle. The most significant sine and cosine components were used.

The disturbance forces, magnetic force caused by the shape of the rotor and mechanical force from eccentricity, were removed from measured data in a similar fashion as the direct effect of the shape. The tract where the rotor stayed when no control was applied was recorded and then subtracted from data measured with the control on. The remaining displacement told how the rotor orbit had changed. This method also removed the shape of the rotor. For each measured data, the last few seconds were taken without control so that the disturbance effect could be calculated from it. That worked as long as there was no slip.

The magnetic forces caused by the shape of the rotor are functions of the rotor angle and the slip angle[8]. Thus, the disturbance needs to be recorded as a function of both the angles. The period of the slip angle can be several minutes, thus, the disturbance has to be measured separately. The disturbance was measured for each operating point used. The few last seconds of each data was still measured without control so that it was possible to estimate the error of the removal.

[8]Angle between rotor and the main flux.

5.2.3 Model identification

Removing the disturbances reveals the real system dynamics. The processed measurement data only describes the effect of control voltage which allows standard identification tools to be used. For LTI systems, noise would be fed as a control signal and the input and output compared; however, the time periodic nature of the system model makes the identification more complicated. The effect of control consists of four components. The LTI-component, LTP-component and their elliptic counterparts. By switching coordination systems, two of these components can be included into a linear model. The elliptic LTP-component is the smallest and thus can be left out. But then either the LTP-component or the elliptic LTI-component must be neglected from the time invariant model as well.

Another problem, when using noise input for identification, is that the neglected components cannot be removed from the data. In frequency domain, the effect of the neglected component will overlap with the effect of modeled components. If the machine is controlled with a single rotating space vector, a wave, the response would be four waves. The two waves that are on the control frequency and on the negative control frequency, in the used coordination system, will only overlap with responses of the negative control wave on the same frequency. The other two waves, however, overlap with some other control frequency. With noise input, it is only possible to measure the sum effect of all the control waves. If the identification noise is randomized well enough, the overlapping parts should only give zero-averaged noise to the calculated responses, allowing this method still to be used.

Each of the four components in the models can be measured separately if, instead of using noise, the identification signal is constructed from single frequencies. It is possible to choose some number of frequencies or even a narrow frequency band that does not cause overlapping. If for example the control frequencies are chosen from 0 to the synchronous speed, the LTI-component will be at that band, the LTP-component will be between the synchronous speed and twice the synchronous speed, and their elliptics will be at the same frequencies but on the negative side, respectively. Thus, the effect of each component can be separated from the frequency response.

Keeping the control band between consecutive multiples of the synchronous speed, the frequencies will never overlap, and the "pure" frequency response can be measured. It just takes more measurements than the noise identification, because every band has to measured separately. If even narrower bands are used, bigger amplitudes can be used. This method was named *wave response measurement* because the control signals are waves or sum of waves traveling to specific direction. A normal frequency response measurement

does not include negative frequencies.

The four components can also be separated from noise input data with more experimental method. If each point of the wave response, obtained with noise measurement, is a sum of four components, measuring four sets of data gives four equations, from which the individual wave responses can be solved. If even more data is measured, the wave responses can be fitted with the method of least squares. This method was used to calculate only the three most significant components. Each point of the wave responses, i.e. each frequency f, was solved from (5.1) where n is the number of measurements, $\underline{Z}_c$ the displacement wave spectrum and $\underline{u}$ the control signal in time domain.

$$\begin{bmatrix} \underline{Z}_{c,1} \\ \underline{Z}_{c,2} \\ \vdots \\ \underline{Z}_{c,n} \end{bmatrix} = \begin{bmatrix} \mathfrak{F}\{\underline{u}_1\} & \mathfrak{F}\{\underline{u}_1^*\} & \mathfrak{F}\left\{\underline{u}_1^* e^{j2(\omega_s t+\varphi_s)}\right\} \\ \mathfrak{F}\{\underline{u}_2\} & \mathfrak{F}\{\underline{u}_2^*\} & \mathfrak{F}\left\{\underline{u}_2^* e^{j2(\omega_s t+\varphi_s)}\right\} \\ \vdots & \vdots & \vdots \\ \mathfrak{F}\{\underline{u}_n\} & \mathfrak{F}\{\underline{u}_n^*\} & \mathfrak{F}\left\{\underline{u}_n^* e^{j2(\omega_s t+\varphi_s)}\right\} \end{bmatrix} \begin{bmatrix} \mathbf{G}_{LTI} \\ \mathbf{G}_{el.LTI} \\ \mathbf{G}_{LTP} \end{bmatrix} \tag{5.1}$$

Once the response data were obtained, the model parameters were identified with various methods. The original idea was to use *differential evolution algorithm* (Price, Storn & Lampinen 2005) to find the physical parameters in the models in Chapter 3 (Ursem & Vadstrup 2003). Unfortunately, the algorithm gave nothing worth reporting despite various attempts. With the physical model it would have been possible to estimate the forces on the rotor allowing them to be controlled directly.

The back-up plan was to use black box identification methods to obtain state-space representations and then later try to solve physical parameters from the models. The LTI models were identified from the normal noise measurement with *PEM* (parameter estimation method) (Ljung 2006) and *subspace identification* (Katayama 2005). The models were built in frequency and time domain, in the k- and rotor coordination systems. PEM was also used for LTP models in frequency domain.

Some of the responses obtained with wave response measurements were so smooth that it was possible to find poles and zeros for the system by just handpicking them, based on the response figures. The failed differential evolution algorithm was used successfully to help to find the zeros once the poles were picked.

For the convergent control, it was not even necessary to obtain the full models. The CC only needed the gains and amplitudes at its operating frequency and those could be read from the calculated responses directly. The CC was so robust that it was possible to use data from which the disturbances had not been removed in time domain. At the early state of the project, the

frequency responses were calculated from raw data. The responses showed the constrained vibration spikes caused by the disturbance at the multiples of rotation speed. The spikes were removed in frequency domain and the CC model parameters interpolated from the remaining curves.

Chapter 6

Results

6.1 Disturbance measurements

The very first measurements with the test machine revealed that the rotor of the machine was not straight, but was somehow bowed. The displacement measurements gave a rough sine wave with 40 μm amplitude when the rotor was rotated slowly. This measured displacement was named *rotor shape*. The shape measured by the sensor in x-direction is showed in Figure 6.1.

The shapes were recorded with 0.5 degree spacing. The measurement in y-direction gave almost the same signal, only shifted in phase and inverted[1]. The phase shift between the measurements was 79 degrees, not 90 degrees as it should have been. The measurement in x-direction was placed too high by the measurement frame and because of the frame's rigid design, there was no easy way to fix the problem, see Figure 5.3. The phase shift was taken into account in data postprocessing.

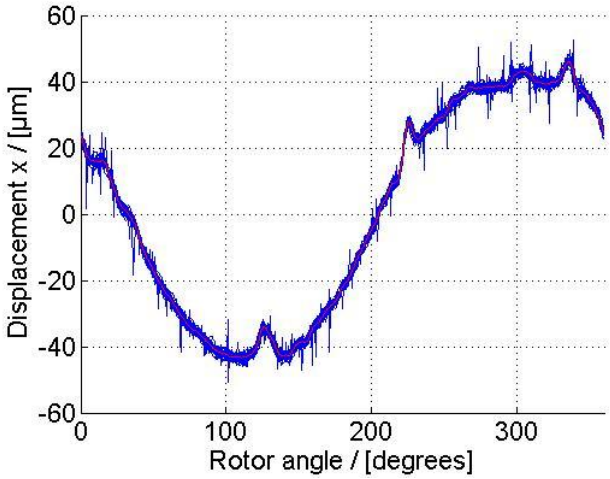

Figure 6.1: Shape of the rotor in horizontal direction (x-direction). The Shape was obtained by measuring the displacement during 37 full revolutions when the rotor was running down freely. The rotation speed of the rotor went from 2.5 Hz to zero. The displacement was presented as a function of the rotor angle and the shape calculated as an average of the rotations. Thus, systematic measurement errors were included into the rotor shape.

The rotor's mechanical displacement was obtained from the measurements by subtracting the shape from the measured signals. Off-line, the

[1]Measurement in x-direction was on the negative side of the x-axis and y-measurement on the positive side, thus the y-direction signal was inverted, see Figure 5.4.

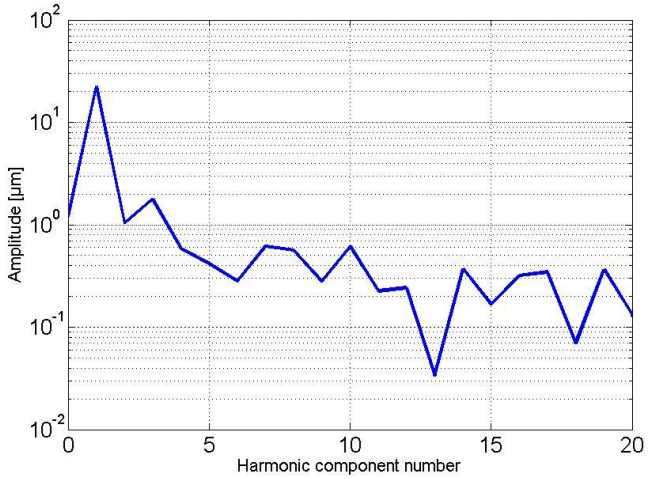

Figure 6.2: Spectrum of the rotor shape. Obtained by calculating the Fourier spectrum of the shape in x-direction.

shape displacement was interpolated from the recorded shapes by using the rotor angle information. This method was thought to be too heavy for online calculation. For online calculation, the shape was presented as a function of the rotor angle using sine functions. The spectrum of the rotor shape, provided in Figure 6.2, showed that the first three harmonics and the DC off-set are the most significant components. The other components are also outside the designed operating band of the controllers which serves as additional justification to ignore them.

The rotor displacement was measured from only one end off the rotor shaft. An extra displacement sensor was briefly tested on the other side to reveal conical rotor motion. The displacement sensor was positioned horizontally to measure x-direction. The rotor shape measured from this extra sensor was in almost 90 phase shift with the measurement on the other side. This would suggest that the rotor shaft was in some kind of spiral. The mechanical displacement, measured with the extra sensor, was consistent with the measurement on the other side when force was applied to the rotor with the actuator. Because the rotor shaft was deformed, having displacement measurements on both ends of the shaft, still would not have given the real displacement of the rotor core.

When the machine was rotated with a weak field[2], the rotor displacement followed the measured shape perfectly. When the flux density of the machine

[2]Field that was required to keep the machine running.

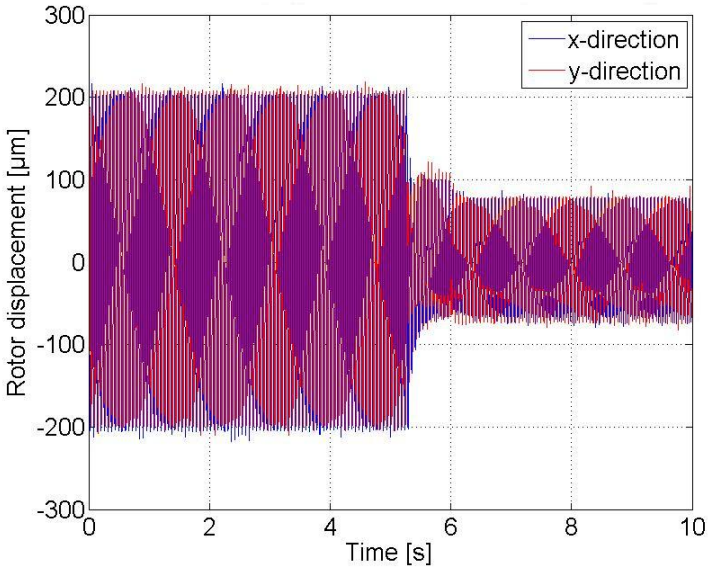

Figure 6.3: Passive damping of 4-pole winding. The machine is operating at 17 Hz 0.35 T. The 4-pole winding is short-circuited at 5.5 s. There was a small delay on one of the three phases that caused the transient visible before 6 s.

was increased, the eccentric rotor started to become a problem. At all the rotation speeds tested, the rotor hit the safety bearings before a sufficient field to produce force was reached. The forces caused by the unbalanced magnetic pull, UMP, were too strong for the thin and long rotor. The real eccentricity of the rotor was not accurately measured but, when the machine was opened and examined with feeding gauge, the eccentricity was estimated to be as high as 50%.

The problem with the eccentricity was partially solved, when the amplifiers connected to the control windings were switched on. Switching the amplifiers on short-circuited the 4-pole winding allowing currents to be induced. The short-circuited extra winding acts as a damper winding greatly reducing the magnetic forces on the rotor. (Chiba et al. 2006)

Figure 6.3 illustrates the effect on the measured rotor displacement. The machine was running at 17 Hz with 0.35 T flux density, when the 4-pole winding was short circuited. With this passive vibration control, the flux density could be increased to above 0.6 T. The 17 Hz rotation frequency with 0.6 T flux density was chosen as one of the operating points, at which the controllers were tested.

At the 17 Hz operating point, the machine was operating at synchronism. Comparing the angle of the rotor and the phase angle of the 2-pole main field showed that, when the flux density increased over some threshold, slip of the machine would disappear. The slip angle, the angle between the field and rotor, kept the value it had when the machine reached synchronous state. The slip angle received practically random values depending on the position of the rotor when the voltage was increased in the main winding.

From this observation, it was concluded that the machine developed some remanence field in the rotor core when rotating at low speed. The remanence causes what is known as hysteresis torque that keeps the machine in synchronism at no load. The machine did not lose its synchronism until the rotation speed was increased over 26 Hz and the torque from friction exceeded the hysteresis torque.

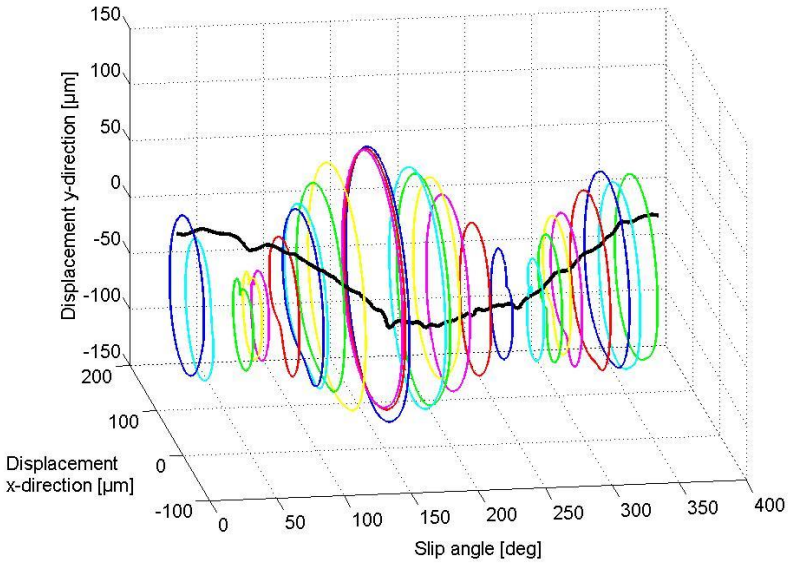

Figure 6.4: Rotor orbits with different slip angles at synchronous state. The shape has been removed from the orbits, thus they only illustrate the displacement caused by forces affecting the rotor. The orbits only have three first harmonic components and DC off-set. The higher components were removed. The line running through all the orbits is the shape of the rotor as a function of the rotor angle.

Because the machine was running without slip, the measured displacements were periodic; a function of the rotor angle only. The rotor was staying

on a constant path. However, this path depended greatly on the slip angle of the machine. Figure 6.4 shows results from measurements at different slip angles. The biggest displacement amplitudes were 2-3 times higher than the smallest one. The displacement amplitudes had two maximums per one cycle of slip angle.

It was concluded that the maximums occur when the 2-pole field is parallel with the rotor bow. That is when the shortest air gap would be in the direction of the maximum flux density if there were no forces on the rotor. The magnetic forces change the location of the shortest air gap but the effective spring force of the rotor shaft is weakest in the direction of the shape. This theory, however, was not confirmed.

When the rotation speed of the machine was increased to 30 Hz, a noticeable slip was detected. Also, it became clear that it was not possible to run the machine any faster while sustaining a sufficient flux without having some active controller on. The flux needed to be weakened even to stay at 30 Hz. The slip of the machine varied between measurements but was between 0.010-0.015 % . Thus the slip angle run a full circle in 4-6 minutes depending on the day. The effect of the slip angle on the magnetic disturbance forces remained which meant that the measured displacement amplitudes varied with a 4-6 minute period.

The rotor path was plotted in a 3D-figure with slip angle on the z-axis. The rotor path drew a tight spiral in which the amplitude of the displacement changes as a function of the slip angle. The spiral can be used to define a surface called here as orbital tube, shown in Figure 6.5. Although the measured rotor displacement was no longer periodic because of the slip, the displacement stayed on the surface of the orbital tube. Only the starting points of the spirals drifted as the rotor angle was different in the beginning of each slip angle period. The tube stayed constant during a measurement, but some changes where noticed between measurements. The small variations in rotation speed and main field flux density affected the tube.

It should be noted that Genta (1999) defined the term orbital tube as a function of changing rotation speed, not as a function of the slip. In this work, the rotation speeds were kept constant. Basically, both definitions have a time-dependent variable on the z-axis so the definition can be expanded to cover both cases.

The orbital tube is needed to reduce the effect of the disturbance forces from measurements. For modeling purposes, only the effect of the control voltage on the displacement is important. The disturbance can be interpolated from the tube when the rotor angle and slip angle are known. The disturbance is then subtracted from the measurements. Figure 6.7 shows an example of the removal. The accuracy of this method was tested by turning

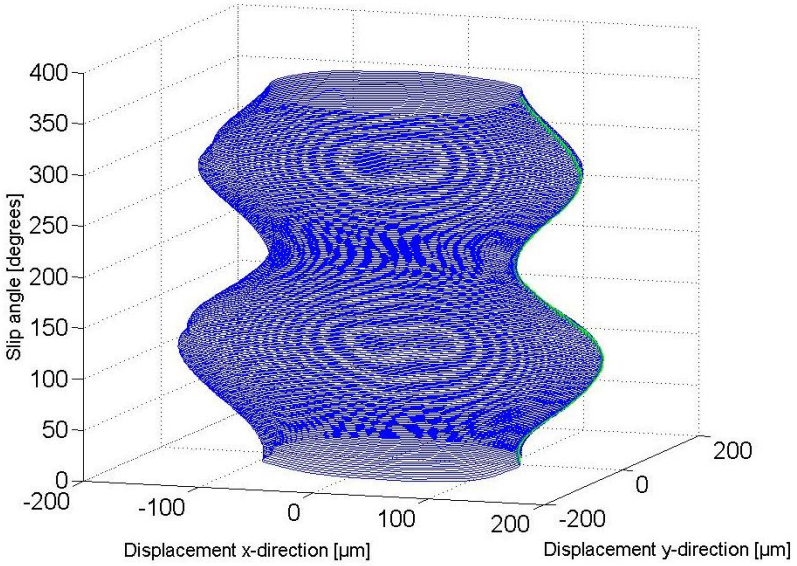

Figure 6.5: Orbital tube at 30 Hz. The orbital tube is the rotor's displacement as a function of rotor angle and slip angle. It took the rotor 5-6 minutes to spiral through the tube during which it made over 10000 full revolutions.

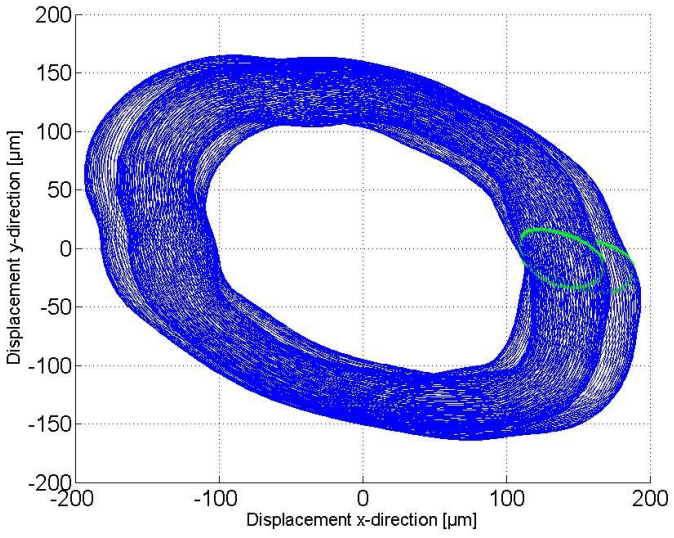

Figure 6.6: Orbital tube at 30 Hz from above. The orbits of the rotor are not circles or even ellipses. The faint green line on the right side of the tube marks the points on the track where rotor angle is zero.

the control voltage always to zero after sufficient data was recorded so that the last few seconds were recorded without control. The amplitude of the error was less than 5 μm. A similar method was also used for the extra winding currents.

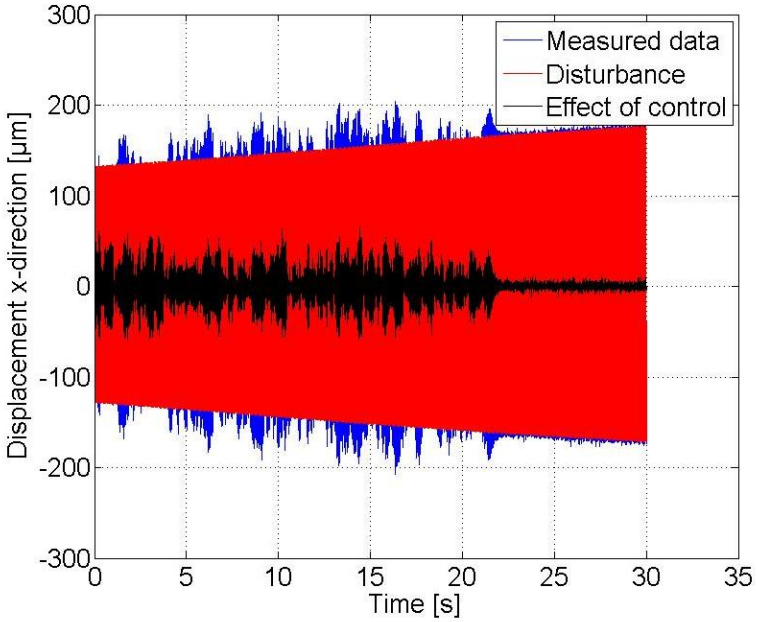

Figure 6.7: Calculating the effect of control for rotor displacement in x-direction. Band limited white noise is used as a control signal. The disturbance is interpolated from the orbital tube and subtracted from the measurement. The control signal is zero after 22 seconds. The last 8 seconds give the error of the method which is less than 5 μm. The rotation frequency was 30 Hz.

6.2 Model identification results

Modeling the test machine proved to be an extremely challenging task. A lot of hope was placed on the differential evolution algorithm to find the parameter model for the machine. The parameter model was never achieved but some models were obtained. The measurements also supported the model structure in the parameter model at least partially.

Figures 6.8-6.11 show a part of the wave response measurements done for the rotation speed 17 Hz with a 0.6 T main 2-pole flux density. The control voltage was a sum of 18 waves with 1 Hz intervals. The phases were randomized and the amplitudes can be seen from the figures. The same constant amplitude was used for each of the 18 waves but the amplitude was changed between measurements.

The first one of the four figures, Figure 6.8, shows the responses within the range from the negative rotation speed (-17 Hz) to 0 Hz. The control voltage was in k-coordination system so the actual output voltage going to the amplifiers was from DC to 17 Hz. The reason why this coordination was used can be seen from the figure. The biggest displacements are now at the same frequency as the control signal. Therefore, the main force component is at the control frequency.

Figure 6.8 also shows the time periodic behavior of the machine. An LTI system would have responses only at the control frequency and the other bands would be zero. From the extra winding current, at least 6 other frequency bands can be detected. The most important thing, though, is that the rotor displacement only shows 3 frequency bands. The LTI-component is the biggest.

The elliptic waves of the LTI-component are within the range from 0 to 17 Hz. They tell that the rotor displacement rotates against the rotation of the rotor on an elliptic path. The amplitude ratio of the forward and backward waves tells how elliptic the displacement path is. The bigger one defines the rotation direction and the phases (that have not been presented) define the direction of the main axis. The time periodic (LTP) component is within the range from 34 to 51 Hz. This frequency band is the elliptic band plus twice the supply frequency (34 Hz).[3] The elliptic for the LTP-component was not detected, so those components of the displacement rotated on circular paths.

Figure 6.9 displays the control frequency range 0 to 17 Hz. This is the most important range because most of the forces causing vibration are at the rotation speed. The amplitude of the time periodic component is approximately 25 % of the LTI component that is now within 17 to 34 Hz.

[3]The slip was zero as explained in 6.1.

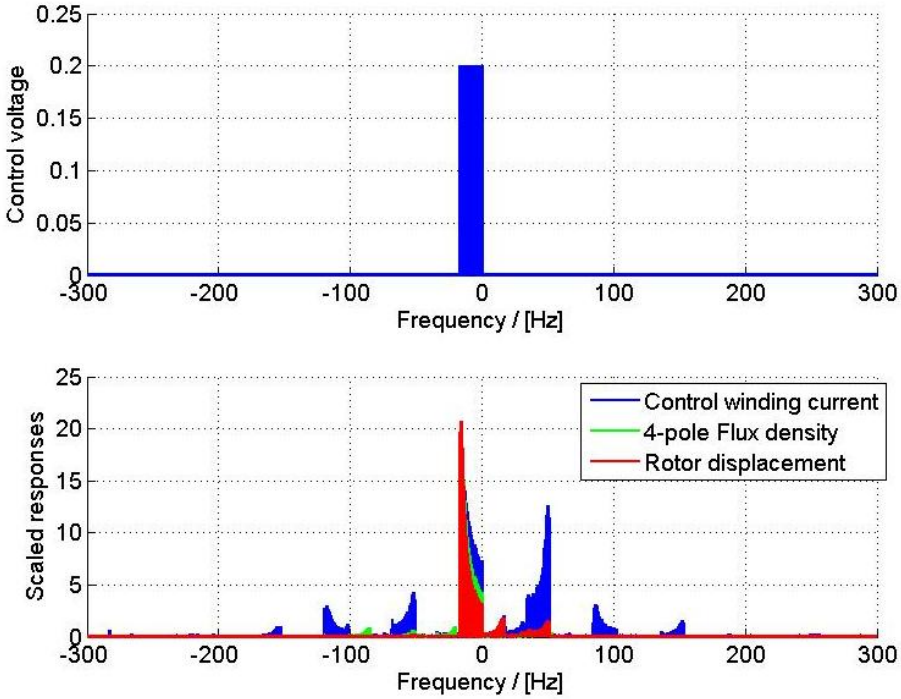

Figure 6.8: Wave response measurement from -17 to 0 Hz at rotation speed 17 Hz. The control signal is above and measured responses below. The control voltage is in k-coordination system. The responses show only the effect of the control. The disturbance has been removed. The response shows a sharp resonance at -17 Hz. That is the frequency at which the actual output voltage of the controller is a DC voltage. Because of the strong response, the control amplitude was lower than for the other frequency bands. The control signal consists of 18 frequencies with 1 Hz intervals.

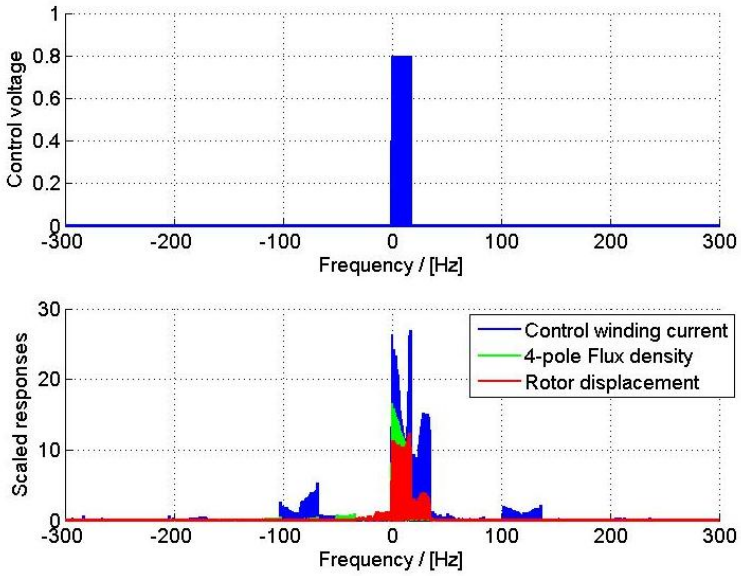

Figure 6.9: Wave response measurement from 0 to 17 Hz at rotation speed 17 Hz. The LTP component is very visible from 17 to 34 Hz. Both the elliptics can also be seen at the negative side.

The frequencies of the LTP components can thought to be the frequencies of the LTI components mirrored around supply frequency. The elliptics are mirrored around 0 Hz. Figure 6.9 shows the elliptics also for the LTP component.

In Figure 6.10, the control frequency is higher than the rotation speed. The non zero frequency bands for rotor displacement are the same as in Figure 6.9. The control voltage is just feeding the other band. The elliptics are getting smaller and in Figure 6.11 they nearly disappear. At 51 Hz the LTP components hits the -17 Hz DC resonance.

The single wave response figures themselves do not help to get any closer the models for the machine, but they do confirm that the models derived in Chapter 3 describe the time periodic behavior correctly. To get useful data for model identification, the wave response figures need to be combined. Knowing the frequency bands in which each component is found in each figure, a full wave response for each component can be collected from different measurements. Taking only the values of the peeks and connecting them, gives Figures 6.12-6.15.

Figure 6.12 shows the wave response for the LTI component of the rotor displacement. This corresponds to the term $\mathbf{\Phi}\underline{\eta}_0$ in Section 3.4. Two sets

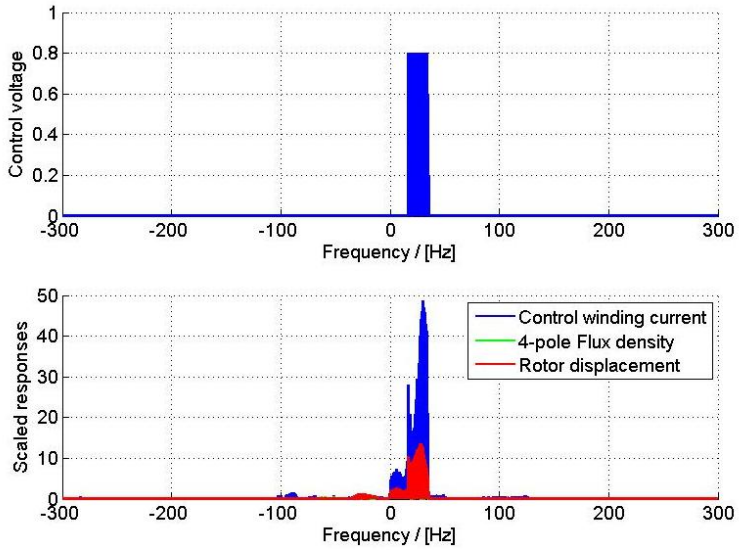

Figure 6.10: Wave response measurement from 17 to 34 Hz at rotation speed 17 Hz. The biggest radial forces rotate faster than the rotor.

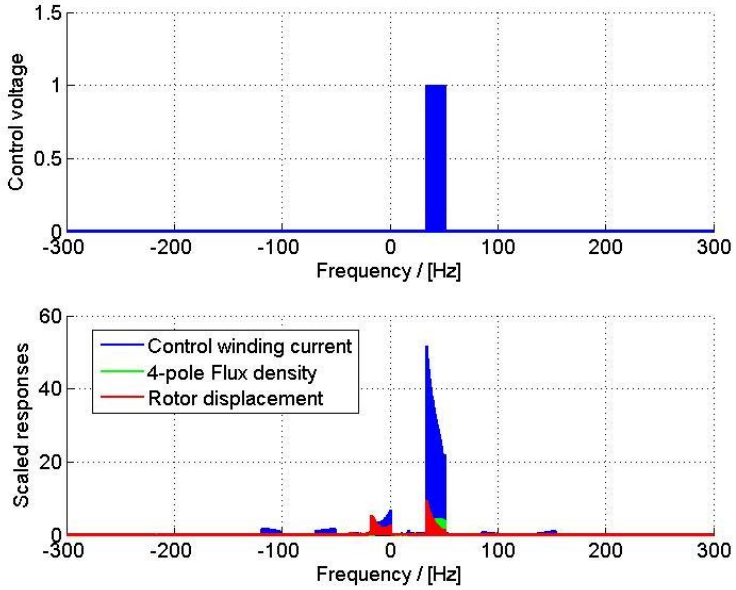

Figure 6.11: Wave response measurement from 34 to 51 Hz.

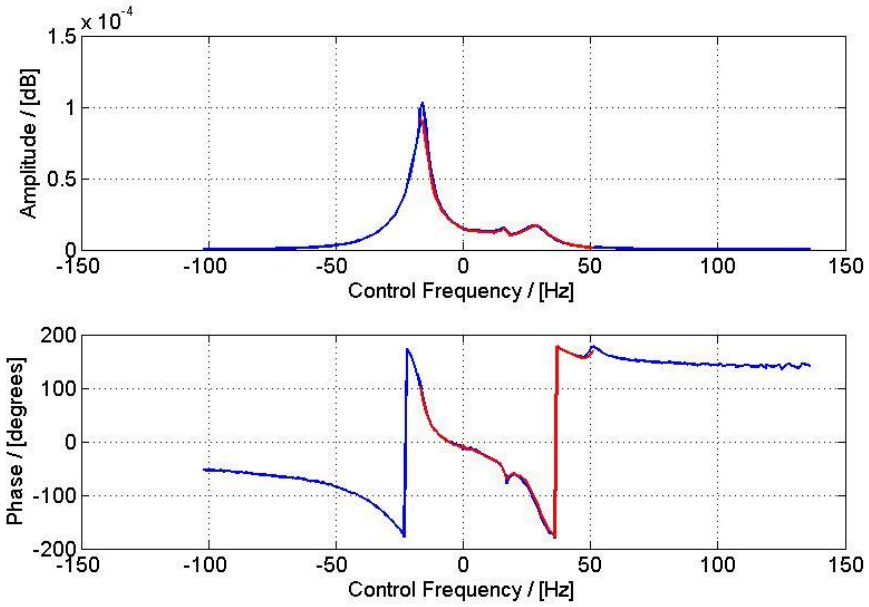

Figure 6.12: Wave response for the rotor displacement LTI-component at rotation speed 17 Hz, 0.6 T

of measurement were done on different days and both result are shown in the same figure. The curves look incredibly smooth and the only significant difference between the two measurements is at the top of the -17 Hz peek. There are two other visible spikes. At +17 Hz, there is an electromagnetic resonance related to the extra winding. Around +33 Hz is the mechanical resonance.

The mechanical bending frequency seemed to be surprisingly low. The electromagnetic feedback and the passive damping of the extra winding bring the frequency down from the 37.5 Hz where it was without the field being present. Still, the mechanical frequency was expected to drop only to 36 Hz. On the negative side, the mechanical frequency is lost under the DC resonance spike at -17 Hz.

The wave response for the LTP component of the rotor displacement, in Figure 6.13, is not as impressive as for the LTI component. The LTP components would be the term $\mathbf{\Phi}\underline{\eta}_2$ in the equations in Section 3.4. The response has been plotted as a function of the control frequency, not the output frequency. The output frequencies would be mirrored around 17 Hz. Again, the figure shows data from two different days. The amplitude curve seems decent but there is something wrong with the phase. There seems to be

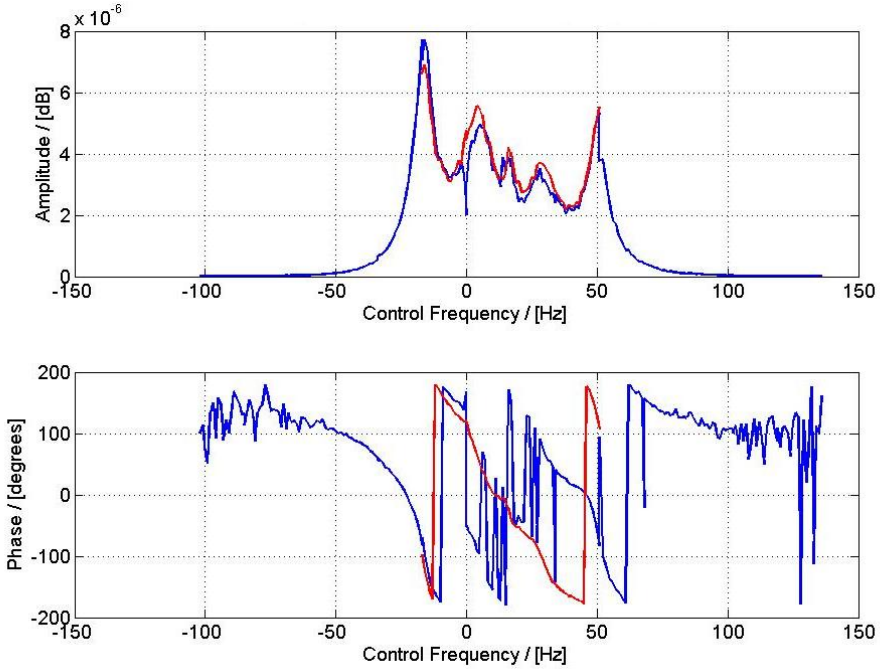

Figure 6.13: Wave response for the rotor displacement LTP-component at rotation speed 17 Hz, 0.6 T

an unexplained 180 degree discontinuance between the two ends of the phase curve. On the first measurement (the smaller data), the phase was smooth but the end does not match with the later measurements. It was thought, that by using bigger amplitudes, this problem would solve itself. However, there was no time to perform and process those measurements again during the time frame of this work.

Studying only the amplitude curve of the Figure 6.13, the locations of the five clear spikes is easy to explain. Starting from the right, at +51 Hz is the DC resonance for the LTP component. All the frequencies are mirrored around +17 Hz, the rotation speed, for the LTP. The next spike or mound is at +33 Hz. It has to come from the term or terms combining the LTI and LTP equations since it is clearly the mechanical frequency of the LTI component. The third hill is the rotation speed +17 Hz; it does not change for the LTP component. The second from left is near DC but on the positive side. It is assumed to be the mirrored mechanical frequency, again few Hertz off from where expected. The first one on the left and the biggest of the spikes would again be the coupling factor between LTI and LTP components.

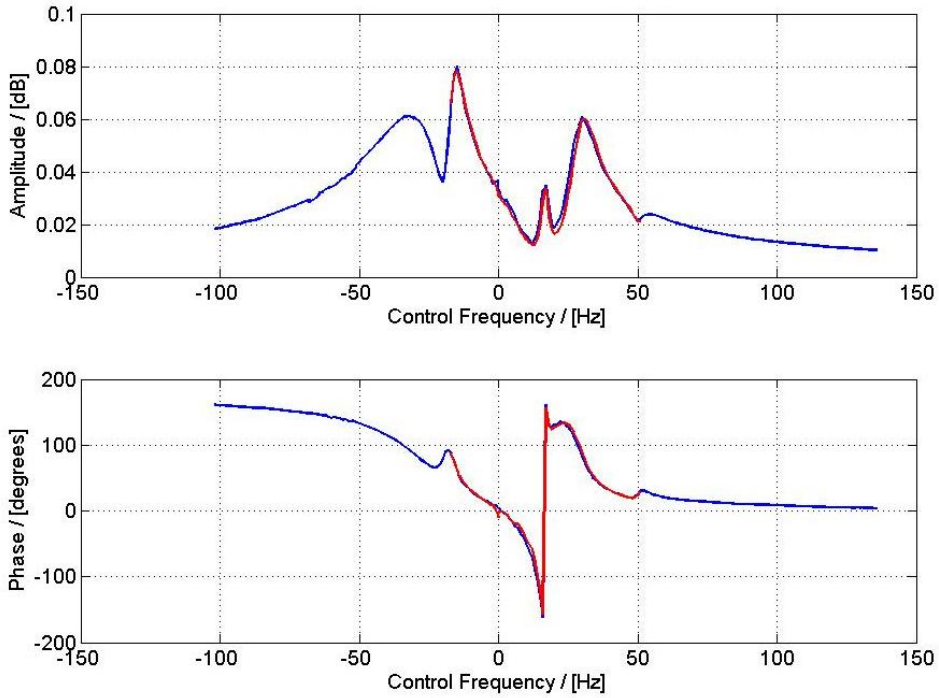

Figure 6.14: Wave response for the extra winding current LTI-component at rotation speed 17 Hz, 0.6 T

The elliptic responses were not computed because the data was to be used for symmetric model that did not have elliptics. The responses were computed for the extra winding currents, $\hat{\underline{i}}_{c,0}$ and $\hat{\underline{i}}_{c,2}$ in Section 3.4, as an effort to obtain the parameter model. Like for the displacement, the LTI component of the current was smooth, seen in Figure 6.14, and the two different measurements align almost perfectly. The LTP component of the current, in Figure 6.15, had the same problem as the displacement. Something was wrong with the phase.

The problems with the phases caused problems when identifying models from the wave responses, especially when there was no certainty, how the phase should look like; is the phase continuous from left or right, is there a 180 degree phase shift and if there is, where. The amplitude curves were thought to be valid and those were used for identification. Unfortunately, ignoring the phases ruled out any standard identification methods.

The responses for the LTI components in Figures 6.12 and 6.14 were so clear that it was possible to read the pole places from the figures with some accuracy. The model in 3.4 suggested that the system had 8 poles

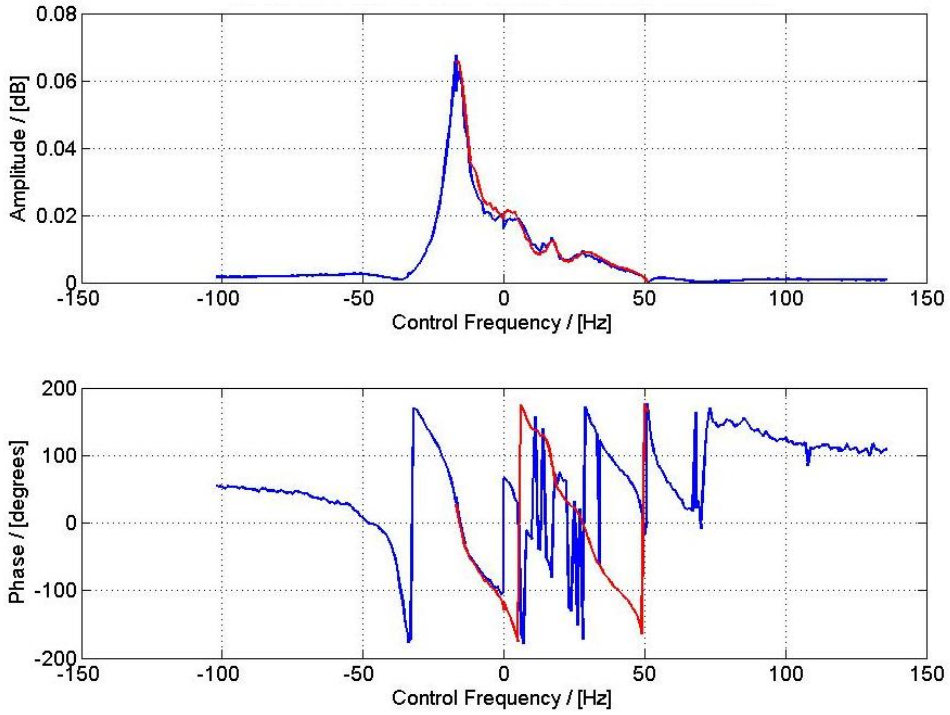

Figure 6.15: Wave response for the extra winding current LTP-component at rotation speed 17 Hz, 0.6 T

and those should be within ±100 Hz. The number of zeros could be seen from the total phase shift. The phase shift was 540 degrees indicating that there was 3 zeros less than poles[4]. For the current, 3 zeros could not get the edges of the phase curve decent at correct angle. Adding one positive and one negative zero allowed both the amplitude and phase to be matched perfectly. The fit obtained by placing the poles and zeros by hand was quite impressive. Figure 6.16 shows the measured and modeled responses for the two displacement components.

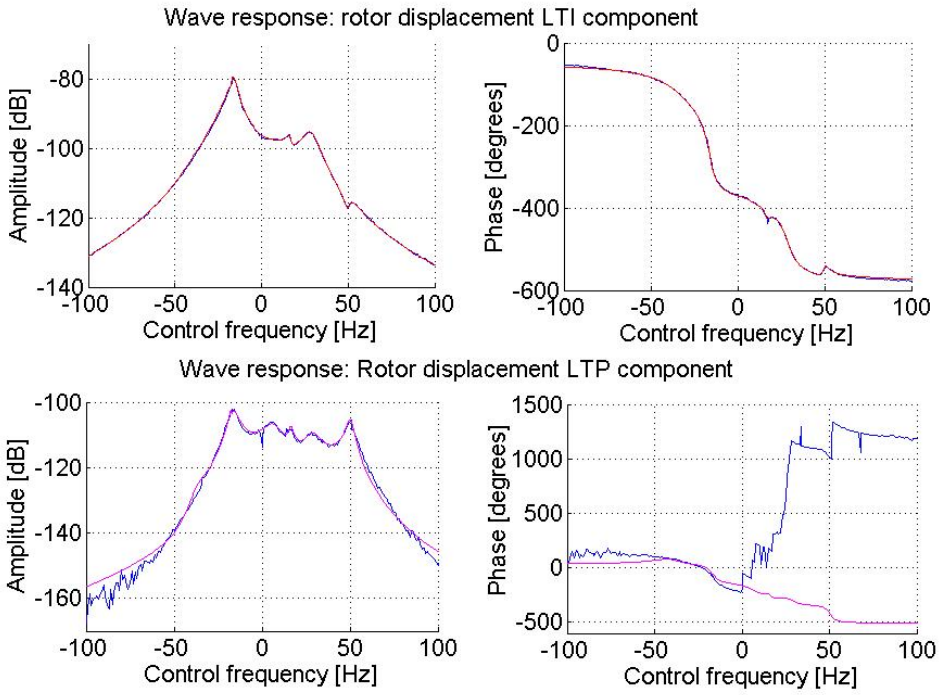

Figure 6.16: Measured and modeled wave responses for the two rotor displacement components. The model was done by picking the poles and zeros manually by trial and error. A trained eye can see the locations approximately from the figure making the method more reasonable. For the LTP component, the phase was ignored. Unit for the amplitude was m/V.

Once the satisfying pole positions were found by iterating the locations of poles and zeros, the zeros for each component were optimized with the differential evolution. Optimizing the poles was also tried but the cost function became too complicated and the iteration did not converge. It was possible

[4]Complex poles decrease and zeros increase phase 180 °, not 90 ° as for real systems.

to pick poles that gave good responses for two components, but not for all the four. Depending on which components were used for the optimization, the poles shifted few Hz. Some poles shifted more than the others.

The pole shifting was also detected when using PEM. The LTI components were so smooth that PEM could be used for them separately and together. There was one pole that seemed to have 2 "good" locations. One near +8 Hz and the other near +26 Hz. Figure 6.17 shows the fit when optimization was done for the current and displacement. The PEM gave 7 zeros for the current, one of them positive, and also 7 zeros for the displacement. Two of the zeros for displacement were at 200 Hz or higher so they were dropped out being outside the modeled frequency band. They were considered to be calculation errors or caused by the known dynamics at 200 Hz.

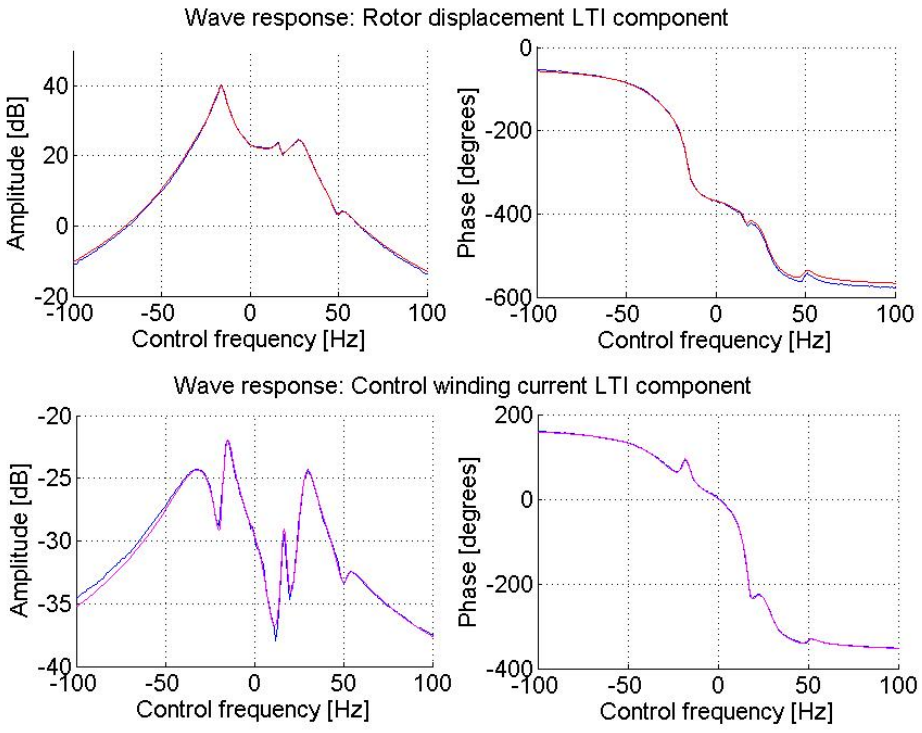

Figure 6.17: Measured and modeled wave responses for the LTI components of rotor displacement and extra winding current. The model was obtained with PEM in frequency domain. Unit for the amplitude was μm/V unlike in Figure 6.16.

When comparing the number of zeros predicted by the model with what was needed to get good data fit, one important observation was done. It was not mentioned in Section 3.4, but equations (3.39)-(3.44) predict 5 zeros for LTI displacement, 7 for LTI current, 4 for LTP displacement and 6 for LTP current. Yet, the measurement data very clearly indicated that the LTP components must have the same number of zeros as the LTI components. Even by adding more coupling terms into the equations, they still do not predict more than 6 zeros for the LTP current. The model will predict 7 zeros if the control voltage is added to equation (3.40). The idea that the control voltage exists also in the LTP equations seems reasonable, but the control voltage should have some time periodic factor in that equation. That would make the models a lot more complicated.

Despite the problems with the parametric model, the wave response method seems to have potential. For input-output identification, the method is valid. If all the phases would have been usable, the PEM could have been used to compute the combined model for all the components. The amplitudes of the control signal could have still been higher and maybe that would have fixed the phase.

Besides the wave response measurements, there was another identification method for LTP system presented in Section 5.2.3. Figure 6.18 shows the result from 30 noise measurements. The measurements were conducted at 30 Hz rotation speed with the 2-pole flux density being 0.38 T. The responses were calculated for three components of the rotor displacement (LTI, elliptic LTI, LTP) but not for the current.

From -50 Hz to +50 Hz the LTI component looks very smooth. The two peeks are at -30 Hz and at +35 Hz. There is something small also at +30 Hz. The 35 Hz is assumed to be the critical speed. The flux has been weakened so the passive damping is not as effective as at rotation speed 17 Hz. Even though the data has been filtered, the elliptic LTI and the LTP component are too noisy to be used with PEM, but clearly the dynamics can be seen from the figures. Maybe with more data and better filtering this method could be used to compute the parameters for the time periodic model.

Since the identification of the parameter models and time periodic models was unsuccessful, the machine was modeled as a black box[5] LTI system. The identifications were done in two coordinate systems. In k-coordinates and in field coordinates. The k-coordination does not include the time periodic components where as the field coordination does not have the elliptic components included in the model. The models were identified as real systems. The complex control voltage was broken into two real inputs. The measurements

[5]Black box means that only inputs and outputs are studied.

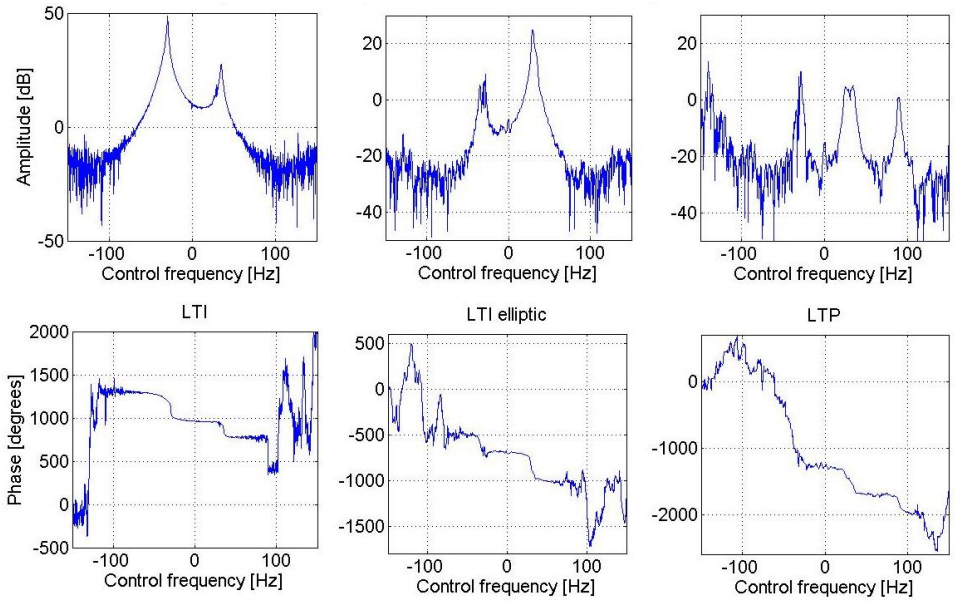

Figure 6.18: Wave responses from noise measurements. Thirty 20 second measurements were done using band-limited white noise (limit 200 Hz). The disturbance effect was removed from data and the responses fitted to 5.1. The least squares method was used for optimization. The measurements were done at 30 Hz 0.38 T

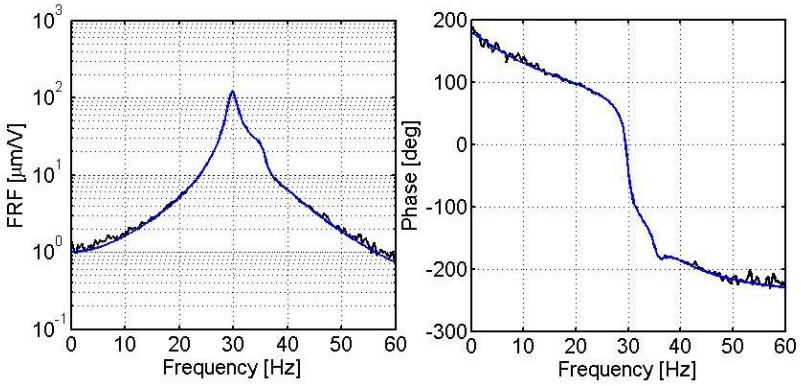

Figure 6.19: Frequency response from the real part of the control voltage to x-direction displacement. The control voltage is in k-coordination. The response was measured by feeding band-limited white noise only to the first control voltage input. The smooth line (blue) is the fitted model that had 8 states. The model was fitted with PEM in frequency domain. The model had two inputs and outputs. The identification was done at 30 Hz, 0.38 T

in x- and y-direction were treated as separate outputs.

The models were fitted with PEM in frequency domain. Figure 6.19 shows the frequency response from the first control input to x-direction measurement. The models were fitted using 6, 8, and 10 states. The 10 state models gave better fits but not every time, and they had a tendency to have uncontrollable states. The 8 state models did not have uncontrollable or unobservable states. The 6 state models were taught to have no rotor currents included in the model. For the controllers, the 8 state models were used.

Figure 6.20 is basically the same as 6.19 but both the control voltage and the displacement are in field coordinates. The response was measured specifically in field coordinates and not just calculated from the k-coordination measurement. Because the data was measured using band-limited input noise, the coordination transformation changes the frequency content of the input by shifting the limits. Figures 6.19 and 6.20 only show one of the 4 responses of the 2 by 2 system.

When comparing the frequency domain fits of the model, the k-coordination fit in Figure 6.19 is clearly better than with the model in rotor coordinates. In Figure 6.20, the model and the measurement differ significantly after 65 Hz. The k-coordination model is better also in time domain comparison. The models were compared against a different set of data that had been measured by feeding noise to both the control inputs. The k-coordination model gave

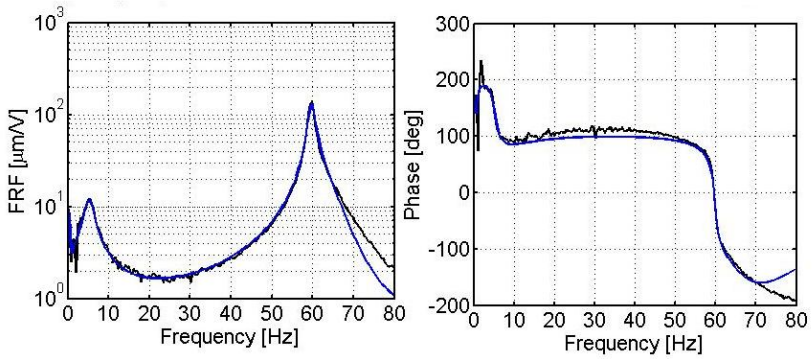

Figure 6.20: Frequency response from the real part of the control voltage to x-direction displacement. Both were calculated in field coordinates. The method was the same as in Figure 6.19. In the field coordination, the wave response would be shifted 30 Hz (rotation speed) towards left, thus the spikes in the frequency response are at different frequencies than in Figure 6.19. The 60 Hz spike in the FRF is actually the DC resonance at negative rotation speed, seen in the wave response figures.

about an 84% fit, shown in Figure 6.21, and the rotor coordination model gave about a 77% fit.

The model in the figures were identified at 30 Hz rotation speed (0.38 T). When the same measurement were done for 17 Hz (0.6 T), the rotor coordinate model was clearly better. The reason can be seen from the wave responses for example in Figures 6.9 and 6.18. At 17 Hz rotation speed, the LTP component is more significant than the elliptic. For 30 Hz, the elliptic has higher amplitudes but the LTP component is bigger at some frequencies.

One challenge for the control design was that changing the operation point had a huge effect on the models. The effect of the 2-pole flux density has been illustrated on Figure 6.22. It shows the response as in Figure 6.19 measured at different flux densities. Figure 6.22 also demonstrates how the mechanical resonance is damped by the magnetic feedback and almost disappears. The resonance moves to the extra winding currents. The frequency response of currents would show the 36 Hz frequency rising.

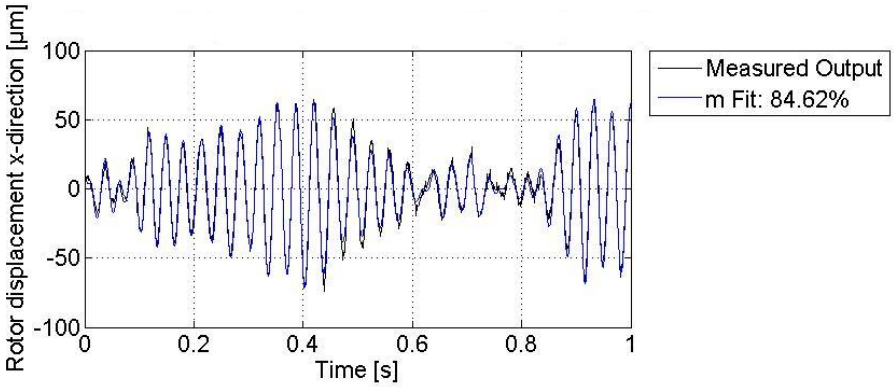

Figure 6.21: Time domain fit of k-coordination model. The model was identified in frequency domain. The compare data was measured feeding noise to both the control voltage components (x and y) and measuring the output. The disturbances were reduced from data. The model gave an 84.6% fit to x-direction displacement and an 83.7% fit to y-direction (not shown in figure).

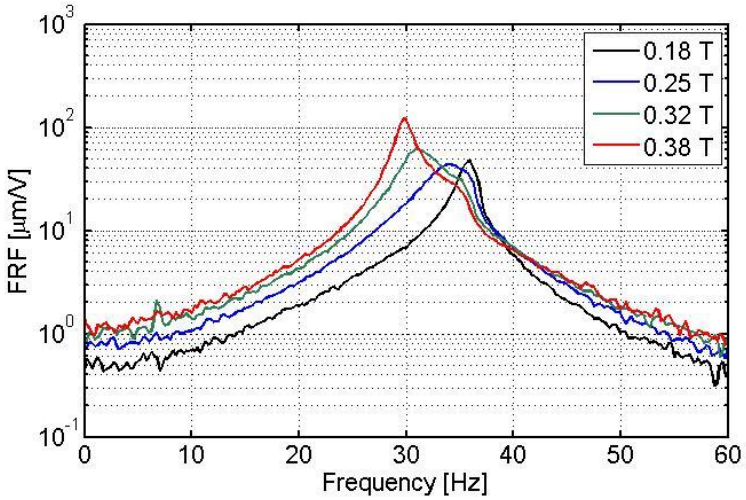

Figure 6.22: Frequency response from the k-coordination real part of control voltage to x-direction displacement. The mechanical resonance gets damped and the magnetic resonance increases as the 2-pole flux density is increased. The rotation frequency was 30 Hz.

6.3 Control results

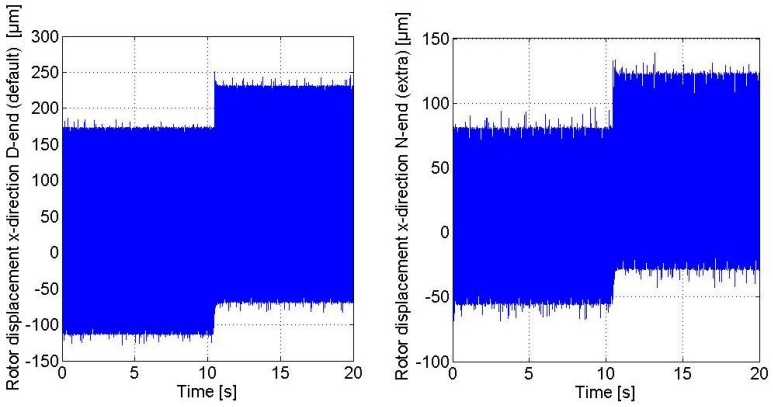

Figure 6.23: Producing static force to x-direction. The machine is rotating at 17 Hz (0.6 T). The control voltage is 3 V real (x-direction) DC in k-coordination. The control voltage is zero for the first 11 seconds. The two measurements are from the opposite sides of the machine. They show that the whole rotor is moving to the same direction; there is no twisting or conical motion from the control.

The first control objective was to prove that the extra winding can produce force and that the direction of the force can be controlled. When the control voltage was presented in k-coordination system, defined by 3.17, a DC voltage made the rotor move to a certain direction. If the real part of the control voltage was defined as being in x-direction and imaginary part as being in y-direction, the DC component of the force had a constant 88 degree phase shift compared to the control. The angle shift was caused by the physical angles between the different windings in the stator slots.

Figure 6.23 shows the displacement when force is produced in x-direction. The figure shows measurements from both sides of the machine. For most of the measurements, the displacement was only measured from the drive end side (D-end). The measurement in the other end revealed that the rotor shaft was in some kind of spiral. The phase shift between the two x-direction measurements was almost 90 degrees when the rotor was rotated without any magnetic field present. The effect of the control voltage was the same for both the measurements so the measurement on the other side was not necessary.

It was difficult to estimate the magnitude of the force that could be produced with the extra winding. In principle, the force could be calculated

from 3.11, if the flux densities are measured. The 2- and 4-pole fluxes were measured and efforts were made to measure the unipolar flux as well. Yet, no unipolar flux was detected. The unipolar flux should be small and is often neglected[6].

When the force was calculated from the 2- and 4-pole measurements alone, the calculations did not add up with the measured displacement. If there was no unipolar flux, there should have not been any time periodic behavior. One explanation is that time periodic behavior is caused by slot and saturation harmonics. Those were not included into the models but do contribute to the force (Arkkio & Holopainen 2008).

During measurements, the magnitude of force was never a problem. Even with weak fields the extra winding produced enough force to completely control the rotor. A normal machine would have at least twice the 2-pole flux density achieved in the measurement and the 2-pole flux density should be directly proportional to the force magnitude. The control voltages needed by the controllers were less than 25 V leaving another 25 V in reserve. Thus, even if the force could be calculated, it is difficult to measure the maximum force the actuator can produce, because the actuator can produce several times more force than needed.

The force production was tested by manually controlling the machine. The control voltage was built from one space vector and the amplitude, phase, and frequency were adjusted from the control desktop. The manual control was also used to control the vibrations. In k-coordination, when the control frequency was taken from the tachometer, the rotor path could be reduced by finding the correct phase. The rotor paths have been plotted to Figure 6.24.

Figure 6.25 shows the results from convergent control. After the start transient, the CC is very effective in removing the unwanted vibration. CC can control the rotor to almost any orbit. The wanted orbit is simply subtracted from the measured signals and the error signal is fed to the controller. In Figure 6.25, the controller tries to guide the rotor to the calculated shape orbit. The error from the shape orbit would be the mechanical displacement defined in Section 3.3. The CC results are only shown for 30 Hz rotation speed but the results were just as good for the 17 Hz.

The controller parameters α in Equation (4.18) were adjusted online from the monitoring program for each harmonic component of the controller. The parameter γ was set to be one. For the first harmonic α was from $1.5 \cdot 10^{-4}$ to $2.5 \cdot 10^{-4}$. For the other components, if included, α was about half of the value for first component. Adjusting the parameters affected the speed the

[6]Mainly because it is difficult to model.

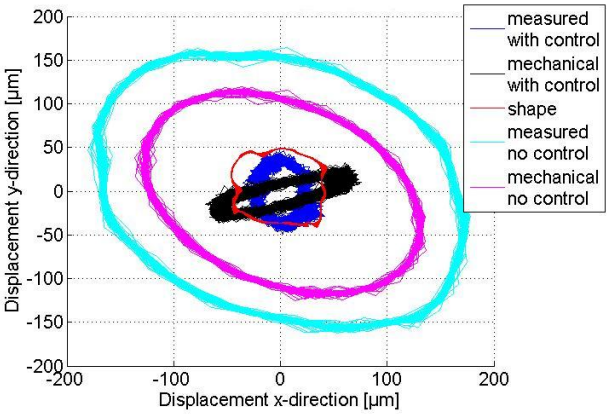

Figure 6.24: Manual control without feedback. The two outer rings are without control. The smaller one is the mechanical displacement. The thin line (red) is the rotor shape calculated from the rotor angle. The more circular one of the controlled paths is the measured and the more oblong the mechanical. Measurements were conducted at 30 Hz rotation speed.

vibration converged but did not change the steady state value.

Like already mentioned, when the rotor shape was measured from both ends of the shaft, there was a 90 degree phase shift between the two ends of the shaft. Both the ends reacted to the control in the same way. Forcing the measurement from one end to go to zero, would have increased the vibrations on the other end. Thus, the rotor was controlled to the shape orbit. Figure 6.25(b) reveals that the error from the shape orbit is very small.

One interesting feature of the machine was that the extra winding currents got smaller when controlled, Figure 6.26. When no control is applied, the extra winding is short-circuited. Currents flow in the windings and cause the passive damping effect seen in Figure 6.3. Applying control reduces the currents and corrects their phase. The currents consist mainly of two frequencies, the supply frequency (30 Hz) and twice the supply frequency (60 Hz). The currents were reduced also at other rotation frequencies.

Efficiency is one key issue about electric machines. The power consumption of the control was calculated from the known control voltages and measured extra winding currents. The actual output voltage of the control amplifiers was measured to be within 1 V of the calculated voltage when the test machine was set up. The power, when the controller was switched on, has been presented in Figure 6.27. It has to be mentioned that the required power in the figure is one of the lowest measured. The average active power

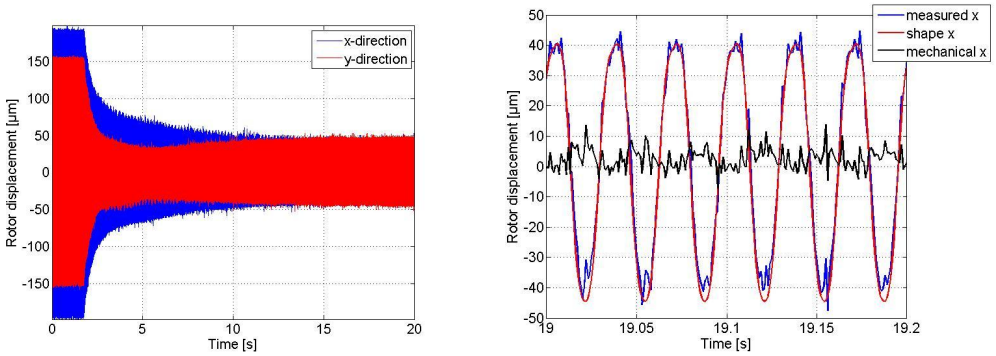

(a) Convergent control switched on

(b) Close-up x-direction only

Figure 6.25: Convergent control in field coordination at 30 Hz rotation frequency (0.38 T). The controller had two components, one at negative slip frequency and the other at 60 Hz. There was an over 10 second transient when the controller was switched on. The controller is not trying to set displacements to zero but to the shape orbit. Figure (a) shows the x- and y-direction measurements at start-up. Figure (b) shows that the difference between the measured displacement and the shape orbit in x-direction is about 10 µm at most. The inaccuracy when removing the effect of disturbance from the identification data was about 5 µm, see Figure 6.7.

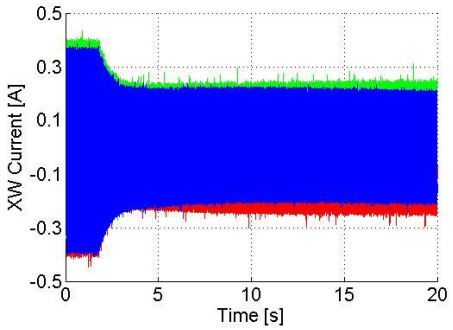

Figure 6.26: The currents of the extra winding reduce when the convergent control is switched on at 30 Hz rotation speed. Figure shows all three phases. The control voltage varied between 16 and 21.5 V depending on the slip angle. The currents had clearly two frequencies 30 Hz and 60 Hz with and without the control.

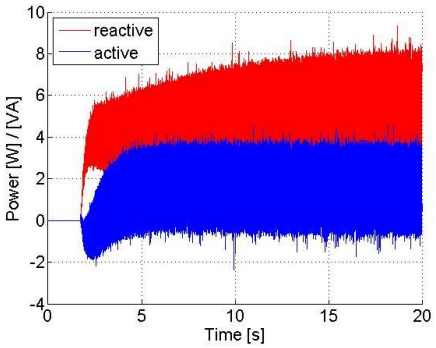

Figure 6.27: The power supplied to the extra winding when the machine is controlled with convergent control at 30 Hz rotation speed. The power was calculated using the measured currents and calculated voltages.

was only 1.2 W and the reactive 4 VA. During steady state measurements, the average control power varied between 1.6 W and 2.5 W, and it also depended on the slip angle.

Though the control requires some power, guiding the rotor to the shape orbit actually improves machine's efficiency. The supply power was measured with power analyzer, both controller on and off, and with various slip angles. When no control was applied, the average power varied from 156 W to 163 W. The power had only one maximum as a function of the slip angle.

With the control on, the average power was more constant varying from 152 W to 155 W. There was no clear maximum at any angle. With every slip angle, the total power consumption was reduced by the controller. At some angles, especially at the power maximum, the power was reduced more than on other angles. The powers were low because the machine was not loaded.

The stability of the controller was tested by hitting the rotor shaft with a hammer. Figure 6.28 shows the displacement in x-direction. The CC is slow to response to the hits but the vibration converges back to zero when looking at the mechanical displacement. For Figure 6.28, the control is done in k-coordinates with the k-coordination model obtained from the frequency response in Figure 6.19. The controller had only one component, the one at

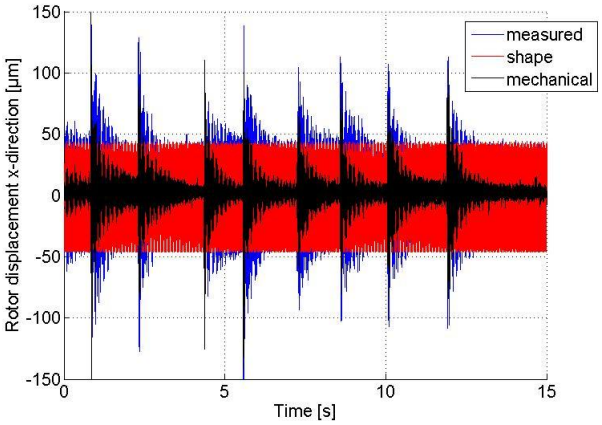

Figure 6.28: Rotor is guided to the shape orbit with convergent control. The rotation speed is 30 Hz and the controller was built on the k-coordination model. The rotor is hit several times with a large plastic hammer. The measured signal is left behind the calculated shape in the figure but the mechanical displacement (black) shows how the rotor orbit changes.

rotation speed, 30 Hz.

In the k-coordination, it was possible to control the rotor with just one control frequency. The CC was controlling the LTI component and the elliptic, but the LTP components, caused by the control voltage, were not controlled. In the field coordination, having only one frequency in the controller caused the rotor to go on an elliptic path shown in Figure 6.29. The control results are poor because the controller is not controlling the wave at negative rotation speed, and that component is excited by the control voltage. From the fact that the k-coordination CC worked well with only one frequency, it can be concluded that the elliptic LTI component dominates the LTP component at 30 Hz. This was confirmed with wave response measurements.

Adding another frequency to the CC in field coordination to remove the elliptic component removes the remaining vibration. The interesting thing is that the controller interprets the elliptic component as disturbance even though it is actually caused by a modeling error or the fact that the field coordination model does not include the elliptic component. This implicates that the CC is capable of controlling time periodic systems perfectly with time invariant models. Figure 6.30 shows a comparison between the one component k-coordination controller and two component field coordination controller.

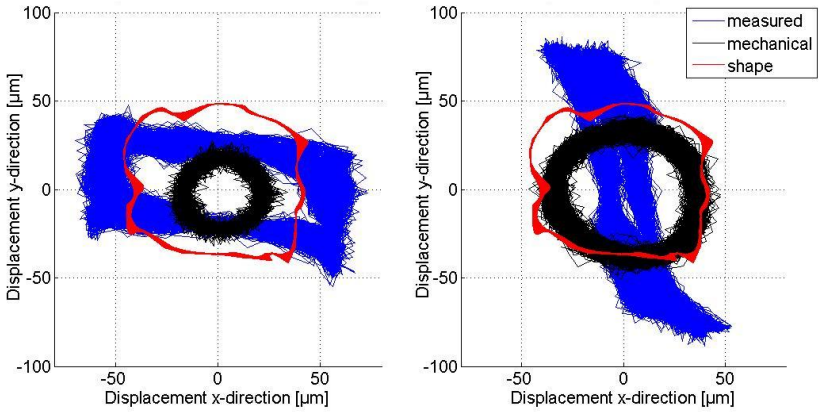

Figure 6.29: Steady state orbits when the rotor is controlled with convergent control on single frequency in field coordinates. The measured displacement was oblong and rotated clockwise at the slip frequency. The mechanical displacement was round but the radius of the orbit varied with the slip angle. The tracks are shown at two time incidents.

In steady state, the controllers were equally good but the k-coordination CC had very violent overshoot when turned on, see Figure 6.31. The reason for the over shoot remained a mystery. Considering this, the field coordination CC was better even if it required two components to operate.

The LQ controller had to be designed for k-coordination. The **Q** matrices in Equations (4.3) and (4.12) were chosen so that the control voltage stayed within the saturation limits (±50 V) in simulations. The model for the LQ was identified at rotation speed 32 Hz with 0.31 T 2-pole flux density.

The state estimator of LQ was given some time to find all the states before the control voltage was switched on. The vibrations were damped almost immediately as seen from Figure 6.32(a). There is a 2 second transient visible during which the control result still improves. Figure 6.32(b) shows that the rotor moves to the smaller orbit in just 2 rotor revolutions.

In the beginning, the controller requested a very high voltage. Saturation limits for the control voltage were set to ±45 V in the control program to prevent the saturation happening in the DA-converters. The state observer was given the saturated signal. In steady state the control voltage was about 40 V.

The LQ could not remove the vibration completely. The controller was trying to control the rotor to the shape orbit but the remaining mechanical vibration in x-direction was around 30 μm. In y-direction, the result was

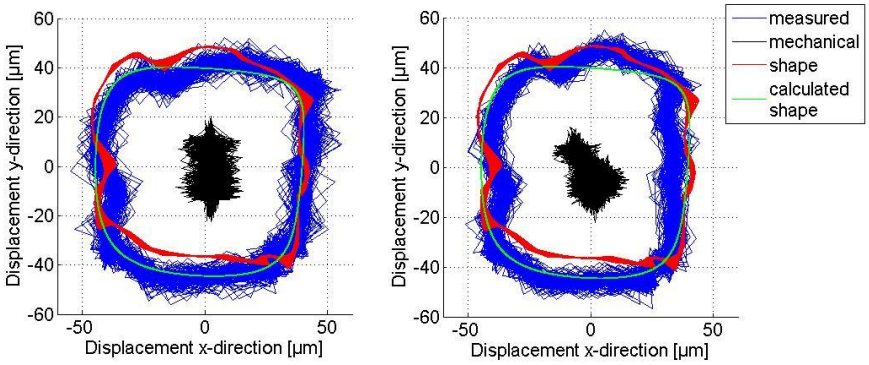

Figure 6.30: Comparing coordinations in steady state. On the left, CC in k-coordination, and on the right, CC in field coordination. The mechanical vibrations are equally small in both (black dots in the middle). For some reason, the calculated shape used by the controllers (thin green line) is visibly lower than the actual shape (red).

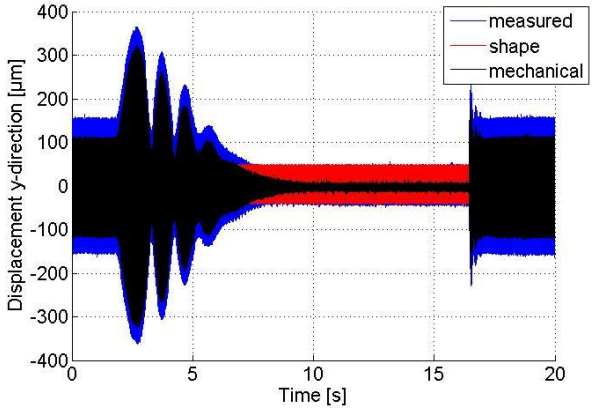

Figure 6.31: The k-coordination CC has a huge overshoot at the beginning. The switch off at the end reveals how much the controller actually reduces the vibration. The data was taken at the moment when the disturbance was at its lowest. The percentual damping is even higher when compared to the maximum of the uncontrolled vibration.

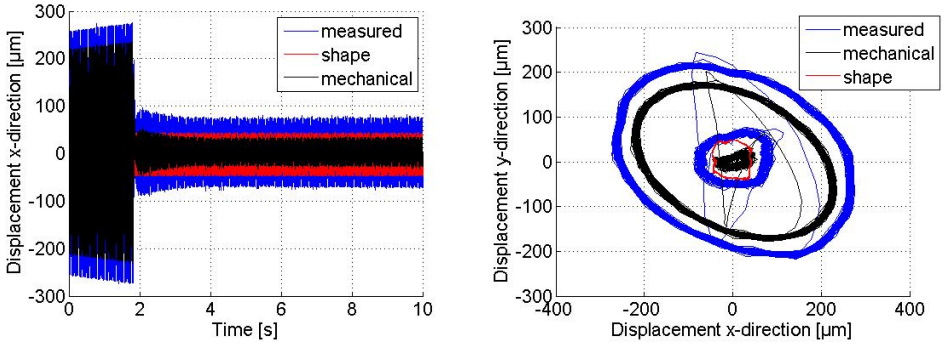

(a) x-direction (b) XY-plot

Figure 6.32: LQ control at 32 Hz 0.31 T. The controller is trying to set the rotor to the shape orbit. The control is switched on before 2 s. The rotor moves to the smaller orbit within 2 rotor revolutions but the remaining vibration is higher than with CC.

closer to the results of the CC.

The LQ-controller proved to be extremely robust. When the rotation speed of the machine was increased, the vibrations increased but stayed under control. The control voltage was too close to the 45 V saturation limit so another LQ with smaller $\mathbf{Q}$ matrix weights was used. For the "weaker" LQ the control voltage at 32 Hz was about 20 V.

The LQ controller allowed the rotation speed to be slowly increased up to 50 Hz, even though the disturbance model in the state observer was specifically designed for 32 Hz. The machine stayed stable even when the flux density was changed. The flux density needed to be increased to prevent the control voltage from saturation. Increasing the 2-pole flux enabled the controller to produce the same force with smaller voltage.

The LQ allowed the rotor to be driven at critical speed with ease. Figure 6.33(a) shows the rotor orbit at 36.4 Hz which is possibly already past the critical speed. From 33 Hz to 37 Hz, there was little change in the vibration levels. Figure 6.33(b) shows the orbits at the rated noload point at 50 Hz stator phase voltage being 230 V. The main winding current was 14.5 A and the slip was again zero. An interesting result was that when the control was switched off at 50 Hz, the machine became unstable.

Although the LQ kept the machine stable almost at all operation points[7],

[7]Every operation point tested that had the 2-pole flux density high enough to produce needed force without the control signal saturating.

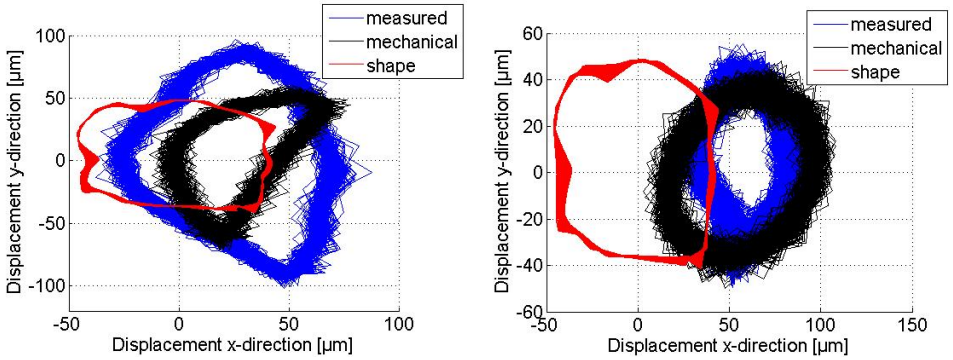

(a) LQ at 36.4 Hz 0.53 T (b) LQ at 50.1 Hz 0.7 T

Figure 6.33: The same controller as in Figure 6.32 worked for other rotation speeds with higher flux densities than designed. The controller kept the machine stable at critical speed (a) and at nominal operation point (b). The machine could not be driven without control at either of the operation points. Thus, there is no orbits without control plotted. The control voltage needed for 50 Hz was 26 V.

the vibrations were not completely removed. This was to be done with the CC designing it for the LQ-controlled closed-loop system. The system transfer function was first calculated from the identified model for the machine and the matrices of the LQ-controller. In theory, this method should work but in practice, it did not. Thus, a model for the closed-loop system was identified with noise inputs using the same methods that were used to get the original model.

The closed loop identification was first done at the same operation point as at which the model for the LQ was identified, 32 Hz 0.31 T. The results were as good as the CC results at 30 Hz. With the LQ, there was not any beginning transient like the one in Figure 6.31. The remaining vibration left by the LQ converged more like in Figure 6.25(a).

With the combined control, the rotation frequency could be increased to 36 Hz. The CC took the rotation angle from the tachometer so it stayed at the frequency of the disturbance. When the same was tested with CC alone, the flux density had to be decreased and the machine stayed stable to 35 Hz at maximum. With the LQ, the flux density could be increased. Yet, at 36 Hz 0.65 T the control broke down. Possibly because the flux density was so much higher than in the operation point of the identification, the model error became too big.

The model for the closed-loop system was re-identified at 35.7 Hz 0.52 T.

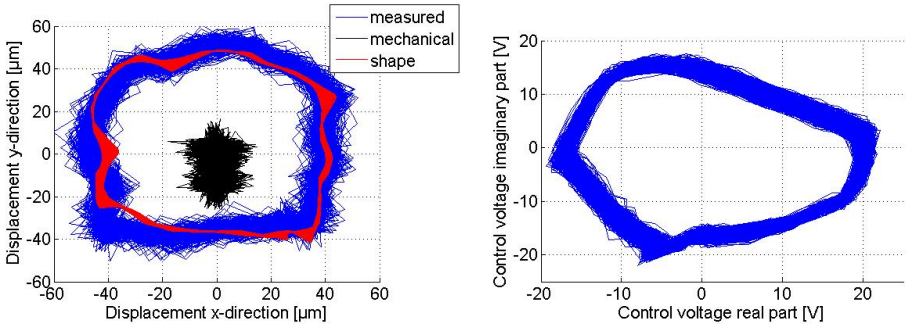

(a) Displacement (b) Control voltage

Figure 6.34: LQ-control with CC at 36Hz 0.72 T. The LQ was designed for operation point 32 Hz 0.31 T and the CC for the closed-loop system at 35.7Hz 0.52 T. The CC is controlling the first harmonic and the DC off-set. Figure (a) shows that the vibrations can be completely controlled. Again, there is no orbits without control because the machine is not stable at the used operation point. Figure (b) shows the control voltage in k-coordination.

When the CC was designed with this new model, the vibration could be completely controlled at 36 Hz 0.7 T which was estimated to be the critical speed at the rated flux density. Figure 6.34(a) shows the rotor orbit at this operation point and Figure 6.34(b) the control voltage of the combined controller.

The CC was made to control two frequencies, the rotation frequency and 0 Hz. When the flux density was increased, the rotor was pulled to the positive direction of the x-axis defined in Figure 5.4. This happened at all frequencies. The 0 Hz component of the CC was able to center the rotor. Figure 6.35 demonstrates the effect of the DC control. Figure 6.35(b) shows only the steady state orbits.

The CC in Figure 6.35 is the one designed for 32 Hz. The 35.7 Hz controller had some stability issues with rotation speeds lower than 33 Hz. It is possible to make a controller that has both of the CC controllers and switches between them. Since their operation areas overlap, combining them would be an easy way to remove the discovered limitation.

To prove that the machine had been driven at the critical speed, the machine was disconnected from the main power supply at 50 Hz. The extra winding circuit was opened so no currents in the 4-pole winding could affect the vibrations. Figure 6.36 shows the rotor displacement in x-directions and the rotation speed given by the tachometer during the rundown measurement.

When the rotor slows down to 38 Hz, the vibrations increase rapidly and

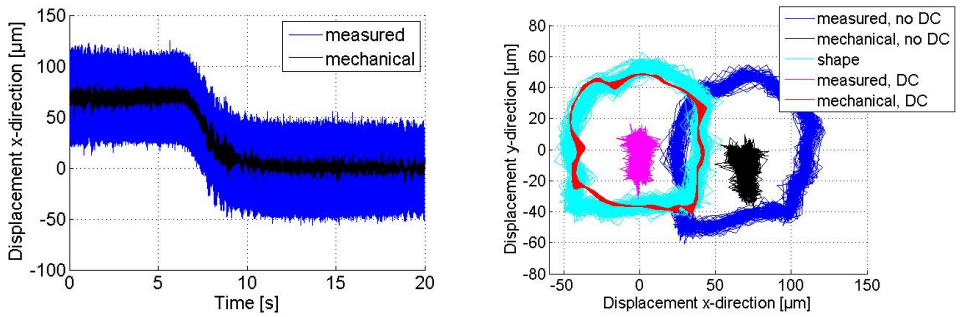

(a) x-direction (b) XY-plot

Figure 6.35: DC component of the CC is switched on at 32.1 Hz 0.56 T. When the 2-pole flux density was increased, the rotor moved to the positive direction of the x-axis. Neither the LQ or CC for the first harmonic component could remove the displacement. Thus, CC for DC displacement was added.

at 37.5 Hz the rotor already hit the safety bearings. The rotation speed drops quickly at the impact and then comes down smoothly. Based on the figure, the critical speed would be about 37.3 Hz. Modal tests confirmed the natural frequency being at 37.3-37.6 Hz. This was without the magnetic field. The magnetic field drops the frequency to some where between 33 Hz and 37 Hz. The vibration could be controlled at all those frequencies.

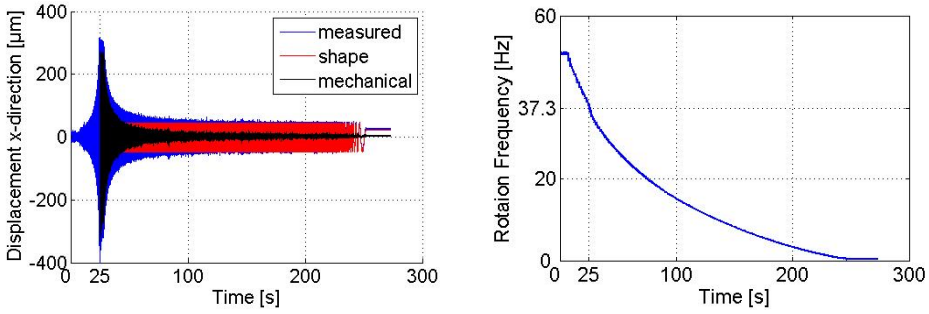

(a) Displacement x-direction (b) Rotation frequency

Figure 6.36: LQ and CC controllers are used to guide the rotor to the origin of measurement coordination at 50 Hz. The machine is cut off from the main supply and the extra winding circuit is opened. Figure (a) shows the rotor displacement in x-direction as friction slows down the machine. At 25 s, the machine has slowed down the critical speed and hits the safety bearings. Figure (b) shows that the rotation frequency is about 37.3 Hz at that time.

Chapter 7

Conclusions

Controlling flexural vibration of a cage induction machine was studied with a small scale test machine. Models for the machine were derived from physical equations with some simplifying assumptions. Different identification methods as well as two different types of controllers were presented.

The flexible and bowed rotor shaft caused big problems for modeling the machine. The machine could not be driven at the rated the flux without some vibration control on and the rotation speed could only be increased to 34 Hz without control. The bowed rotor also made the identification of models more difficult. It caused the amplitude of the rotor displacement without control to be so high that the amplitudes of the identification signals needed to be limited.

The modeling partially failed. The much wanted physical parametric model was not obtained. Some identification methods seemed very promising but there was not enough time to work on them. The identification attempts suggested that there might be something missing from the derived equation, something that should be included to the model.

Despite the modeling difficulties, the vibration control was a success. The measurements proved that the extra winding can produce sufficient force to control the rotor and that the force can be controlled. The LQ controller kept the machine stable at all operation points and the CC controller was able to remove the vibrations almost completely as long as the 2-pole flux density was high enough. The machine could easily be driven at the critical speed fulfilling the objectives of the research.

This thesis still leaves several open questions for future research. Acquiring the parametric model is one future objective, even though there is a change it is not needed. It might be possible to design an adaptive controller for the machine that does not require complete models. Some theoretical study of the controllers used might still be needed to prove that the methods

used can be generalized. At least for this purpose, the parametric model might be useful.

There is also some theoretical study needed before the methods can be tested in full scale with over 2 MW machines. Although the frequency converters were abandoned with the small scale machine, the tests showed no real reason, why they could not be used for bigger machines. Still this claim should be proven. It should also be shown that the passive damping effect, when short circuiting the extra winding, appears also with bigger machines and at all operation points.

Before even thinking about commercializing the vibration-control method, the same research should be done for a loaded machine. The test machine was never loaded and run most of the time completely without slip. Some problems the slip causes, were experienced and solved. Loading the machine could bring plenty of new problems to be solved.

Bibliography

Arkkio, A. & Holopainen, T. (2008), Origin of unbalanced-magnetic-pull components in electrical machines, *in* 'Proceedings of 9th International Conference on Vibrations in Rotating Machinery', The University of Exeter.

Belmans, R., Vandenput, A. & Geysen, W. (1984), Influence of the electromagnetical phenomena on the radial vibrations of a two-pole induction motor with squirrel cage rotor, *in* 'Proceedings of International Conference on Electrical machines (ICEM-84)', Lausanne, Switzerland, pp. 695–699.

Boldea, I. & Nasar, S. A. (2002), *The induction machine handbook*, CRC Press, Boca Raton, Florida.

Brauer, J. R. (2006), *Magnetic actuators and sensors*, John Wiley & Sons.

Burrows, C. R. & Sahinkaya, M. N. (1983), 'Vibration control of multi-mode rotor-bearing systems', *Proc. of the Royal Society of London, Series A, Mathematical and Physical Sciences* **Vol. 386 No. 1790**, 77–94.

Chiasson, J. (2005), *Modeling and high-performance control of electric machines*, Wiley-Interscience, New Jersey.

Chiba, A., Fukao, T. & Rahman, M. (2006), 'Vibration suppression of a flexible shaft with a simplified bearingless induction motor drive', *Conference Record of the 2006 IEEE Industry Applications Conference 2006. 41st IAS Annual Meeting.* **vol.2**, 836–842.

Fetter, A. L. & Walecka, J. D. (2003), *Theoretical mechanics of particles and continua*, Courier Dover Publications.

Franklin, G. F., Powell, J. D. & Workman, M. L. (1998), *Digital control of dynamic systems*, 3rd edn, Addison-Wesley, Menlo Park, CA.

Genta, G. (1999), *Vibration of structures and machines: practical aspects*, Springer-Verlag New York, Inc.

Harvey, A. C. (1991), *Forecasting, structural time series models and the Kalman filter*, Cambridge University Press.

Hiromi, T., Katou, T., Chiba, A., Rahman, M. & Fukao, T. (2007), 'A novel magnetic suspension-force compensation in bearingless induction-motor drive with squirrel-cage rotor', **43(1)**, 66–76.

Holmgren, W., Hasling, J. & Denny, R. (1979), 'Non-contact distance measurement system', US Patent 4160204.

Holopainen, T. (2004), *Electromechanical interaction in rotordynamics of cage induction motors*, number 634, VTT Publifications, Espoo. Doctoral Thesis.

Hubert, C. (2002), *Electric machines: theory, operation, application, adjustment, and control*, second edn, Prentice Hall, New Jersey.

Jeffcott, H. H. (1919), 'The lateral vibration of loaded shafts in the neighbourhood of a whirling speed: the effect of want of balance', *London, Edinburgh and Dublin philosophical magazine and journal of science* **6:27**, 304–314.

Katayama, T. (2005), *Subspace methods for sytem identification*, Springer.

Keogh, P., Cole, M. & Burrows, C. (2002), 'Multi-State Transient Rotor Vibration Control Using Sampled Harmonics', *Journal of Vibration and Acoustics* **124**, 186.

Kovács, P. K. (1984), *Transient phenomena in electrical machines*, Elsevier Science Publishers, Amsterdam.

Laiho, A., Tammi, K., Zenger, K. & Arkkio, A. (2008), 'A model-based flexural rotor vibration control in cage induction electrical machines by a built-in force actuator', *Electrical Engineering (Archiv für Electrotechnik)* **90(6)**, 407–421.

Lantto, E. (1999), 'Robust control of magnetic bearings in subcritical machines', *Doctoral dissertation. Acta Polytechnica Scandinavica, The Finnish academy of technology* pp. 1–143, http://lib.tkk.fi/Diss/199X/isbn9512255758/.

Lewis, F. L. & Syrmos, V. L. (1995), *Optimal control*, 2nd edn, John Wiley & Sons, Inc.

Ljung, L. (2006), *System identification: theory for the user*, second edn, Prentice Hall.

Orivuori, J. (2008), Active control of rotor vibrations in electric drivers, Master's thesis, Department of Automation and Systems Technology, Helsinki University of Technology.

Orivuori, J., Laiho, A. & Sinervo, A. (2008), Active control of radial rotor vibrations in electric machines: identification, modeling and control design, *in* 'NORPIE 2008 - Nordic Workshop on Power and Industrial Electronics', University of Technology, Faculty of Electronics, Communications and Automation, Espoo, Finland. Digital publification (http://lib.tkk.fi/Conf/2008/urn011661.pdf).

Price, K. V., Storn, R. M. & Lampinen, J. A. (2005), *Differential Evolution: A Practical Approach to Global Optimization*, Springer Verlag.

Rao, J. S. (2000), *Vibratory condition monitoring of machines*, Narosa Publishing House, New Delhi, India.

Rashid, M. (2004), *Power electronics: circuits, devices and applications*, third edn, Pearson Education, Inc., New Jersey.

Sedra, A. & Smith, K. (2004), *Microelectronic Circuits*, fifth edn, Oxford University Press, Inc.

Taegen, F. (1964), 'Die bedeutung der läufernutschlitze für die theorie der asynchronmachine mit käfigläufer.', *Arch. für Electrotechnik* (48), 373–386.

Tammi, K. (2007), *Active control of radial rotor vibrations: identification, feedback, feedforward, and repetitive control methods*, number 634, VTT Publications, Espoo. Doctoral Thesis.

Ursem, R. & Vadstrup, P. (2003), 'Parameter identification of induction motors using differential evolution', *The 2003 Congress on Evolutionary Computation, CEC '03.* **Vol.2, 8-12 Dec. 2003**, 790–796.

van Dam, R. & Immink, K. (1980), 'Tachometer system', US Patent 4216419.

Wildi, T. (2006), *Electrical machines, drives, and power systems*, 6th edn, Pearson Education, Inc.

Zenger, K., Sinervo, A., Orivuori, J., Laiho, A. & Tammi, K. (2008), Parallel disturbance force compensator for electrical machines, *in* 'The 17th IFAC World Congress', Seoul, Korea. Digital publification (DVD).